INFORMATION TO USERS

This manuscript has been reproduced from the microfilm master. UMI films the text directly from the original or copy submitted. Thus, some thesis and dissertation copies are in typewriter face, while others may be from any type of computer printer.

The quality of this reproduction is dependent upon the quality of the copy submitted. Broken or indistinct print, colored or poor quality illustrations and photographs, print bleedthrough, substandard margins, and improper alignment can adversely affect reproduction.

In the unlikely event that the author did not send UMI a complete manuscript and there are missing pages, these will be noted. Also, if unauthorized copyright material had to be removed, a note will indicate the deletion.

Oversize materials (e.g., maps, drawings, charts) are reproduced by sectioning the original, beginning at the upper left-hand corner and continuing from left to right in equal sections with small overlaps.

Photographs included in the original manuscript have been reproduced xerographically in this copy. Higher quality 6" x 9" black and white photographic prints are available for any photographs or illustrations appearing in this copy for an additional charge. Contact UMI directly to order.

Bell & Howell Information and Learning
300 North Zeeb Road, Ann Arbor, MI 48106-1346 USA

UMI®
800-521-0600

DISSERTATION

INVESTIGATIONS OF SURFACE INTERACTIONS AND DEPOSITION MECHANISMS IN PLASMA ENHANCED CHEMICAL VAPOR DEPOSITION OF SILICON-BASED MATERIALS

Submitted by

Patrick R. McCurdy

Department of Chemistry

In partial fulfillment of the requirements

for the Degree of Doctor of Philosophy

Colorado State University

Fort Collins, Colorado

Fall 1999

COLORADO STATE UNIVERSITY

February 17, 1999

WE HEREBY RECOMMEND THAT THE DISSERTATION PREPARED UNDER OUR SUPERVISION BY **PATRICK R. MCCURDY** ENTITLED **INVESTIGATIONS OF SURFACE INTERACTIONS AND DEPOSITION MECHANISMS IN PLASMA ENHANCED CHEMICAL VAPOR DEPOSITION OF SILICON-BASED MATERIALS** BE ACCEPTED AS FULFILLING IN PART THE REQUIREMENT FOR THE DEGREE OF DOCTOR OF PHILOSOPHY.

Committee on Graduate Work

Advisor

Department Head

ABSTRACT OF DISSERTATION

INVESTIGATIONS OF SURFACE INTERACTIONS AND DEPOSITION MECHANISMS IN PLASMA ENHANCED CHEMICAL VAPOR DEPOSITION OF SILICON-BASED MATERIALS

Plasma processing of silicon-based materials is widely used in the semiconductor industry for the production integrated circuits. Two very important materials are silicon carbide and silicon nitride. Silicon carbide has found applications in solar cells, flat panel displays, photoreceptors, and photoresist materials, while silicon nitride thin films are used as gate dielectrics and barrier coatings in microelectronic devices, as capacitors in dynamic random access memory cells and in the microfabrication of sensors and actuators. Here the various aspects of the chemistry of plasmas used for producing thin films of hydrogenated amorphous silicon carbide (a-$Si_{1-x}C_x$:H) and hydrogenated amorphous silicon nitride (a-SiN_x:H) have been investigated.

First, the surface reactivities of two species, NH_2 and SiH have been investigated using the imaging of radicals interacting with surfaces (IRIS) technique. IRIS combines spatially-resolved laser-induced fluorescence with molecular beam and plasma techniques. The interaction of NH_2 radicals on a variety of substrates has been measured using both NH_3 and SiH_4/NH_3 plasmas. The latter system deposits a-SiN_x:H films. Surface production NH_2 was found under most plasma conditions. In addition to surface reactivities, the internal and translational energies of NH_2 radicals in an NH_3 plasma

molecular beam have been characterized.

The surface reactivity of the SiH radical in SiH_4-based plasmas under wide ranging conditions has been measured. Under all deposition conditions, the reactivity of SiH remains high, 0.95 ± 0.05. In addition, velocity distributions for SiH provide translational temperatures under a variety of plasma processing conditions.

Second, equivalently powered, pulsed and continuous wave SiH_4/CH_4 radio-frequency discharges (13.56 MHz) were used to deposit a-$Si_{1-x}C_x$:H. Deposited films were analyzed with FTIR, XPS, SEM, profilometery, and OES. Deposition parameters investigated included pulsed plasma power, duty cycle, substrate bias, and addition of H_2 as a diluent gas. Oxidation rates for a-$Si_{1-x}C_x$:H films deposited from both pulsed and CW films have been measured using FTIR.

Patrick R. McCurdy
Department of Chemistry
Colorado State University
Fort Collins, Colorado 80523-1872
Fall 1999

ACKNOWLEDGMENTS

First of all, I would like to acknowledge my advisor, Ellen Fisher, for her outstanding contribution as my mentor in graduate studies. She has learned to master the art of advising in a very short time-span. She was quick to help whenever asked, but never micro-managed my work.

Most of all, I would like to thank my wife, Julie, and children–Courtney, Colin and Ellen for the sacrifices they had to make for me to get through six years of graduate school.

DEDICATION

This work is dedicated to my wife, Julie, for standing by me through the hard times during the past six years of graduate school. I could not have done it without her.

TABLE OF CONTENTS

CHAPTER 1

INTRODUCTION AND OVERVIEW

Plasmas used for processing materials are partially ionized gases composed of ions, free electrons, atoms, molecules, and free radicals. These plasmas are used in a wide variety of thin film processes, such as plasma enhanced chemical vapor deposition (PECVD), plasma etching, and surface modification of polymers. Unlike other thin film techniques, such as molecular beam epitaxy and chemical vapor deposition, plasma processes are not thermal, and the dynamics of these processes are not well described by equilibrium thermodynamics. Because of the complexities of plasma systems, many reaction mechanisms remain unknown, including those for material deposition.

Radicals have long been assumed to be the most important species in plasma depositions because of their relative reactivities and abundance in these systems. While traditional empirical methods of PECVD thin film analysis provide much needed information, the development of new plasma processes is severely limited by the lack of understanding of the chemistry occurring in these systems. Thus, a solid understanding of the chemistry occurring at the plasma-surface interface during plasma processing is vital for optimization of existing processes and to drive the development of new materials.

1.1. NON-EQUILIBRIUM SYSTEMS

Unlike thermal plasmas, such as the sun, processing plasmas are not in thermodynamic equilibrium.[1] In the bulk of the plasma, the electron temperature, T_e, is much higher than either the ion temperature, T_i, or the neutral gas temperature, T_g.[2] Although both electrons and ions gain energy from an external applied field, the elastic collisions with neutral molecules are numerous for both species. Because the electron mass is much smaller than that of neutral molecules, little kinetic energy is transferred during collisions. In contrast, similar masses between ions and neutrals allow significant kinetic energy transfer from the ion to the neutral species.[3] In elastic collisions, both the kinetic energy and the momentum of the colliding species are conserved, equation 1.1.

$$E_{trans} = \frac{4 m_e m_n}{(m_e + m_n)^2} E_o \qquad (1.1)$$

In this expression, m_e is the mass of the electron or ion, m_n is the mass of the neutral, E_{trans} is the energy transferred, and E_o is the initial kinetic energy of the ion or electron. Equation 1.1 shows the relationship between mass difference and energy transfer for elastic collisions. The initial kinetic energy of the neutral is assumed to be zero. This results in ions rapidly losing energy in collisions with neutrals; thus they equilibrate to the same temperature, $T_i \approx T_g$. Simultaneously, electrons gain energy from the external applied field, and, although they undergo many elastic collisions, little energy is lost because of the large mass difference. Thus, T_e is much greater than either T_i or T_g.

1.2. PLASMA SHEATHS

Because of the greater mobility of electrons over ions, electrons are lost preferentially to the surfaces of the plasma reactor.[1] This preferential loss of electrons results in a positively charged sheath surrounding all surfaces in the reactor. Plasma sheaths are characterized by very low electron densities and appear as dark areas adjacent to surfaces in contact with the plasma. Unlike the bulk of the plasma, across the sheath of plasmas $T_i >> T_e >> T_g$. Ions accelerated across this sheath are known as bombarding ions because of their high energy. They play an important role in many plasma processes such as reactive ion etching.[1]

1.3. PLASMA MODES.

Another factor that makes plasma systems difficult to characterize is that they can exist in many different modes. All modes can be classified as either low density or high density.[1] Low density plasmas, defined by their lower electron densities, have high-voltage sheaths over a significant surface area. The most common type of low density plasma is a parallel plate capacitively coupled discharge. Radio frequency (rf) coil reactors, as described in Chapters 2 and 6, can also be capacitively coupled and, therefore, can produce low density plasmas. In contrast, high density plasmas typically have an order of magnitude higher degree of ionization ($\sim 10^{11}$ cm^{-3} vs. $\sim 10^{10}$ cm^{-3})[1] and are characterized by low voltage sheaths over the surfaces of the reactor. Inductively coupled rf discharges, microwave discharges, and electron cyclotron discharges are examples of high density plasmas.

1.4. COIL DISCHARGES

As mentioned in the previous section, coil reactors can operate in either a capacitively coupled mode or an inductively coupled mode. The inductively coupled mode is favored by high applied rf powers and low pressures, and is characterized by higher plasma densities, an increased brightness of the discharge, and lower sheath potentials.[4] In inductively coupled plasmas, the charged particles are accelerated azimuthally, while in the capacitively coupled regime the charged particles are accelerated axially.[5] This difference in the direction of the electric field also causes the glow in the inductively coupled regime to be confined to the coil region, while the glow in the capacitively coupled regime extends throughout the discharge tube.[6]

These two modes in rf coil discharges are not mutually exclusive. In rf coil discharges, plasmas are normally ignited in the capacitive regime before reaching the inductively coupled mode, but once the inductively coupled mode is ignited, both modes usually operate simultaneously.[6] The simultaneous operation of both capacitive coupling and inductive coupling is characterized by the appearance of a bright, localized plasma confined to the coil region embedded in a diffuse, faint plasma.[7]

It has also been shown that very different surface chemistry can occur at the plasma-surface interface in these two modes. For etching experiments, Choe et al. studied Si etching by Cl_2 plasmas, and found very different etching rates occurred in the same reactor when changing between the two modes.[8] In the experiments described in Chapters 7 and 8, changes in the plasma mode affect the types of amorphous, hydrogenated silicon carbide (a-$Si_{1-x}C_x$:H) films deposited. The role of plasma modes in these depositions is

discussed extensively in Chapter 8. The role of plasma modes in PECVD is not, however, well characterized or understood.

1.5. PULSED PLASMAS

Recently, there has been a growing interest in the use of pulsed plasmas to deposit thin films. Pulsed plasmas have been shown to give a high degree of control over the retention of functional groups in the deposition of organic films.[9] While the majority of this research has focused on the plasma polymerization of organic monomers, some work has also been performed on the pulsed plasma deposition of inorganic thin films, such as TiN.[10] Pulsing the plasma in a rf coil reactor has the added benefit of allowing the inductively coupled regime to be reached at much lower overall power inputs. Thus, for low duty cycle, high peak power pulsed plasmas, high plasma densities can be realized, with low power consumption and little heating of the substrate.

1.6. OVERVIEW OF RESEARCH

To date, the vast majority of work that has been performed on the PECVD of thin films has been from an overwhelmingly empirical approach. Factors such as flow rate, plasma composition, substrate temperature, pressure, power, and reactor geometry are correlated to deposition rates, and physical properties of the deposited films. This empirical approach has been used largely because the multitude of species which exist in plasmas (radicals, ions and neutrals), undergo many complex chemical processes simultaneously, both in the gas phase and at the gas-surface interface. Thus, full

characterization of the plasma chemistry is difficult.

In general, knowledge about both individual plasma species as well as film composition and properties is necessary to fully understand a plasma deposition system. The first half of this dissertation focuses on measuring the surface interactions of individual species in plasmas (i.e. SiH and NH_2). The remainder of this dissertation focuses on characterizing plasma deposited a-$Si_{1-x}C_x$:H films as a function of plasma deposition parameters.

1.6.1. MOLECULAR APPROACH

In Chapter 2, an overview of the imaging of radicals interacting with surfaces (IRIS) apparatus is given. This instrument employs molecular beam techniques and laser induced fluorescence (LIF) for measuring the reactivity of gas phase radicals at the surface of a depositing film. IRIS uses an inductively coupled plasma source to create a molecular beam which contains essentially all plasma species. A tunable excimer-pumped dye laser is used to excite a single molecule in the complex plasma molecular beam. LIF signals are imaged onto a gated, intensified charge coupled device (ICCD) to provide spatial resolution. ICCD images depict the fluorescence from molecules both in the molecular beam and scattered from the surface of a depositing film. Data collected with and without a substrate in the path of the molecular beam provide information about the surface reactivity of the species of interest.

In Chapter 3, the velocity distributions of NH_2 molecules in an effusive NH_3 plasma molecular beam were measured as a function of applied rf plasma power using

spatially and temporally resolved LIF signals. Monte Carlo simulation methods were employed to model spatial profiles of radicals in the molecular beam. The model assumes an initial Gaussian distribution of molecules across the laser's path and calculates time dependent changes in the profiles using Maxwell-Boltzmann distributions. Preliminary data on velocity profiles for NH_2 radicals scattered from a 300 K Si substrate are also presented.

In Chapter 4, the surface reactivity of SiH in a 100% SiH_4 plasma molecular beam was measured on a 300 K Si (100) substrate. The molecular beam deposited a-Si:H films similar to those produced in our inductively coupled reactors. The substrate temperature dependence (300-673 K) of the reactivity is also presented. In addition, results of velocity distribution measurements for SiH in the plasma molecular beam are presented.

Results from IRIS experiments on the surface scattering of NH_2 radicals from a variety of substrates during NH_3 plasma processing are presented in Chapter 5. In most cases, the NH_2 surface scattering was found to be greater than unity. This suggests NH_2 is produced through surface reactions. The density distribution of scattered NH_2 radicals had a cosine angular dependence from all substrates. The velocity distributions of NH_2 radicals scattering from a variety of 300 K substrates were determined. The relative abundance of NH_2 in SiH_4/NH_3 plasmas as a function of the ratio of the feed gases in a 45 W plasma was also determined. At an SiH_4/NH_3 ratio of 0.30 or greater, no NH_2 signal was detected in our plasma molecular beam.

1.6.2 FILM FORMATION AND CHARACTERIZATION

In Chapter 7, the oxidation rates for a-$Si_{1-x}C_x$:H films deposited from both pulsed and continuous wave (CW) SiH_4/CH_4 rf (13.56 MHz) plasmas were measured using Fourier transform infrared (FTIR) spectroscopy. Films deposited from CW plasmas oxidize much more rapidly than those deposited from equivalently powered pulsed plasmas. The effect of a diluent gas in the feed (He, Ar, or H_2) on film oxidation rates was also investigated. Additional compositional changes in the a-$Si_{1-x}C_x$:H materials with addition of H_2 to the plasma feed gas are also discussed.

Chapter 8 investigates equivalently powered, pulsed and CW SiH_4/CH_4 plasmas used to deposit a-$Si_{1-x}C_x$:H films, which were analyzed with FTIR, XPS, SEM, and profilometery. Plasmas were characterized using optical emission spectroscopy (OES). Deposition parameters investigated included pulsed plasma power, duty cycle, cycle time, and addition of H_2 as a diluent gas. The effect of charged particles on film characteristics was also investigated by biasing the substrates, and by deflecting ions.

REFERENCES

1. M. A. Lieberman and J. J. Lichtenberg, *Principles of Plasma Discharges and Materials Processing* (Wiley, New York, 1994).

2. S. M. Rossnagel, *Thin Film Processes II*, edited by J. L. Vossen and W. Kern (Academic, San Diego, CA, 1991), p. 11.

3. G. J. Collins, *Plasma Process Technology Fundamentals* (Colorado State University, Fort Collins, CO, 1985)

4. H. U. Eckert, Proc. 2nd Int. Conf. on Plasma Chem. and Technol., edited by H. Boening, (Technomic, Lancaster, PA, 1986), p 171.

5. U. Kortshagen, N. D. Gibson, and J. E. Lawler, J. Phys. D **29**, 1224, (1996).

6. J. Amorim, H. S. Maciel, and J. P. Sudano, J. Vac. Sci. Technol. B **9**, 362 (1991).

7. C. A. Nichols, J. R. Woodworth, and T. W. Hamilton, J Vac. Sci. Technol. A **16**, 3389 (1998).

8. J. Y. Choe, I. P. Herman, and V. M. Donnelly, J. Vac. Sci. Technol. A **15**, 3024 (1997).

9. M. A. Leich, N. M. Mackie, K. L. Williams, and E. R. Fisher, Macromolecules **31**, 7618 (1998). N. M. Mackie, D. G. Castner, and E. R. Fisher, Langmuir **14**, 1227, (1998). N. M. Mackie, and E. R. Fisher, Polym. Prepr. **38**, 1059 (1997).

10. V. Panchalingam, X. Chen, C. R. Savage, R. B. Timmons, and R. C. Eberhart, J. Appl. Polym. Sym. **54**, 123 (1994).

CHAPTER 2

A MOLECULAR BEAM INSTRUMENT FOR THE IMAGING OF RADICALS INTERACTING WITH SURFACES EXPERIMENTS

2.1. INTRODUCTION

Understanding the interactions of molecules with surfaces is fundamental to the development of many technologically relevant processes such as chemical vapor deposition (CVD),[1] plasma-enhanced CVD (PECVD),[2] plasma etching,[3,4] and surface modification of polymers.[5,6] In all of these processes, chemical and structural changes occur as a result of gas-phase molecules interacting with a solid surface. The chemistry associated with these systems is often complicated by the presence of a variety of gas-phase species, including radicals, electrons, and ions which can react with each other as well as with the surface being processed. Unfortunately, little is known about gas-surface reactions[7,8] within these environments, especially those involving radical species.[9] Yet, radicals are believed to be the most important species in both etching and deposition systems.[10] Indeed, the majority of proposed mechanisms for CVD and PECVD systems cite radicals as the primary film precursors.[3,10,11] Thus, in order to fully understand the chemical mechanisms involved in CVD and PECVD processes, direct measurements of radical-surface interactions are needed.

The imaging of radicals interacting with surfaces (IRIS) apparatus described here is designed to measure the surface reactivity of gas-phase species during deposition or etching processes.[12,13,14,15] This versatile instrument incorporates a differentially-pumped vacuum system, spatially-resolved laser-induced fluorescence (LIF), molecular beams, and rf plasma technology. The IRIS method was first developed nearly a decade ago at Sandia National Laboratories (SNL).[12] The prototype instrument was used to measure the surface reactivity of SiH on a 300 K substrate using a 100% SiH_4 plasma as the molecular beam source. A subsequent instrument at SNL, incorporating differential pumping, has been used to study SiO,[14] NH,[13] and OH radicals.[15] Our third generation IRIS apparatus is greatly improved over the original design by employing a modular design for the vacuum chamber, a heatable substrate, and a state-of-the-art two dimensional detector.

2.2. INSTRUMENT DESIGN AND PRINCIPLE OF OPERATION

2.2.1. OVERVIEW

The IRIS apparatus discussed here is based on an experimental design developed at SNL.[12] The original IRIS apparatus had a simple, single chamber design. It operated with a single diffusion pump backed by a mechanical pump for evacuation, and a linear diode array detector for collection of LIF signals. A subsequent design at SNL utilized differential pumping to maintain lower operating pressures in the main chamber. The Colorado State University (CSU) apparatus described here also employs differential pumping, but has the added feature of a gated, intensified charge-coupled device (ICCD) camera as the detector.[17] This provides two dimensional images from LIF produced in the

region where the laser intersects the molecular beam, hereafter referred to as the interaction region. Additional features have been added to the IRIS experimental design in use at CSU and are described fully below.

A schematic diagram of the IRIS apparatus is shown in Fig. 2.1. In a typical IRIS experiment, feed gases enter the rear of the plasma tube and rf power is inductively coupled to the gases, and a plasma is produced. Diffusion of the plasma into the differentially pumped region generates a near-effusive molecular beam. The molecular beam contains virtually all neutral and ionized species present in the plasma,[13] including the species of interest. After reaching the main chamber, the beam is collimated by a series of slits. A tunable laser beam enters the main chamber and intersects the molecular beam at 45°, exciting the species of interest. Spatially resolved LIF signals are collected by a gated ICCD array. These data correspond to the species of interest in the incident molecular beam. A substrate is then rotated into the path of the molecular beam and spatially resolved LIF is again collected. The substrate is placed at a specified distance, parallel to the laser beam, Fig. 2.1. Data collected with the substrate in the path of the molecular beam now reflects LIF from incident *and* scattered molecules. The difference between spatial distributions with the surface in and out of the molecular beam is a measure of the radical's surface reactivity. Spatial distributions also indicate scattering mechanisms for radicals investigated (i.e. specular vs. adsorption-desorption). State-specific reactivity measurements are made by tuning the laser to absorption frequencies for different rotational states of the radical of interest. Substrates can be heated to determine the substrate temperature dependence of the reactivity and translated away from the laser

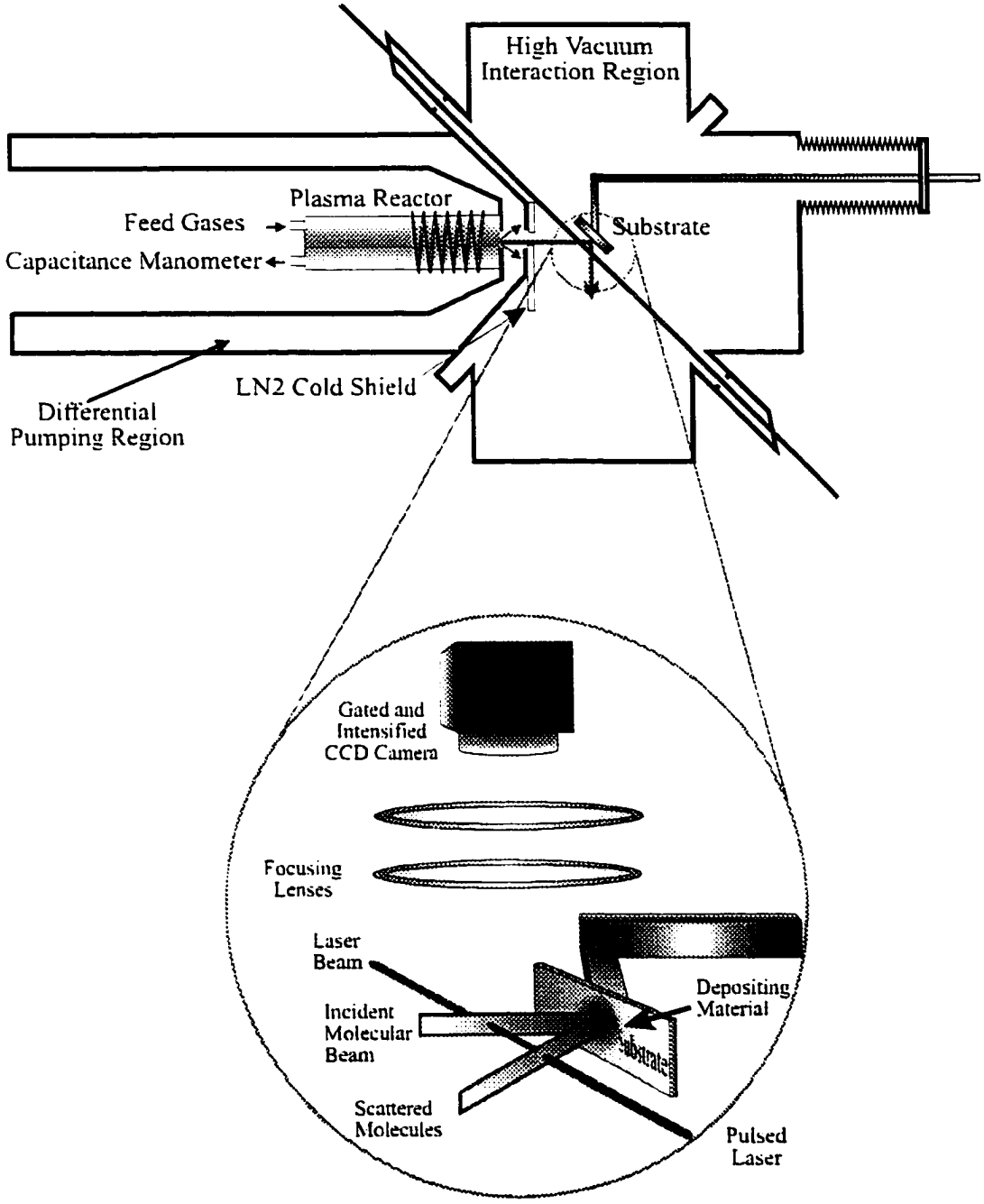

Figure 2.1. Schematic of the CSU IRIS apparatus. The detail of the interaction region shows the spatial orientation of the optics and detector relative to the molecular beam and laser beam. The ICCD camera is located perpendicular to the plane of intersection of the laser beam and molecular beam. Specular scattering of the molecules off the substrate is illustrated.

to characterize the scattered molecules' spatial distribution. Thus, the unique design of the IRIS instrument allows for measurement of the surface reactivity of gas-phase species *during* a plasma deposition or etching process. The following sections describe the various components of the IRIS apparatus in detail.

2.2.2. VACUUM SYSTEM AND MOLECULAR BEAM FORMATION

The vacuum system comprises three primary regions: (1) the plasma region which is indirectly pumped through the other two regions; (2) the differential pumping region; and (3) the main chamber which includes the interaction region.

1. Plasma Source. The source for the molecular beam is an inductively-coupled rf plasma. Figure 2.2 details the plasma region and the molecular beam formation area of the IRIS apparatus. The plasma chamber is built from two 50 mm ID Pyrex glass cylinders with an O-ring joint in the center of the chamber. Fig. 2.2. The total length of the plasma chamber is 32 cm. Removable glass liners (4.4 cm ID) are used in both ends of the plasma reactor to minimize deposition on the inside of the chamber. These liners are replaced periodically when deposits have accumulated on the inside walls.

The pressure in the plasma chamber is monitored using an MKS Baratron capacitance manometer. Base pressure in this region is approximately 1 x 10^{-6} Torr. Under typical operating conditions with a 20 sccm flow of argon, pressure in this region is ~0.040 Torr. The source can also be used without a plasma ignited. This would allow the study of surface reactivity during thermal CVD processes. In addition, the plasma housing can be removed and another molecular beam source can be mated to the

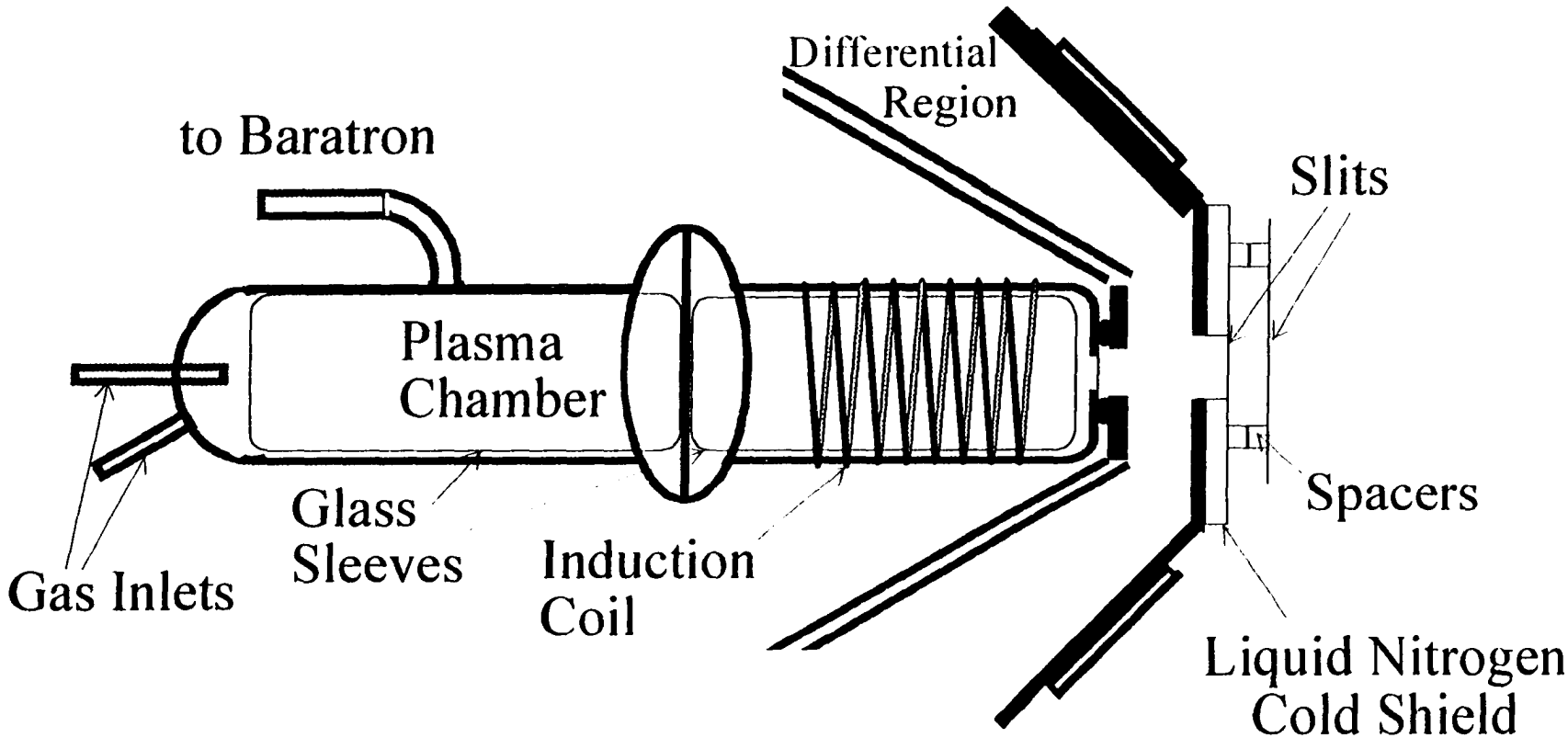

Figure 2.2. Enlarged view of the plasma chamber, differential region, and molecular beam formation area. The position of the collimating slit can be varied by ± 1 cm by changing the length of the slit extentions. precursors and gas flow is controlled by MKS mass-flow controllers (10-1000 sccm).

differential region.

At the back of the plasma chamber there are two 0.635 cm gas inlet ports which are connected to a four line gas manifold. Three of these lines are used for gaseous precursors and gas flow is controlled by MKS mass flow controllers (10-1000 sccm). One of these three lines is dedicated to SiH_4 and Si_2H_6. For safety, this line is equipped with an emergency by-pass around the flow controller. The by-pass has a bellows sealed valve to open and close the by-pass. The fourth line on the manifold is dedicated to high vapor pressure liquids. For liquid precursors, the vapor pressure is controlled by a Nupro bellows-sealed metering valve on the gas manifold. The liquid inlet line can be heated from the source bulb to the plasma chamber (typically 45-60 °C).

The front half of the plasma chamber is wrapped with an eight loop induction coil made from 10 gauge nickel plated copper wire, Fig. 2.2. Radio frequency power (0–300 W, 13.56 MHz) from an ENI HF-300 power supply is inductively coupled to the feed gases through this coil. Coupling is optimized by an rf matching network consisting of an ISI Jennings 100 pF variable capacitor. Typical applied powers are 20-200 W, giving power densities of ~ 0.088 to 0.88 W/cm^3. A grounded metal screen placed in the chamber confines the plasma to the front 15 cm of the tube. The two halves of the plasma chamber are held together by an aluminum collar that is mounted to the differential pumping region with four long bolts. An O-ring makes a vacuum seal between the plasma chamber and the differential housing. The front end of the glass cylinder contains a 1.0 cm diameter orifice through which gas molecules diffuse into the differential region.

2. Differential Region. A molecular beam is formed as species diffuse from the 1.0 cm hole in the plasma chamber through a 1.27 cm hole in the differential housing and into the differential pumping region, Fig 2.2. This region has a volume of ~19 L and consists of the space between the plasma housing and the main chamber. The differential region is pumped by a 4,200 Ls^{-1} Varian HS-10 diffusion pump, backed by a Leybold D30A mechanical pump (12.6 Ls^{-1}) and equipped with a manually operated gate valve located between the pump and the chamber. The differential region reaches a base pressure of 1 x 10^{-7} Torr when pumped overnight, as measured with a Granville-Phillips hot ionization gauge. The typical operating pressure in this chamber, measured during an IRIS experiment (e.g. 20 sccm Ar or 10 sccm SiH_4 flow) is ~2.5 x 10^{-4} Torr.

The differential region and the main chamber are separated by a wall 25 mm from the end of the plasma chamber, Fig. 2.2. The differential wall is ~3.1 mm thick and contains a 2.5 cm diameter hole, directly in line with the hole in the end of the plasma chamber. The size of this orifice can easily be decreased by mounting a defining slit on the main chamber side of the wall. The plasma molecular beam species diffuse through this hole and into the main chamber.

3. Main Chamber. The main chamber is the largest chamber of the IRIS apparatus, with a volume of ~32 L. It is pumped by a 4,200 Ls^{-1} Varian HS-10 diffusion pump backed by a Welch 1397 mechanical pump (8.3 Ls^{-1}) and equipped with a water baffle and pneumatic gate valve stacked between the pump and the chamber. This chamber reaches a base pressure of 1 x 10^{-7} Torr after pumping overnight, as measured by a Granville-Phillips hot ionization gauge. The typical operating pressure in the main

chamber (with two defining slits, ~1.0 mm each) during an IRIS experiment (e.g. 20 sccm Ar or 10 sccm SiH_4) is ~4 x 10^{-6} Torr.

Under normal experimental conditions, the vast majority of the plasma molecular beam species are pumped away in the differential region and do not enter the main chamber. The remaining particles diffuse through a series of defining slits, Fig. 2.2, forming a well-collimated molecular beam. Two slits are usually used to define the molecular beam spatially. The defining slit is cooled to liquid nitrogen temperatures by a cold shield to minimize desorption of molecules from the slit surfaces. The cold shield is a 100 x 150 x 5 mm copper block with 0.635 mm o.d. copper tubing surrounding a 13 x 25 mm slot. It is attached to the main chamber side of the differential wall, and the defining slit is mounted directly to the cold shield, centered about the slot. The temperature is monitored by a K-type thermocouple attached directly to the copper block. The collimating slit is held in place with bolts and ceramic spacers directly to the defining slit. The width of the second slit can also be varied, but is usually 0.8-1.25 mm wide and 19 mm long. For the SiH experiments, the second slit was located 10 mm from the differential wall and 26 mm from the interaction region. For the NH_2 experiments, the second slit was placed 12 mm from the differential wall and 24 mm from the interaction region. Additional slits may also be used for further collimation.

The use of a rectangular molecular beam rather than a circular beam has two advantages. First, for beams of equivalent fluxes, a rectangular beam provides higher spatial resolution in the horizontal direction. Second, this configuration increases the detection sensitivity to molecules scattered/desorbed from the surface because molecules

emanating from a line source decrease in density as $1/r$ rather than the $1/r^2$ resulting from a point source.

2.2.3. SUBSTRATE CONTROL

The design of the IRIS apparatus allows for use of a variety of substrate types and sizes that can be mounted on one of two holders. The first substrate holder consists of a 2.5 cm aluminum rod machined at a 45° angle. The machined surface is an ellipse, measuring ~2.5 x 3.6 cm on its surface. The substrate is affixed directly to this surface either by Apiezon Wax W or double sided cellophane tape. The base of the aluminum rod has also been machined with a hole large enough to accommodate the manipulator arm rod.

The second substrate holder used in IRIS experiments has a more complicated design, Fig. 2.3. This holder starts with the basic design of the simpler substrate holder, a base made from a 2.5 cm aluminum rod machined at a 45° angle. A rectangular aluminum base plate (2.54 cm x 5.08 cm) is positioned above the machined surface of the base, thermally isolated by three sapphire balls (3.2 mm diameter). Sandwiched between the base plate and the cover plate (2.54 cm x 5.08 cm) is a ~15 cm long S-shaped nichrome wire, Fig. 2.3. The nichrome wire is electrically isolated with a MgO layer enclosed in Inconel casing. The cover plate, base plate, and base are held together by a 19 mm long machine screw. Substrates are mounted on the cover plate by means of two aluminum straps (2.54 x 0.95 cm) located on each end of the cover plate.

Both substrate holders can be mounted on an L-shaped manipulator arm attached

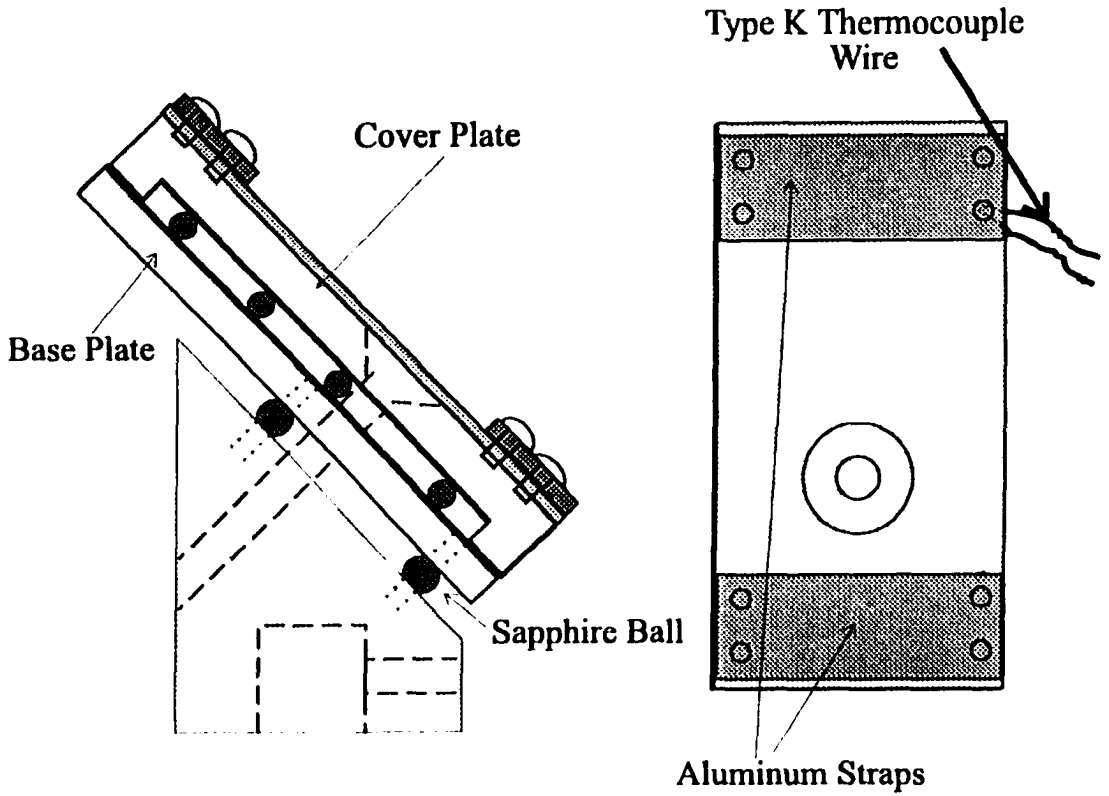

Figure 2.3. Detail of the heatable substrate holder (a) side view and (b) top view. Samples are held onto the head by means of the two aluminum straps. The thermocouple is held in contact with the substrate by placing it under the strap held by the set screws.

to a Vacuum Generator LTD bellows seal, linear motion feedthrough with a 10 cm translation capability, Fig. 2.1. The arm allows the substrate to be rotated precisely in and out of the path of the molecular beam and to be translated away from the interaction region. Translation of the substrate effectively varies the laser-surface distance. Typically, the substrate is positioned such that it is 2.0 to 5.0 mm from the laser beam.

Using the heatable substrate holder, the temperature of the substrate can be controlled from ambient temperature (~300 K) to ~750 K using an Omega CN9000A temperature controller with a K-type thermocouple wire. A Kepco ATE 6-25M power supply (6 V, 25 A) resistively heats the surface by passing current through the nichrome wire located between the cover plate and the base plate of the holder. The thermocouple wire is positioned under one of the aluminum straps on the holder, physically in contact with the front of the substrate, Fig. 2.3. The temperature is monitored with the Omega controller. Small (~1.5 x 5 cm) pieces of Si (100) wafers were used as substrates for all experiments described here. These substrates were cleaned with methanol prior to mounting on a substrate holder. No additional cleaning was done to remove the 30-80 Å of native oxide.

2.2.4. LASER SYSTEM

Monochromatic light at the desired excitation wavelength is produced with an excimer-pumped dye laser system. The Lambda Physik LPX 110i excimer laser (XeCl) emits 308 nm pulsed light with a pulse width of 17 ns at FWHM. The pump laser is typically operated with a pulse energy of 80-150 mJ at a repetition rate of 100 Hz. The

pulse energy can be adjusted to saturate the LIF signal, thus minimizing the problem of laser output power fluctuations. The excimer laser pumps a Lambda Physik Scanmate 2 dye laser to produce tunable light. Using the appropriate dye, output wavelengths can be scanned from 330 nm to above 1036 nm. In addition, our system can access wavelengths between 205 and 330 nm with the addition of either a KDP or a BBO doubling crystal. Pulse-to-pulse energy measurements can be made on the laser beam either before entering the chamber, after exiting the chamber or both simultaneously using a Molectron JD2000 Joulemeter Ratiometer with the appropriate head(s).

In the SiH system, light in the 409-415 nm range was produced using Furan-2 in the dye laser. The measured output power from the dye laser was 3-6 mJ per pulse (100 mJ pump energy). For the NH_2 data, light in the 596-598 nm range was produced using Rhodamine 6G in the dye laser. The measured output power of the light was 6-15 mJ per pulse (100 mJ pump energy).

The output of the dye laser is directed into the main chamber of the IRIS apparatus via a prism, a focusing lens, and a periscope. The laser beam enters the interaction region through a Brewster angle window, parallel to the substrate at a 45° angle from the molecular beam, Fig.2.1. The laser beam also passed through a ~1 mm diameter aperture 12 cm before the interaction region to reduce scattered light in the chamber. The focusing lens is a 50.8 mm diameter synthetic fused silica plano-convex lens (f = 2000 mm) placed outside the chamber, ~2200 mm from the interaction region. This produced a focal point prior to the interaction region, and gave a well-defined laser beam, <1 mm wide at the intersection of the molecular beam and the laser.

2.2.5. FLUORESCENCE DETECTION

The spatial dependence of the fluorescence excited by the laser beam is measured by imaging light from the interaction region on a Princeton Instruments (PI) gated ICCD camera. The camera is equipped with a microchannel plate image intensifier and both UV and IR enhancement coatings. The ICCD camera is electrothermally cooled to an operating range of -22 to -40 °C. The high gain of the microchannel plate and the low readout noise of the ICCD array result in a very sensitive detector capable of responding to a single photon. The ICCD has a 586 x 384 pixel display, corresponding to an area of 109 mm^2. For IRIS experiments, the detector is oriented with its long axis along the laser beam.

For fluorescence excitation spectra and reactivity experiments, the fluorescence is imaged directly onto the ICCD array, Fig. 2.1. The light is collected with two 50 mm diameter synthetic fused silica lenses. One lens (f = 300 mm) collects and collimates the light above the interaction region. The second lens (f = 75 mm) then focuses the fluorescence onto the ICCD array, Fig. 2.1. The optics demagnify the image so that the 12.9 mm long array views a region 55.0 mm long, making it possible to spatially resolve both the incident and scattered beam simultaneously. The total area imaged by the ICCD array is 1980 mm^2. Band pass filters can be used between the chamber and the lenses to reduce spurious signal due to scattered light from the laser or plasma source. Indeed, in both the SiH and NH_2 substrate temperature dependence studies, an IR cutoff filter (>800 nm) was used to eliminate light noise from the heated Si substrate.

The ICCD is located perpendicular to both the molecular beam and the laser

beam, directly above the interaction region, Fig. 2.1b. Typically, the ICCD is gated on 1.1 μsec after the laser fires, to avoid interference from scattered laser light. The gate width is varied according to the fluorescence lifetime of the species of interest. During all IRIS experiments, signals are generally collected for 10-100 accumulations. An accumulation is typically 2-60 seconds long with the laser firing at 100 Hz. Fewer accumulations decrease readout noise. The radiative lifetimes of SiH and NH_2 are very different, 534 ns and ~10 μs, respectively. For the SiH experiments described here, 10 accumulations of 20 seconds each were used with the laser firing at 100 Hz. For the NH_2 experiments, 3 accumulations of 60 seconds each were used. Pixel binning (typically 4 x 4 groups) is used to realize S/N ratio enhancement and minimize data collection time.

2.2.6. SYSTEM INTEGRATION

Figure 2.4 shows a schematic of the electronics configuration for the collection of reactivity data with the IRIS apparatus (dashed lines). The computer is a Pentium 133 MHz with 32 megabytes of RAM using PI WinView software, linked to the ICCD camera via a PI ST-130 detector controller. The controller is connected through its notscan output to a PI PG-200 programmable pulse generator ("notinhibit" in). Since fluorescence from multiple laser pulses are accumulated on the ICCD during the IRIS experiment, the controller sends a notscan signal to the pulse generator during image readout. The PG-200 in turn sends the trigger signal (trigger out) to the laser to initiate firing (trigger in). An oscilloscope is connected to the PG-200 to monitor the signal from

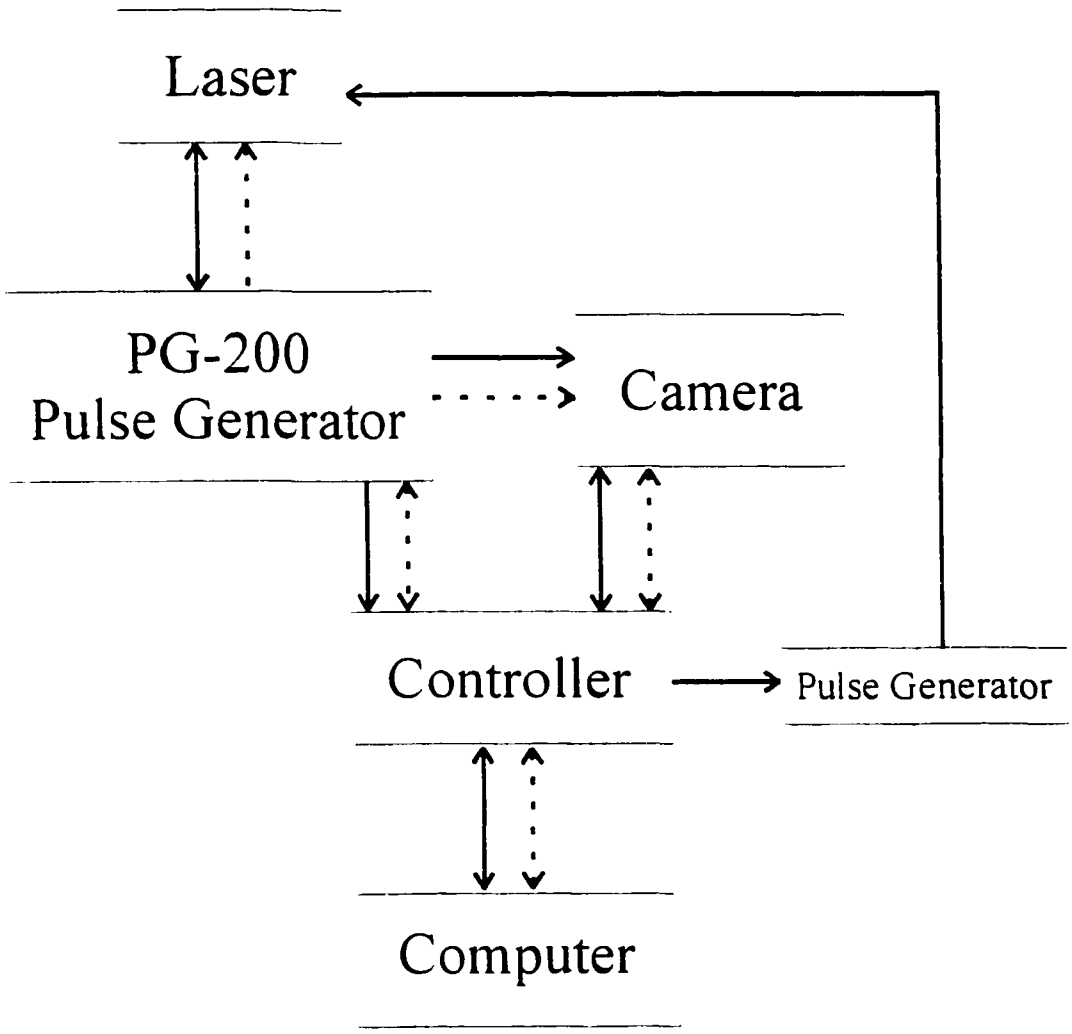

Figure 2.4. Schematic of the electronics configuration for collection of IRIS reactivity data (dashed lines) and for collection of rotational excitation spectra (solid lines).

the PG-200 to the laser.

The electronics configuration is slightly different when collecting an excitation spectrum for the species of interest in an IRIS experiment, Figure 2.4 (solid lines). The main difference between the configurations shown in Fig. 2.4 is that the laser now triggers the PG-200, rather than the PG-200 triggering the laser. This allows the laser to control the ICCD camera. The ST-130 sends a feedback signal to the dye laser to change the grating position. The ST-130 output signal is shortened by an HP pulse generator so the signal can be recognized by the laser.

2.2.7. ADDITIONAL FEATURES

The IRIS instrument at CSU has a number of features that have been added to the basic design employed at SNL. First, the apparatus has two ports which can accommodate a mass spectrometer, Fig. 2.1. These ports are located at the rear of the main chamber, to accommodate an in-line mass spectrometer and on the side of the main chamber, perpendicular to the molecular beam axis. The latter configuration would be employed to monitor molecules desorbing from the substrate. Addition of a mass spectrometer to IRIS will provide information on gas-phase species present in the molecular beam, and may be used to detect species scattered off the substrate.

Another feature is an additional set of laser ports located 90° from the laser ports used in a typical IRIS experiment. As noted in Fig. 2.1, the port located perpendicular to the substrate surface can be used for laser interferometry on the depositing film. This would allow us to determine *in situ* film deposition rates during processing. This port

may also be adapted for Raman or FTIR spectroscopy, allowing for additional *in-situ* surface characterization.

One difficulty with these experiments is that a significant amount of certain molecules may effuse around the standard slit configuration and scatter off the defining and collimating slits for the molecular beam. This results in a broad background of fluorescence along the laser path. To solve this problem, a liquid nitrogen cold shield was attached to the differential wall, Fig. 2.1. The temperature of the cold shield is monitored with a chromel/alumel thermocouple attached to the copper block. At the lowest temperatures attained (<100 K), the signal we observe is due primarily to the radical of interest *in the molecular beam*.

Other features include: a nitrogen purge, allowing for greatly reduced pump down times after the chamber is vented for short periods; a power-pressure-water interlock system that triggers the shut down of the pumping system in case of increased chamber pressure, power failure, or decreased water flow; and inlet and vent ports for liquid nitrogen feedthroughs for cooled molecular beam slits.[13]

2.3. SIMULATIONS

2.3.1. SURFACE REACTIVITY

To quantify the surface reactivity for the LIF signals acquired, a numerical simulation based on the experimental geometry is required.[12] This model calculates the spatial distribution of the radical number density in the molecular beam at the interaction region as well as the radical number density along the laser for molecules scattering from

the substrate surface. The molecular beam is simulated using known slit, laser beam, and substrate configurations and line-of-sight calculations to eliminate contributions from regions of the plasma orifice that are blocked by the slits. For this simulation, the modeler uses the following input parameters: slit widths, distance from the plasma orifice to the slits and laser, the laser-surface distance, the size of the detector array, a Gaussian to convolute the model, and a height matching factor to scale the calculated molecular beam to the experimental data.

To properly describe the spatial distribution of the molecules emanating from a surface, a specific scattering mechanism must be assumed. Our simulation allows for two mechanisms, either specular scattering or adsorption-desorption (cosine distribution about the surface normal). The calculated curve for scatter assumes all of the incident molecules leave the substrate surface. With specular scattering, the surface acts as a mirror and reflects the incoming molecules. The simulation of the specular scatter profile is calculated the same as the incident molecular beam profile, and accounts for different laser-orifice distances. With adsorption-desorption, the molecules interact with the surface and each area element of the surface is a potential source of desorbing molecules. The model does not account for any migration of molecules on the surface and assumes desorption is with a cosine angular distribution. To determine the reactivity of a specific molecule, the fraction of radicals scattering from the surface, S, is adjusted to best fit the experimental data. The surface reactivity, R, is defined as 1-S. A more complete explanation of this model is given elsewhere.[16]

IRIS experiments measure the relative densities of a molecule in the molecular

beam versus that of the molecule desorbing from a surface. Because the molecules may have different velocity distributions in the molecular beam than those scattered from the substrate, the relative densities in the laser beam may differ. This factor can be accounted for by scaling our reactivity measurements, using equation 2.1.

$$F_d = \frac{v_{mb}}{v_{scat}} \tag{2.1}$$

Where v_{mb} is the average velocity of molecules in the molecular beam, v_{scat} is the average velocity of molecules scattering from the surface, and F_d is the relative density change.

2.3.2. VELOCITY DISTRIBUTION MEASUREMENTS

2.3.2.1 MOLECULAR BEAM

For reactivity measurements, the laser normally enters the chamber at a 45° angle to the molecular beam, Fig. 2.1. For velocity measurements of a species in the molecular beam, the laser enters the main chamber perpendicular to the molecular beam and the axis of the focal plane of the ICCD detector, Fig. 2.5. The detector is positioned above the interaction region, oriented such that the long axis of the 2D image is along the laser path. To increase our spatial resolution, ICCD pixels were not binned as with our reactivity experiments. Each pixel images a 7.93×10^{-3} mm^2 area. Using short (e.g. 100 ns for NH_2) gate widths on the detector and variable gate delays (e.g. 1.5 - 11.5 μs for NH_2), we are able to take 'snap shots' of a radical's fluorescence in time with respect to the laser pulse.

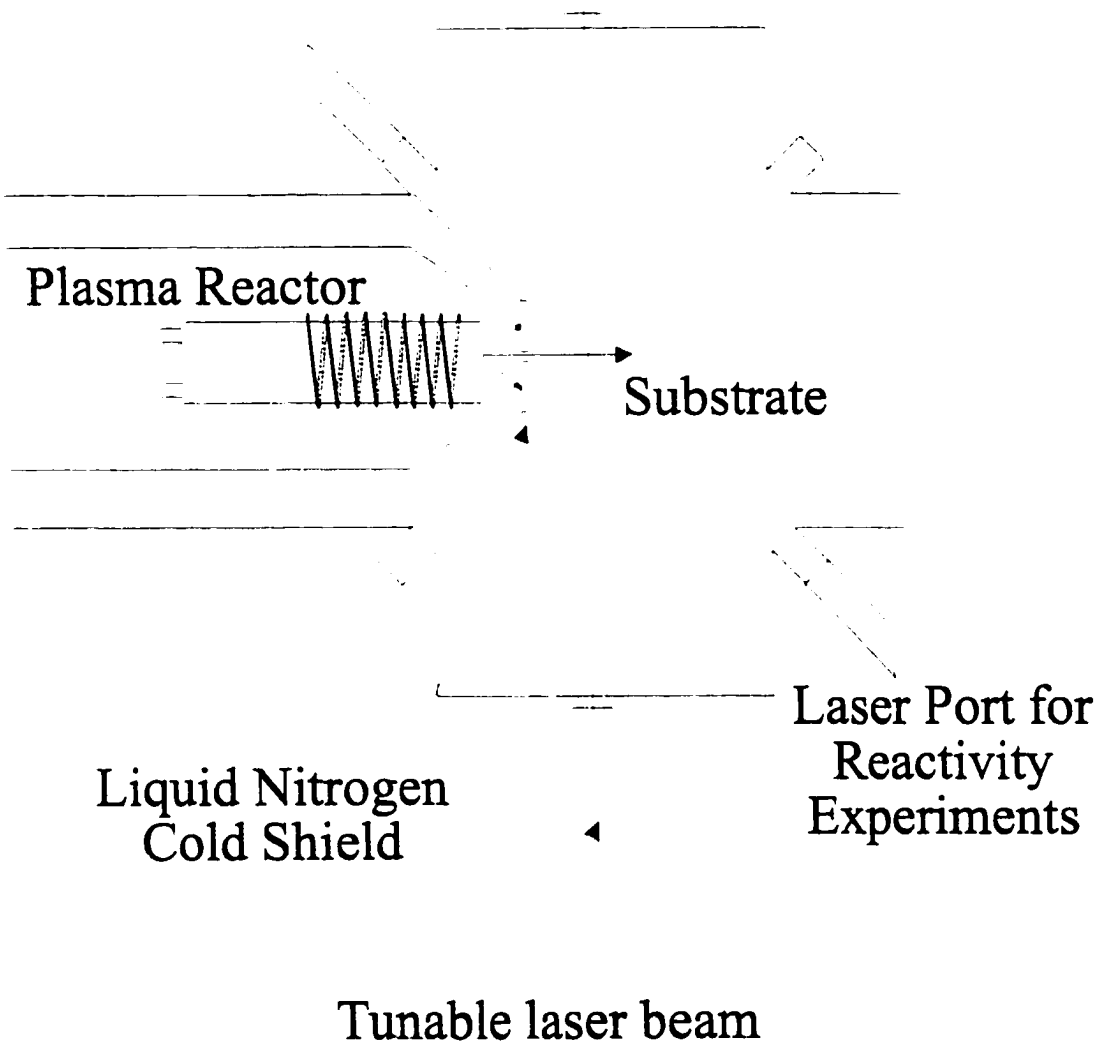

Figure 2.5. Schematic of the modified IRIS apparatus. The ICCD camera is located perpendicular to the plane of intersection of the laser beam and molecular beam.

For NH_2 experiments, NH_3 was introduced into the plasma chamber with a flow rate of 20.0 sccm. For the fluorescence excitation spectrum, a 45 W plasma is used and laser wavelengths are scanned from 596 to 598 nm. Spatial distribution measurements were made at applied rf powers of 25-150 W using 597.725 nm laser light to excite the NH_2 radicals in the molecular beam.[17] From the resulting two-dimensional images, one-dimensional plots of intensity versus distance are produced by averaging 40 rows of pixels (3.6 mm wide) along the central axis of the molecular beam path. A background swath of the same width is subtracted from the foreground plot.

For SiH experiments, a flow rate of 10.0 sccm of SiH_4 was used giving a pressure in the reactor of ~25 mTorr. Spatial distribution measurements were made at applied rf powers of 5-55 W using 411.240 nm laser light (J= 7.5) to excite the SiH radicals in the molecular beam. As with NH_2, 40 rows of pixels (3.6 mm wide) were averaged to create one-dimensional plots along the molecular beam path after subtracting a background.

The velocity of the specific radical in the molecular beam approximates its speed in the bulk of the plasma assuming an effusive beam is formed. An effusive source is created when the mean free path in the source is greater than the smallest dimension of the pressure-limiting orifice through which the beam passes.[18] With a typical operating pressure of ~ 1 x 10^{-4} Torr in the differential region, the mean free path is ≈500 mm. The smallest slit our molecular beam passes through is ≤ 2.5 mm and the hole in the plasma tube is 1.0 cm. Under these conditions, our molecular beam is best classified as effusive.

Using Monte Carlo techniques,[19] we simulate the velocity profile of the selected radical as a function of distance traveled between laser excitation and collection of

fluorescence. Our model assumes a Gaussian laser beam profile and calculates its time evolution using a Maxwell-Boltzmann distribution[3,20] of molecular velocities within the molecular beam.[21] As the molecular beam is well-collimated in the direction of propagation, the molecular velocity distribution is described by a Maxwell-Boltzmann distribution of speeds,[22] equation 2.2.

$$\frac{N_v}{N} = 4\pi\left(\frac{m}{2\pi kT}\right)^{3/2} v^2 e^{-mv^2/2kT} \tag{2.2}$$

where N_v/N is the number density at the velocity (v), m is the mass of the select radical, k is Boltzmann's constant, and T is the translational temperature, Θ_T. Curves are calculated for different Θ_T using a statistically significant number of psuedorandom numbers and are normalized to the same peak height. Other than the peak height, there are no adjustable parameters in the model. The Θ_T that best describes the data is determined by nonlinear least squares regression analysis.

An important input parameter for our model is the length of time a molecule has to travel along the molecular beam axis after excitation, before fluorescence collection, τ. This is determined by the time required for the laser to trigger and fire, experimentally determined as 1.1 μs; the gate delay, *d*; and gate width, *w*, equation 2.3.

$$\tau(\mu s) = d - 1.1 + \frac{1}{2}w \tag{2.3}$$

For NH_2 data, gate delays vary from 1.5 to 11.5 μs and the gate width was 100 ns, while for SiH data, gate delays vary from 1.45 μs to 2.95 μs and the gate width was 300 ns.

2.3.2.2. SCATTERED RADICALS.

We have also developed a model for determining $\Theta_{T\,scat}$ based on a Maxwell-Boltzmann distribution of velocities. The velocity distributions of radicals scattering from a substrate can be directly measured from the data by determining the distance the LIF signal moves on the ICCD from the surface normal as the gate delay of the ICCD is increased. Unlike the model for determining the velocity distribution in the molecular beam, the model for the scattered molecules relies on knowing the angular distribution of the desorbing species. The model also accounts for the x, y, and z components of velocity for the scattering molecules. It is assumed that the molecule's velocity distribution is independent of the angle of desorption. The model only calculates the velocity component of each simulated molecule along the surface normal.

For velocity distribution measurements of molecules scattering from a surface, the standard IRIS configuration is used–i.e. the laser enters the chamber at a 45° angle with respect to the molecular beam and the camera is oriented along the laser axis. This configuration is used to minimize any signal interference between the plasma molecular beam and the scattering molecules. For velocity distribution measurements of NH_2

scattering from surfaces, the gate delay is stepped in 2.0 μs increments from 1.45 to 9.45 μs. The gate width was increased to 500 ns to improve S/N. Appendix 1 gives the actual computer code for the program and a more detailed overview of the velocity distribution simulation.

REFERENCES

1. K. E. Spear and J. Carlson, Electrochem. Soc. Interface **2**, 39 (1993).

2. R. Reif and W. Kern in *Thin Film Processes II*, edited by J. L. Vossen and W. Kern (Academic Press, Inc., San Diego, CA, 1991), p. 525.

3. Michael A. Lieberman and Allan J. Lichtenberg, *Principles of Plasma Discharges and Materials Processing*, (John Wiley & Sons, Inc., New York, 1994).

4. H. W. Lehmann in *Thin Film Processes II*, edited by J. L. Vossen and W. Kern (Academic Press, Inc., San Diego, CA, 1991), p. 673.

5. F. D. Egitto and L. J. Matienzo, IBM J. RES. Develop. **38**, 423 (1994).

6. N. Morosoff in *Plasma Deposition Treatment, and Etching of Polymers*, edited by R. d'Agostino (Academic Press, Inc., New York, 1990), p. 528.

7. J. M. Jasinski and S. M. Gates, Acc. Chem. Res. **24**, 9 (1991).

8. M. Masi, B. Giambattista, L. Canzi and S. Carra, Chem. Eng. Sci. **49**, 669 (1994).

9. We follow Herzberg's example and use the term "radical" to refer to transient intermediate species, rather than limiting the term to only those species with an unpaired electron. G. Herzberg, *The Spectra and Structures of Simple Free Radicals*; Cornell University: Ithaca, NY, 1971.

10. R. d'Agostino in *Plasma Deposition, Treatment and Etching of Polymers*, edited by R. d'Agostino (Academic Press, San Diego, 1990), p. 528.

11. G. Bruno, P. Capezzuto and G. Cicala in *Plasma Deposition of Amorphous Silicon-Based Materials*, edited by G. Bruno, P. Capezzuto, and A. Madan (Academic Press, Boston, 1995), p. 27

12. P. Ho, W. G. Breiland and R. J. Buss, J. Chem. Phys. **91**, 2627 (1989).

13. E. R. Fisher, P. Ho, W. G. Breiland and R. J. Buss, J. Phys. Chem. **96**, 9855 (1992).

14. R. J. Buss, P. Ho and M. E. Weber, Plasma Chem. Plasma Process. **13**, 61 (1993).

15. E. R. Fisher, P. Ho, W. G. Breiland and R. J. Buss, J. Phys. Chem. **97**, 10287 (1993).

16. K. H. A. Bogart, J. P. Cushing, and E. R. Fisher, J. Phys. Chem. **101**, 10016 (1997).

17 K. Dressler, and D. A. Ramsey, Phil. Trans. A **251**, 553 (1959)

18 M. A. D. Fluendy and K. P. Lawley, *Chemical Applications of Molecular Beam Scattering*, (Chapman and Hall: London, 1973).

19 M. H. Kalos, P. A. Whitlock, Monte Carlo Methods. Volume 1: Basics, Wiley, New York, 1986; S. Jain, Monte Carlo Simulations of Disordered Systems, World Scientific, New Jersey, 1992.

20 J. B. Anderson and J. B. Fenn, Phys. Fluids **8**, 780 (1965)

21 W. Jitschin and G. Reich, J. Vac. Sci. Technol. A **9**, 2752 (1991)

22. R. A. Serway, *Physics for Scientists and Engineers, 2nd Edition* (Saunders College Publishing: New York, 1986)

CHAPTER 3

VELOCITY DISTRIBUTIONS FOR NH_2 RADICALS IN NH_3 PLASMA MOLECULAR BEAMS

3.1. INTRODUCTION

Ammonia and silane plasmas are used extensively in the microelectronics industry as a nitrogen source for plasma deposition of amorphous hydrogenated silicon nitride, a-SiN_x:H and other metal nitride films.[1] Thin films of a-SiN_x:H are used as gate dielectrics and barrier coatings in microelectronic devices,[2] as capacitors in dynamic random access memory (DRAM) cells[3] and in the microfabrication of sensors and actuators.[4] NH_3 plasmas are also used to modify the surfaces of polymers to increase wettability and chemical bonding in the manufacturing of composite materials.[5,6] Despite this wide spread use, much remains unknown about the underlying mechanisms of film deposition and polymer surface modification using ammonia-based plasmas. Specifically, the role of gas-phase radicals in these processes is unclear and little work has been done to characterize the basic interactions of NH_x radicals with Si or a-SiN_x:H surfaces.

To fully understand the chemistry of low-temperature plasmas, knowledge of the energy partitioning between species must also be acquired. Energetics for plasma radicals are often difficult to obtain because discharges are non-equilibrium systems that are not always well characterized by the laws of thermodynamics. Moreover, kinetic energy

distributions of plasma species are relatively difficult to determine.[7] Although NH and NH_2 are the predominant radicals in NH_3 plasmas,[8,9] they have not been well studied.[10] With NH_2 the literature is extremely sparse. Perrin and coworkers have reported LIF measurements of NH_2 resulting from the Hg-photosensitized decomposition of NH_3.[11] Vervloet and Mirienne-Lafore have also examined the rotational spectrum of NH_2 in a 27 MHz rf discharge using high resolution photographic emission spectroscopy and LIF.[12] Neither of these studies, however, characterized the energy distributions of the NH_2 radicals or their interactions with surfaces.

The imaging of radicals interacting with surfaces (IRIS) method combines laser-induced fluorescence (LIF) and plasma molecular beam techniques to obtain state-specific surface reactivity data from plasma radicals.[1,13,14,15] In IRIS experiments, the LIF were imaged using an electronically gated, intensified charge-coupled device (ICCD) detector for collection of LIF signals. By exploiting the time gating on the ICCD, we have collected and modeled velocity distributions of NH_2 radicals in an NH_3 plasma molecular beam. This was the first time the IRIS method has been used to directly determine the translational temperature of a plasma species.

For these experiments, a reasonably long fluorescence lifetime (ca. 500 ns)[16] was required to accurately determine translational temperatures for a particular molecule in our complex molecular beam. The extremely long fluorescence lifetime of NH_2 (≈ 10 μs)[17] made it an ideal molecule for these experiments. The results presented here demonstrate that the translational temperature (Θ_T) of NH_2 radicals could be well described using a Maxwell-Boltzmann distribution function. This technique will be valuable for measuring

velocity distributions of any radical with a sufficiently long fluorescence lifetime. To further explore plasma radical energetics, we have also determined Θ_T for NH_2 radicals as a function of applied rf plasma power.

Finally, our experimental method was sensitive enough to observe the velocity of molecules scattering off a surface. Here preliminary velocity data for NH_2 molecules scattered from a Si (100) surface placed in the path of the molecular beam are presented.

3.2. RESULTS AND DISCUSSION

3.2.1. MOLECULAR BEAM NH_2

Results presented here are the first measurements of velocity distributions for NH_2 in a plasma molecular beam. A fluorescence excitation spectrum for NH_2 radicals is shown in Fig. 3.1. The spectroscopy of NH_2 is well known,[17,18] and comparison to literature spectra indicates the fluorescing species is indeed NH_2.[18,19] The most prominent spectral line in the 596-598 nm region is three overlapping rotational bands (3_{03}-3_{13}; 4_{04}-4_{14}; and 5_{05}-5_{15}), of the $\Sigma(0,9,0)$ vibronic state, for the $^2A_1$-$^2B_1$ electronic transition. This transition (λ = 597.725 nm), was chosen for our measurements because of its high fluorescence intensity.

Cross sectional LIF data for NH_2 molecules (100 W NH_3 plasma) at three different gate delay times are shown in Fig. 3.2. As the gate delay increases, the LIF signal broadens and shifts away from the laser as expected in a effusive molecular beam. The density of excited NH_2 radicals also decreases as a function of the fluorescence lifetime. These effects reduce the signal to noise ratio (S/N) in our data as a function of time. They

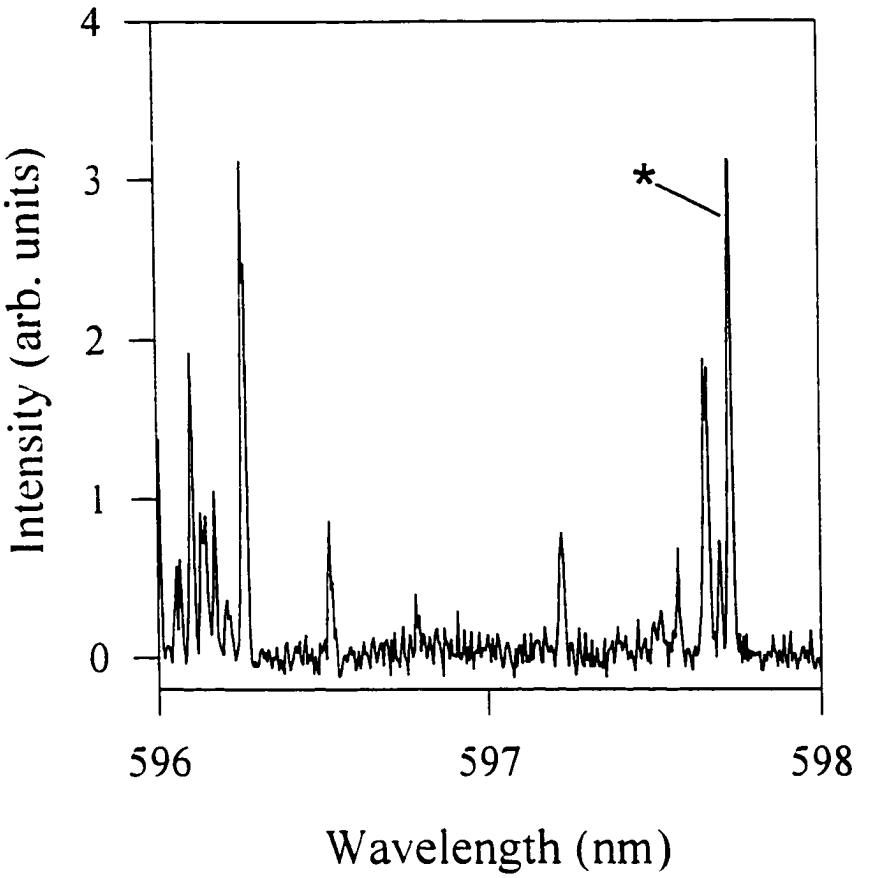

Figure 3.1 Experimental fluorescence excitation spectrum of NH_2 in the molecular beam formed from a 100% NH_3 plasma (45 W, 20 sccm). The spectrum was taken with 0.005 nm steps on the dye laser. The (*) denotes the 597.725 nm absorption line used in velocity distribution measurements.

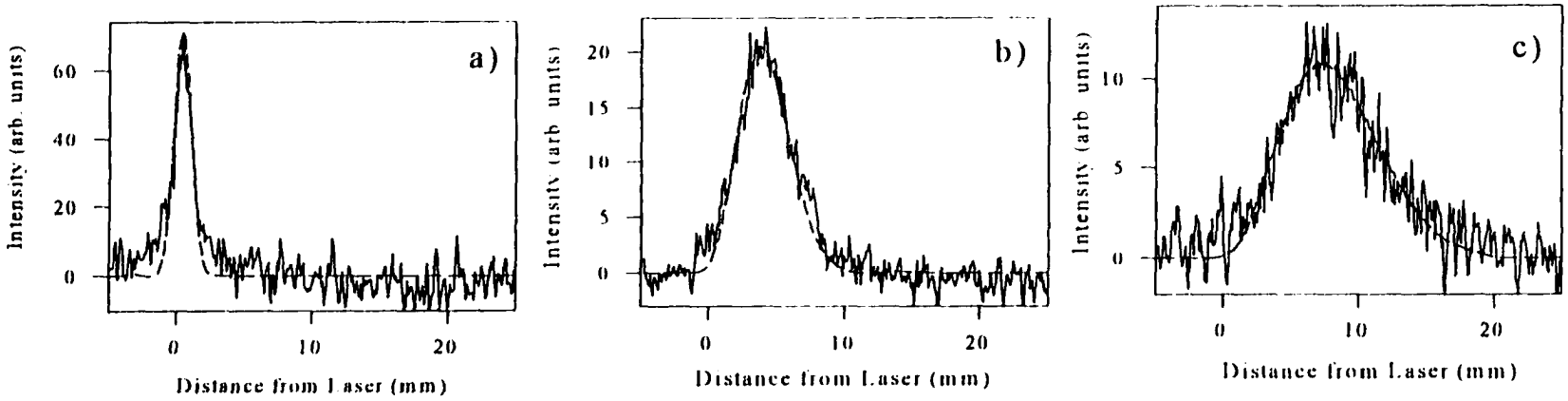

Figure 3.2 Cross sectional data for NH_2 radicals in a molecular beam form from a 100 W NH_3 plasma (solid line) at three different gate delays: (a) 1.5 μs delay (τ = 0.45 μs), (b) 5.5 ms delay (τ = 4.45 ms), (c) 9.5 ms delay (τ = 8.45 ms). Simulated curves using model described in the text are also shown (dashed lines). The curves correspond to (a) Θ_1 = 600 K, (b) Θ_1 = 600 K, and (c) Θ_1 = 620 K.

have the benefit, however, of a greater net movement of the excited NH_2 molecules which minimizes error

Using the velocity model, we simulated the velocity profiles for each τ to derive Θ_T for the NH_2 radicals in the molecular beam, Fig 3.2. Clearly, there is good agreement between the data and the simulated curves, indicating the Maxwell-Boltzmann distribution is valid for these systems at all τ. At τ approaching zero, the radicals have not traveled very far from the laser, Fig. 3.2.a. Here, the distributions observed were essentially Gaussian, supporting the model's assumption that the laser had a Gaussian profile.

Velocity distributions were also obtained for NH_2 radicals using different applied rf plasma powers, Table 3.1. Using five different τ, we derived an average Θ_T for NH_2 with applied rf plasma powers from 25 to 150 W. Data taken with the shortest gate delay (d = 1.5 μs, τ = 0.45 μs) were not included in the average because the resolution of the camera does not allow an accurate estimation of the distance traveled in this relatively short time.

The average Θ_T increased linearly with applied rf power from 512 ±8 K for a 25 W NH_3 plasma, to 664 ± 35 K at 150 W, Table 3.1.[20] The increase in Θ_T was not directly proportional to the increase in plasma power because there were many pathways for energy dissipation in the system, including increased fragmentation of molecules,[21] and increased vibrational and rotational energies of plasma species.[9] It has been shown that a large fraction of the energy absorbed by electrons from the electric field created in a discharge is transferred to gas molecules in the form of vibrational excitation.[22] At high gas pressures, this vibrational energy is rapidly converted to translational energy.[23]

Table 1

Q_T for NH_2 radicals [a]

rf power (W)	Pressure [b] (mTorr)	τ (μs)					Avg Θ_t (K) [c]	Avg. v(ms^{-1}) [d]
		2.45	4.45	6.45	8.45	10.45		
25	30.9 ± 0.6	500	518	515	520	510	512 ± 8	823 ± 7
50	32.1 ± 0.1	530	515	520	530	515	522 ± 8	831 ± 7
75	36.6 ± 0.1	625	600	600	585	545	591 ± 29	884 ± 22
100	40.3 ± 0.4	590	600	610	620	600	604 ± 211	894 ± 8
150	48.3 ± 0.4	710	690	655	635	630	664 ± 35	937 ± 25

[a] Calculated from the model described in text.
[b] Pressure of plasma at the given rf power.
[c] The mean Θ_t for the τ listed. Errors reported are one standard deviation from mean.
[d] Average velocity of NH_2.

To determine Θ_T accurately in these experiments, it is essential to have a near collisionless environment in the molecular beam. Using differential pumping and operating in a high vacuum environment minimizes collisions in our molecular beam. The assumption of a Maxwell-Boltzmann distribution of velocities in the molecular beam seems well justified as our data were accurately reproduced by this model at all gate delays and for all plasma powers. Furthermore, there was good agreement between Θ_T values measured at different τ for a particular plasma power, Table 3.1. This indicates the molecules do not undergo significant collisional cooling in the molecular beam after excitation for applied powers of 25-100 W

At an rf power of 150 W, however, we observed a steady decrease in Θ_T with increasing τ, Table 3.1.[24] The most probable cause for the cooling trend in these data is an increased number of collisions in the molecular beam. At relatively high rf powers, there is an increased probability for fragmentation of precursor molecules.[7] Indeed, as the rf power was increased, we observed a concomitant increase in the overall pressure in the plasma source for the same NH_3 flow (20 sccm), Table 3.1. At 150 W, the pressure in the source rises to ≈ 48 mTorr, resulting in a shorter mean free path. This leads to an increased pressure and number of collisions in the molecular beam, thereby decreasing the translational energy of the NH_2 as a function of delay time.

3.3.2. SCATTERED NH_2

In addition to velocity profiles for NH_2 radicals in our molecular beam, we were also interested in measuring the velocity of species scattered from surfaces and the surface reactivity of NH_2 using NH_3-based plasmas. Fig. 3.4 shows an ICCD image taken with a

Si substrate placed in the path of the molecular beam, 8.4 mm from the laser. The separation of the LIF signals from NH_2 in the molecular beam approaching the surface and NH_2 molecules scattering from the surface is visible. These preliminary results show a significant number of NH_2 radicals scatter from the substrate, indicating a low surface reactivity for NH_2, these results will be developed further in Chapter 5

The preliminary data of Fig. 3.3 show that the scattered NH_2 radicals had a much broader distribution along the laser than did the NH_2 in the molecular beam. This is indicative of an adsorption–desorption scattering mechanism, resulting in a cosine distribution about the surface normal. Furthermore, the relatively large signal due to scattered species was much closer to the laser than the signal resulting from NH_2 in the molecular beam. This would seem to indicate the scattered molecules are moving much more slowly than radicals in the molecular beam, however, it must be remembered that while the molecules in the molecular beam have one direction of motion, the scattered molecules have three components to their velocity. A model to accurately describe the velocity of the scattered molecules is described in Appendix 1. From these calculations, we were able to determine the extent of translational energy accommodation on the surface as described in Chapter 5.

3.4. CONCLUSIONS

The present results show our data provide much needed energetic information about plasma radicals, specifically translational temperatures. For NH_2 radicals in an NH_3

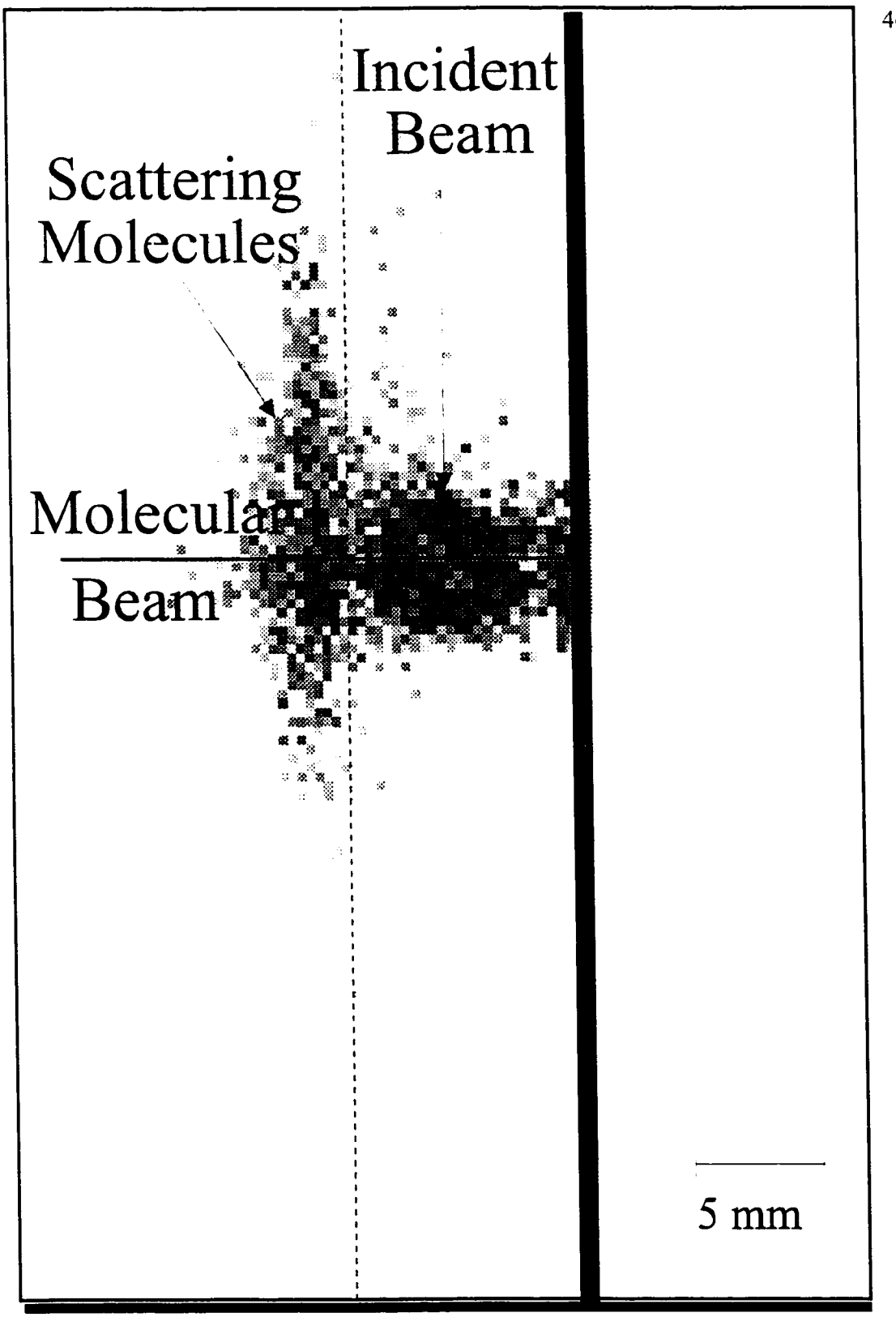

Figure 3.3 ICCD of LIF signals from NH_2 molecules in the molecular beam and scattering from a 300 K Si surface using a 50 W NH_3 plasma, d = 6.00 μs and w = 500 ns.

plasma molecular beam, the spatial and temporal profiles were well described using a Maxwell-Boltzmann velocity distribution. This is strong evidence that neutral species in this system are at equilibrium. The velocity of the molecules increased linearly with applied rf plasma power, indicating at least some of the power is dissipated through increased molecular motion. In addition, data presented for scattered species indicated that we can acquire spatially and temporally resolved profiles for molecules emanating from a surface. Thus, with this new technique we will be able to determine the energetics of many neutral species in plasmas as well as molecules scattered from a surface *during* plasma deposition or etching.

REFERENCES

1. E. R. Fisher, P. Ho, W. Breiland, and R. J. Buss, J. Chem. Phys. **96,** 9855 (1992).

2. F. S. Galasso, R. D. Veltri, W. J. Croft, Am. Ceram. Soc. Bull. **57,** 453 (1978); J. J. Gebhart, R. A. Tanzilli, T. A. Harris, J. Electrochem. Soc. **123**, 1578 (1976).

3. S. Koseki, A. Ishitani, J. Appl. Phys. **72**, 5808, (1992).

4. X. Zhang, C. P. Grigoropoulos, Rev. Sci. Instrum. **66**, 1115, (1995).

5. E. M. Liston, L. Martinu, and M. R. Wertheimer, J. Adhesion Sci. Technol. **7,** 1091 (1993).

6. J. E. Klemberg-Saphieha, O. M. Kuttel, L. Martinu, and M. R. Wertheimer, J. Vac. Sci. Technol. **A6,** 2975 (1991).

7. M. A. Lieberman and A. J. Lichtenberg, *Principles of Plasma Discharges and Materials Processing* (Wiley: New York, 1994), p. 35.

8. G. P. Miller, J. K. Baird, J. Phys. Chem. **97**, 10984 (1993).

9. P. Ho, R. J. Buss, R. E. Loehman, J. Mater. Res. **4**, 873 (1989).

10. G. W. Robinson, M. McCarty Jr., J. Chem. Phys. **30**, 999 (1959); S. N. Foner, R. L. Hudson, J. Chem. Phys. **45**, 40 (1966).

11. T. Fuyuki, B. Allain, J. Perrin, J. Appl. Phys. **68**, 3322 (1990).

12. M. Vervloet, M. F. Merinne-Lafore, Can. J. Phys. **60**, 49 (1980).

13. K.H.A. Bogart, J. P. Cushing, E. R. Fisher, Chem. Phys. Lett. **267**, 377 (1997)

14. P. R. McCurdy, K. H. A. Bogart, N. F. Dalleska, and E. R. Fisher, Rev. Sci. Instrum. **68**, 1684 (1997).

15. K. H. A. Bogart, J. P. Cushing, and E. R. Fisher, J. Phys. Chem. **101**, 10016, (1997).

16. Radicals with much shorter lifetimes can also be studied by changing the magnification optics. Currently, we have studied molecules with fluorescence lifetimes as short as 534 ns.

17. J. B. Halpern, G. Hancock, M. Lenzi, K. H. Welge, J. Chem. Phys. **63**, 4808 (1975).

18 C.-H. Chang, S.-C. Lin, and Y.-T. Chen, J. Molec. Spectrosc. **169**, 427 (1995).

19. S. C. Ross, F. W. Birss, M. Vervloet, and D. A. Ramsay, J. Molec. Spectrosc. **129**, 436 (1988).

20. The errors with these values represent one standard deviation from the mean of the temperatures at different τ. The correlation coefficient for a linear regression fit to these data yields r = 0.977.

21. M. Hirose, in: *Plasma Deposited Thin Films*, edited by J. Mort, and F. Jansen, CRC Boca Raton, FL, 1986, p. 31.

22. M. I. Boulos, P. Fauchais, E. Pfender, *Thermal Plasma Fundamentals and Applications*, Plenum, New York, 1994.

23. A. V. Phelps, in: *Chemical Reactions in Electric Discharges*, R. F. Gould (Ed.) American Chemical Society, Washington DC, 1969.

24. The 75 W data appear to have a similar decrease in Θ_T with increasing τ. Additional data sets show, however, $\Theta_T = 600 \pm 50$ K at all τ, with no observed decrease at longer τ.

CHAPTER 4

EFFECTS OF PLASMA PROCESSING PARAMETERS ON THE SURFACE REACTIVITY OF SiH IN SILANE PLASMAS DURING DEPOSITION OF a-SiH

4.1. INTRODUCTION

Ho, Breiland, and Buss (HBB) first used the IRIS technique to study SiH radicals from a 100% SiH_4 plasma on a 300 K Si substrate.[1] Substrate temperature dependence measurements, however, were not performed in the original experiments. Here, we present results for SiH radicals from a 100% SiH_4 plasma on 300 K Si substrates to test the performance of our apparatus. We also present results for the substrate temperature dependence (300-673 K) of SiH molecules at the surface of a depositing a-Si:H film. In addition, the translational temperature of SiH in the molecular beam has been determined for several different applied plasma powers.

4.2. RESULTS.

4.2.1. SPECTROSCOPY OF SIH.

The spectral selectivity of the LIF technique was used to identify and study SiH separately from the other species in the molecular beam. Figure 4.1 shows an experimental fluorescence excitation spectrum for SiH obtained with laser wavelengths

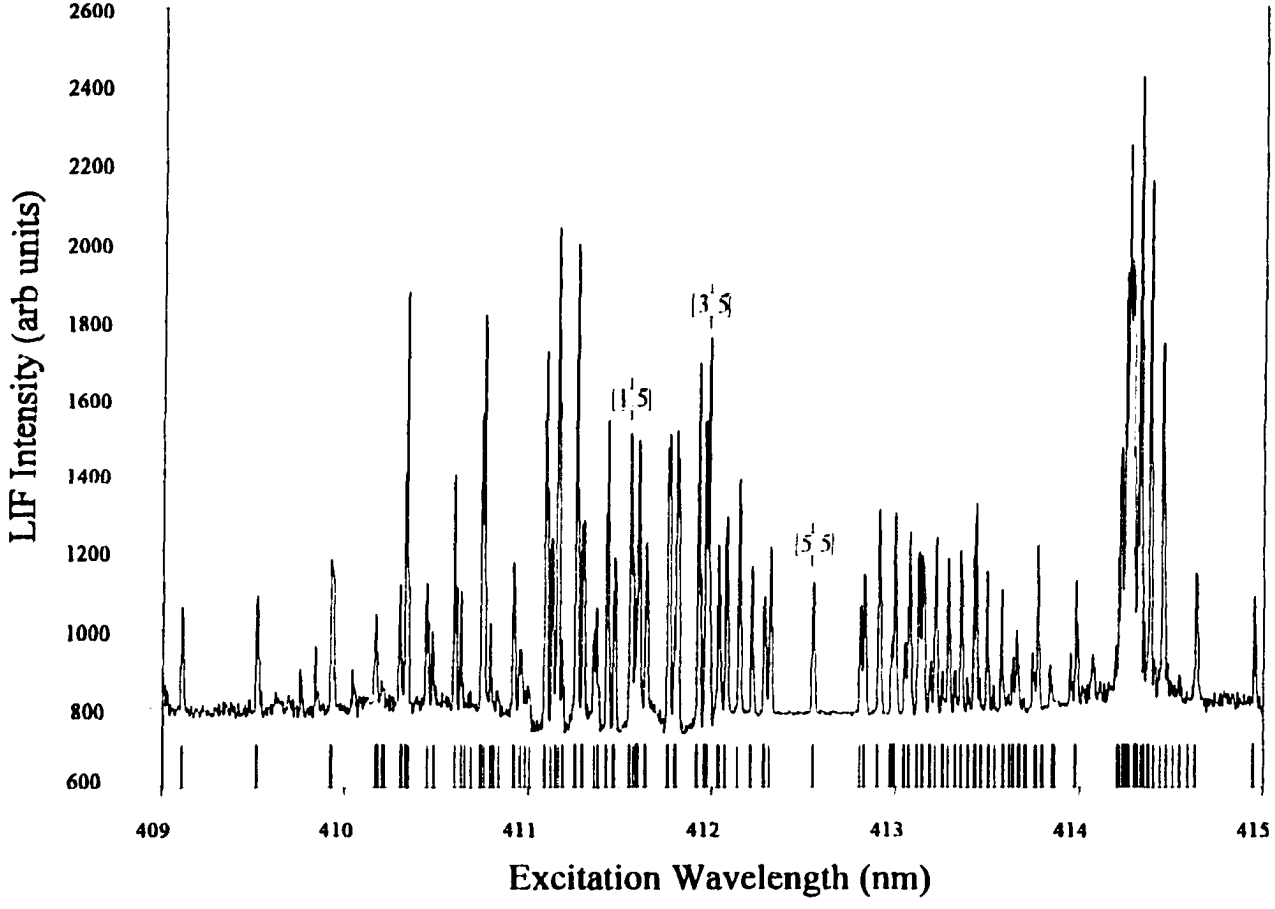

Figure 4.1. Experimental fluorescence excitation spectrum of SiH in the molecular beam formed from a 100% SiH_4 plasma. The lines labeled [1.5], [3.5], and [5.5] are the R_{21} (J=1.5), Q_{21} (J=3.5), R_{22} (J=5.5) rotational lines used in this study. Plotted below the experimental spectrum are the calculated line positions for the SiH rotational states.

between 409 and 415 nm. Also shown in Fig. 4.1 are the calculated line positions from a numerical simulation of the well-known spectroscopy of the SiH $A^2\Delta$-$X^2\Pi$ transition.[2,3,4,5] The experimental spectrum was not corrected for variations in laser power and was obtained using a broader molecular beam than was used for the reactivity measurements to improve signal levels. The good agreement between the calculated line positions and experimental spectra shows the fluorescing species was indeed SiH.

The IRIS method for measuring radical reactivities is not adversely affected by optical saturation because the signal from desorbing molecules is normalized to the signal from the incident molecular beam. All IRIS measurements reported here were performed under optically saturated conditions. Since we are only concerned about the ratio of incoming molecules to scattered molecules in a steady state, measurements are unaffected by operating in a saturated regime. Saturation effects in IRIS experiments have been discussed in detail previously.[1,6]

4.2.2. SPATIAL DEPENDENCE OF SIH.

The ICCD camera allows two dimensional imaging of LIF from SiH molecules. Figure 4.2 displays the images obtained for SiH using a 100% SiH_4 plasma as the molecular beam source. These images have been corrected for background signal from scattered laser light and plasma emission with no additional manipulations. In Fig. 4.2, the laser was propagating from the bottom of the image to the top and the molecular beam was propagating from left to right across the image. The laser was tuned to 411.546 nm, which excites the R_{21} (J=1.5) state of SiH. Figure 4.2a shows an image of LIF from SiH in the molecular beam as it intersected the laser beam. Figure 4.2b shows the fluorescence

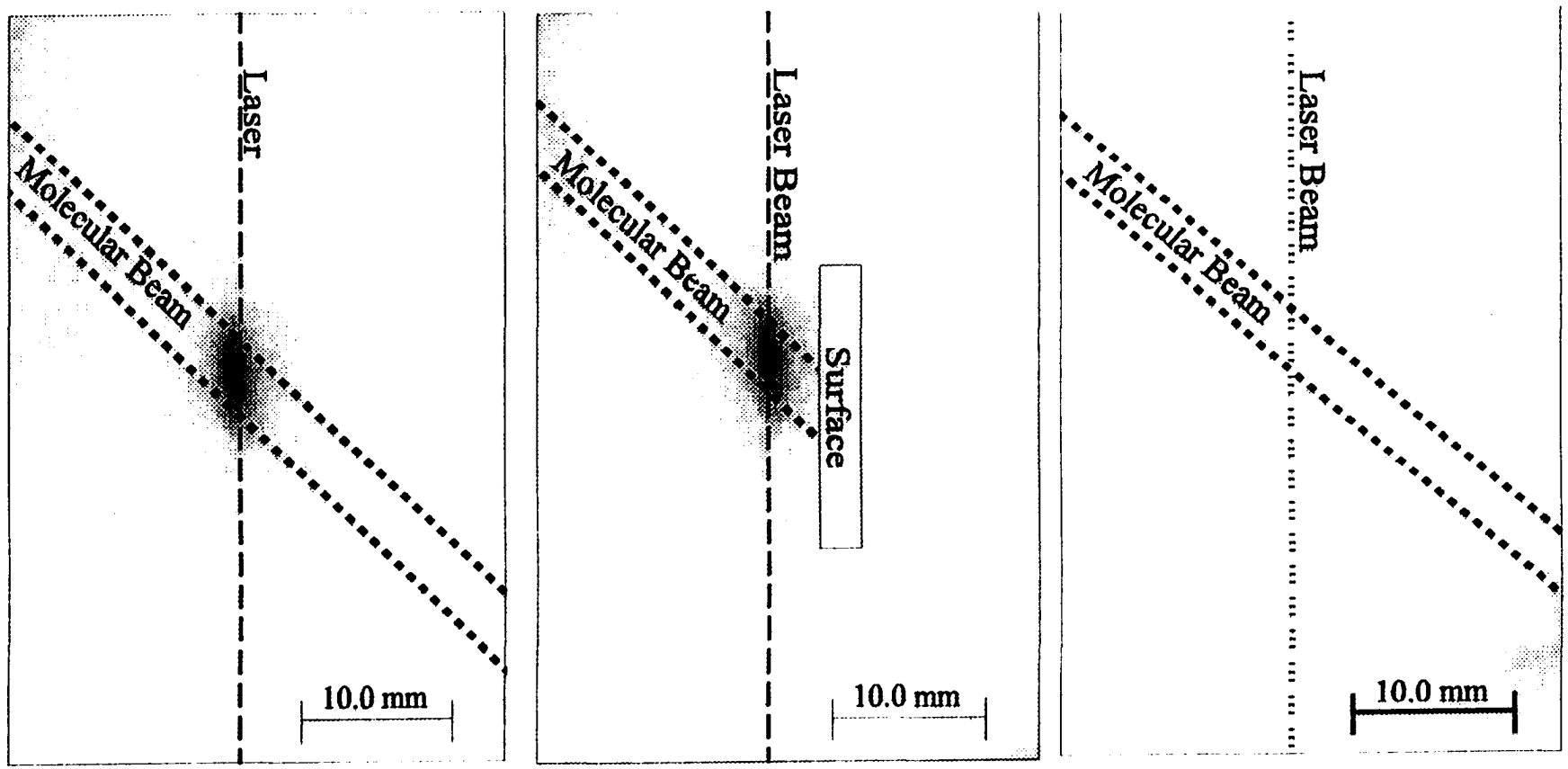

Figure 4.2. ICCD images of LIF signals produced by SiH molecules (a) in the molecular beam only (no substrate) and (b) with the substrate in the path of the molecular beam, 2.5 mm from the laser. The image shown in Figure (c) is the difference between images (a) and (b), corresponding to SiH molecules scattering from the substrate. The dashed lines indicate the location of the molecular beam and the laser beam in the images. LIF signals with the highest intensity appear as the darkest regions in the image. A sum of four data sets is shown.

with the Si substrate (300 K) rotated into the path of the molecular beam, 2.5 mm from the laser beam. This signal corresponds to SiH molecules both in the incident molecular beam and scattering off the surface of a depositing a-Si:H film. The difference between Fig. 4.2b and 4.2a is shown in Fig. 4.2c, corresponding to SiH molecules emanating from the substrate. From this figure, it is clear very little SiH was scattering off the depositing film. The physical location of the SiH molecules is given by the images in Fig. 4.2.

To directly compare with previous IRIS results for SiH from a SiH_4 plasma, vertical cross sections of the image data shown in Fig. 4.2 were taken. Combining the signals for a 1.16 mm wide strip along the laser beam for each image in Fig. 4.2 resulted in the three curves shown in Fig. 4.3. The LIF signal from molecules in the incident molecular beam was nearly identical to the LIF signal taken with the substrate in the path of the molecular beam. This indicates there was very little, if any, scatter from the substrate. The data in Fig. 4.3 were very similar to those produced with the original IRIS apparatus equipped with a linear diode array [1]

The observation that signals from the scattered/desorbed SiH molecules were only a few percent of the signals from the SiH in the molecular beam suggests that most of the SiH molecules reacted at the surface. From the data, the scattering ratio was determined. This ratio is defined as:

$$S = \frac{F_{scat}}{F_{mb}} \tag{4.1}$$

where F_{scat} is the flux of molecules emanating from the surface and F_{mb} is the flux of

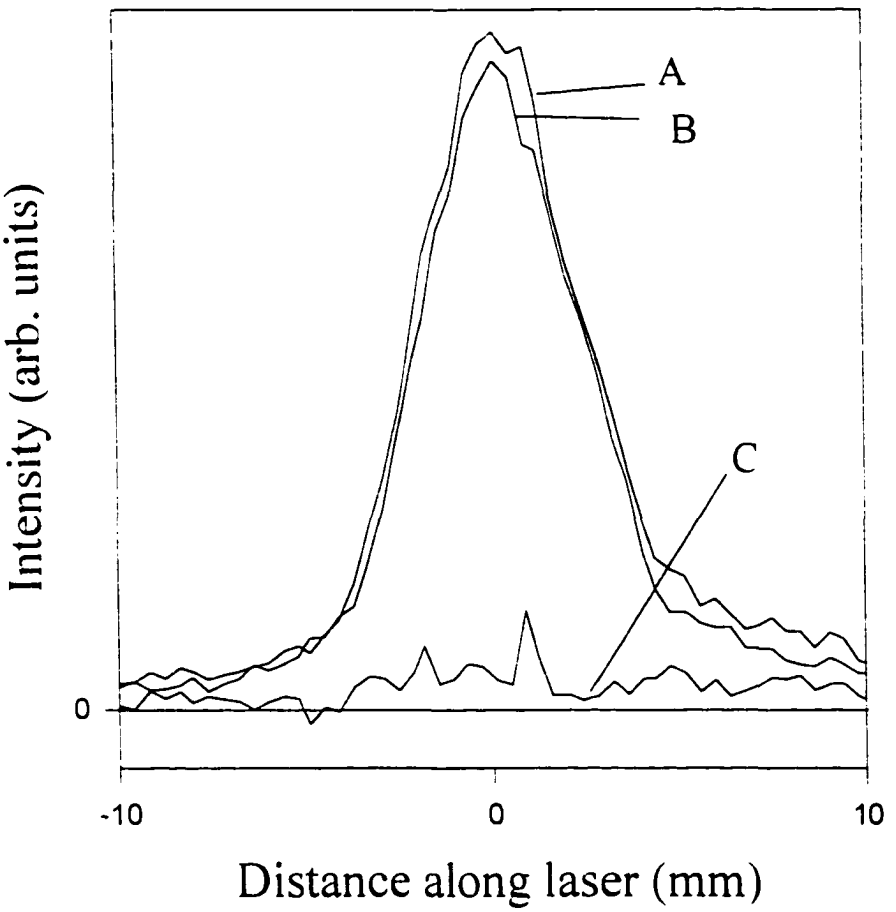

Figure 4.3. Cross-sectional data from the images shown in Figure 4.2. The y-axis is the signal intensity of a 1.16 mm swath centered along the laser beam path. The x-axis corresponds to the distance along the laser beam, where the zero point corresponds to the intersection of the laser and the molecular beam. The three curves correspond to LIF signals for SiH observed in the incident molecular beam (A), with the substrate in the path of the molecular beam (B), and for SiH desorbing from the surface (C).

incoming molecules. The reactivity, R, of a particular radical with a substrate is then defined as:

$$R = 1 - S \tag{4.2}$$

Hence, the reactivity can be considered as the probability that a radical will disappear from the gas phase as a result of its interaction with the substrate. HBB measured a high reactivity of 0.94 on a room temperature Si substrate.[1] Our data indicated a reactivity of 0.95 ± 0.05 for SiH molecules at the surface of a depositing a-Si:H film, in excellent agreement with HBB.

4.2.3. TEMPERATURE DEPENDENCE OF SIH.

Industrial scale deposition of a-Si:H films are normally performed at substrate temperatures well above 300 K.[7] It is imperative, therefore, to measure radical reactivities at elevated substrate temperatures in order to achieve full understanding of these processes. The previous SiH reactivity measurements were performed only on 300 K substrates. Published reactivity values for the OH molecule on a heated substrate show a clear temperature dependence,[6] suggesting that substrate temperature (T_s) may affect the reactivity of SiH molecules. Therefore, we have examined the effects of T_s on surface reactivity of SiH as a further demonstration of our instrument's capabilities.

We have measured the surface reactivity of SiH at T_s = 300K, 373K, 473K, 573K, and 673K for three rotational states, J = 1.5, 3.5, and 5.5. Figure 4.4 shows one example of LIF signals using the J = 3.5 rotational state at T_s = 673 K. There was no discernable difference between this figure and the data collected as shown in Fig. 4.3. Thus, at

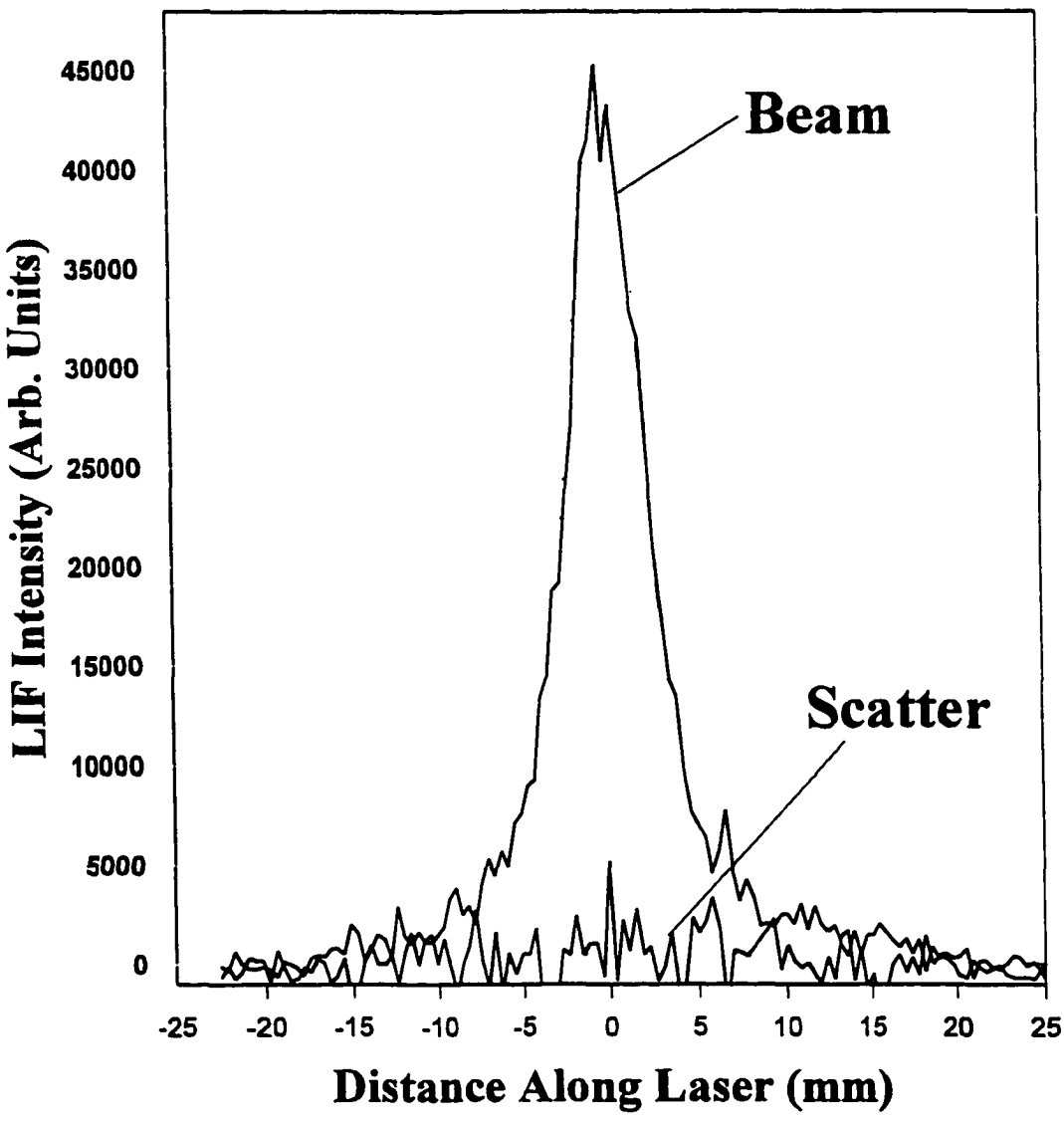

Fig. 4.4 LIF signals for SiH in the molecular beam (upper trace) and scattered from the substrate (lower trace) using elevated substrate temperatures (T_s = 673) and alternate rotational states (J = 3.5).

elevated substrate temperatures and with different rotational states, signals from scattered SiH is negligible. This is true for all substrate temperatures and all rotational states studied.

4.2.4. VELOCITY DISTRIBUTIONS OF SIH IN SILANE PLASMA

Figure 4.5 shows a one dimensional plot of LIF signal intensity for different gate delays for SiH in a 100% SiH_4 plasma (P = 5 W). As the gate delay time was increased, the position of the LIF intensity peak maxima clearly shifts, the peak width increases, and the intensity of the fluorescence decreases. At longer time delays, fluorescence intensities were below our detection limits (>3 μs) for collection times < 600 s. The wings seen on these cross-sections were the result of a combination of scattered light and a slightly unfocused laser beam.

Figure 4.5 also shows the simulated LIF intensity profiles generated by the velocity distribution model. The model accurately described the data for delays ranging from 0.20 μs to 2.2 μs. The average velocity was calculated using a weighted average of all $\tau \geq 0.7$ μs and yields Θ_T = 977 ± 45 K for the 55 W SiH_4 plasma. Table 4.1 shows the calculated average velocities for other rf plasma powers ranging from 5 W to 55 W. The good agreement between the simulated curves and the data in Figure 4.5 indicates the SiH velocities were well described by a Maxwell-Boltzmann distribution.

Figure 4.6 plots Θ_T of SiH as a function of applied rf plasma power. Like NH_2 and OH,[8] Θ_T in the molecular beam increases with increasing applied rf power. Unlike NH_2, however, a linear relationship between Θ_T and applied rf power was not seen. Instead,

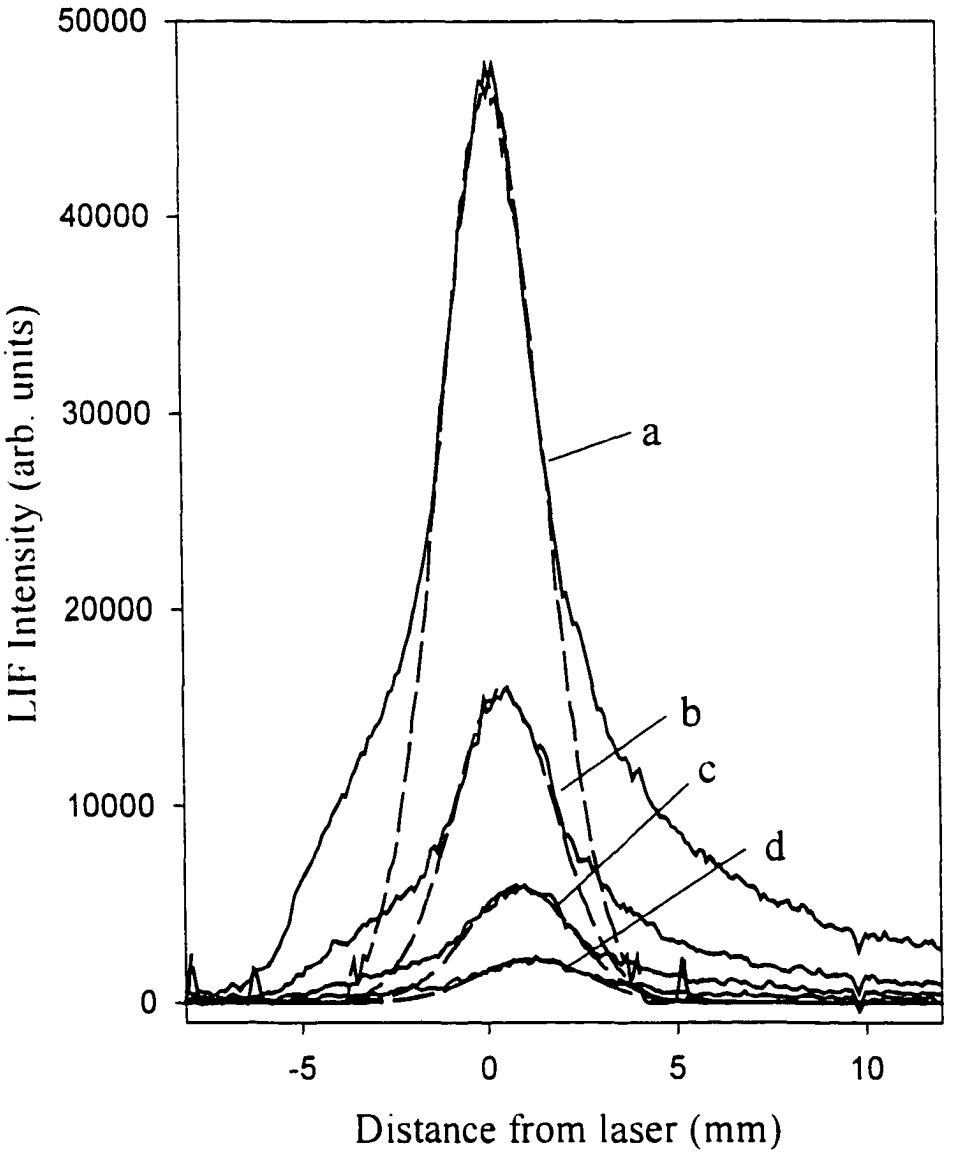

Figure 4.5 Cross sectional data for SiH radicals in a molecular beam formed from a 5 W SiH_4 plasma (solid line) at four different gate delays: (a) 1.25 μs delay (t = 0.20 μs), (b) 1.8 μs delay (t = 0.70 μs), (c) 2.3 μs delay (t = 1.2 μs), and (d) 2.8 μs delay (t = 1.7 μs). Simulated curves using the model described in the text are also shown (dashed lines). The curves correspond to (a) Θ_T = 650 K, (b) Θ_T = 565 K, (c) Θ_T = 675 K (d) Θ_T = 640 K.

Table 4.1

Θ_T for SiH radicals [a]

rf power (W)	τ (μs)			Avg. Θ_T (K) [b]	Avg. v(ms^{-1}) [c]
	0.7	1.2	1.7		
5	500	518	515	627 ± 56	911 ± 81
14	530	515	520	638 ± 45	919 ± 65
25	625	600	600	723 ± 47	978±64
40	590	600	610	957±45 K	1125±52
55	710	690	655	977±45 K	1137±52

[a] Calculated from the model described in Appendix 1.
[b] The mean Θ_T for the τ listed. Errors reported are one standard deviation from mean.
[c] Average velocity of SiH.

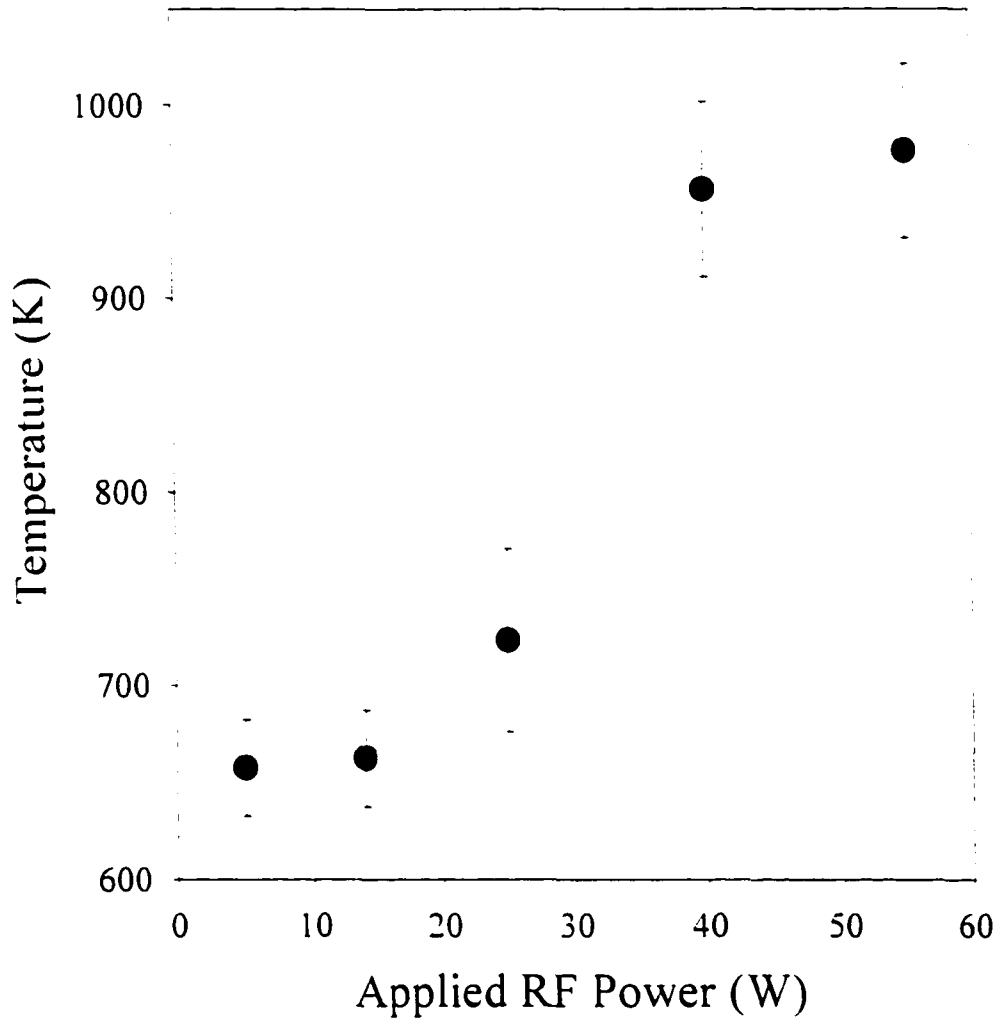

Figure 4.6 Θ_T as a function of applied rf plasma power for a 10.0 sccm SiH_4 plasma. Each point is the average Θ_T from τ = 0.7, 1.2 and 1.7 μs. Error bars represent one standard deviation of the mean.

Θ_T increased gradually with increasing applied rf power from 5 W to 25 W. From 25 W to 40 W, a large increase is measured for Θ_T, and then from 40 W to 55 W only a slight increase is seen in Θ_T. Also, no increase in pressure inside the plasma reactor was noted with increasing applied rf power as was observed in the NH_2 experiments. This non-linear relationship between Θ_T and the applied rf power indicate changes were occurring in the plasma over the applied rf power range studied. Possible changes in the plasma mode will be addressed in greater detail in section 4.3.

4.3. DISCUSSION

The multitude of gas-surface interactions that occur during plasma processing is difficult to characterize precisely. During PECVD, the growing film surface is continuously bombarded with reactive neutral molecules, ions, and high-energy photons, yielding a complex steady-state surface composition. The resulting film chemistry, morphology, electronic and structural properties for any system are directly affected by the interactions of these reactive species with the substrate. Indeed, radicals are believed to be the most important species in many plasma etching and deposition systems.[9] Thus, it is desirable to know how the individual plasma species interact at the surface of the material being processed. The IRIS technique allows the study of one specific molecule interacting at a surface while the surface is being processed by the full range of plasma species.

Our IRIS apparatus has been used to study the rotational-state-resolved reaction of SiH with the surface of a-Si:H during plasma deposition. With SiH, we measured a

surface reactivity of 0.95 ± 0.05 on a room temperature substrate, in good agreement with previous IRIS measurements.[1] Furthermore, the reactivity did not change measurably with substrate temperature from 300 K to 673 K. This high reactivity of SiH radicals on the surface of a depositing a-Si:H film suggests that SiH may be an important species in the deposition process. Note, however, that these experiments simply measure the disappearance of SiH molecules from the gas phase, but do not distinguish between loss mechanisms on the surface. That is, there is no distinction between SiH molecules that are incorporated into the depositing film and SiH molecules that undergo a surface reaction to form another species that desorbs from the surface [e.g. SiH(ads) + H(ads) → SiH_2 (g)] Also, since these experiments did not measure the relative abundance of the various species responsible for deposition in the plasma it is impossible to decipher the relevant importance of the SiH radical as compared to other plasma species. It is possible, however, that SiH formed under different conditions and plasma exposure may exhibit a different reactivity than that observed here.

There is extensive debate in the literature over the importance of various precursors in PECVD of a-Si:H from SiH_4 plasmas. As IRIS data can aid in understanding the roles of various precursors to deposition processes, a brief discussion of this debate is warranted here. Much of the discussion has centered on the role of the various radicals present in these systems, specifically SiH_x (x = 1-3). Most researchers agree that SiH_3 is the most important precursor under typical deposition conditions. This is based primarily on experimental evidence that SiH_3 is the dominant mono-silicon radical in SiH_4 plasmas.[10,11] In addition, several studies on the gas phase reactions of SiH_x radicals

show that SiH and SiH_2 react rapidly with SiH_4 (the dominant species in typical rf SiH_4 plasmas[12]), while SiH_3 does not.[13,14,15,16] SiH_3 does, however, react very rapidly with other radicals.[12] This leads to a long lifetime for SiH_3 radicals in a silane plasma. Doughty and Gallagher have shown that SiH_x species are produced primarily in the center of an rf discharge, away from the substrate.[17] For these radicals to contribute to film growth they must travel some distance to reach the substrate. Thus, a long lifetime is crucial for them to have a significant role in film growth. This suggests that even if SiH and SiH_2 have significant concentrations in the center of the plasma, they will not reach the film surface in ample numbers to be important in film deposition.[17]

In addition to the number densities of the various possible film precursors, we must also consider their surface reactivities. Here, we have shown the surface reactivity of SiH is near unity at the surface of a depositing a-Si:H film using T_s = 300-673 K. IRIS measurements are the only direct measurement of a surface loss coefficient, β, for SiH_x radicals currently available. Other literature studies have estimated β for SiH_2 and SiH_3 radicals. Values for SiH_3 range from 0.050 on a hydrogenated, chlorinated silicon surface,[18] to 0.2 on a-Si:H.[19] In addition, Perrin and Broekhuizen estimate that $\geq$60% of adsorbed SiH_3 recombine with other radicals at the surface and desorb.[19] Some researchers believe, however, that a low surface loss coefficient leads to greater surface mobility for film precursors which ultimately leads to a better quality material.[20] The only β value available for SiH_2 comes from Robertson and Rossi who measured $\beta(SiH_2) = 0.15$ on an a-Si:H film.[21] Hence, although the number density of SiH radicals in SiH_4 plasmas may be significantly less than that of SiH_3, the considerable difference in β values of these

molecules implies that SiH could be an important precursor, depending on the plasma parameters.

Another factor that must be considered in determining the relative importance of SiH_x radicals to film growth is the specific plasma conditions used to deposit a-Si:H. Several studies show that increasing plasma power decreases the number density of SiH_4 while increasing the number density of other plasma species.[22,23,24] In addition, Perrin and co-workers have determined there are two deposition regimes in SiH_4 plasmas, the α regime and the γ regime.[25] The γ regime can be accessed by either high pressures or high electrode bias voltages and is characterized by an increased electron density.[26] In this regime, there is an increase in the relative number density of SiH_x radicals in the plasma.[24,25] In our IRIS experiments, we observe a higher number density of SiH molecules when the plasma source is operating at pressures above 20 mTorr. We also observe much higher number densities of SiH radicals at higher rf powers. This would imply that in the γ regime, SiH radicals could be important contributors to film growth.

The velocity measurements of SiH in the molecular beam indicate a complex relationship exists between the applied rf power and Θ_T. Below 25 W and above 40 W, Θ_T increases gradually with applied rf power, but from 25 W to 40 W a large increase in Θ_T is observed. It is likely a change in plasma modes occurs between 25 W and 40 W and is responsible for this effect. This change in mode is likely related to a change from an α to γ plasma mode.

As mentioned in Chapter 1, electrodeless coil plasmas can be either capacitively coupled or inductively coupled. In the capacitively coupled regime not only is it possible

for coupling to occur between the plasma and the individual loops in the rf coil, but also between the coil and any grounded objects significantly close to the coil. A likely explanation for the increase in Θ_T is that, at low powers capacitive coupling occurs only between the plasma and the individual coils of the plasma, but at higher powers coupling begins to occur between the coil and the metal interface between the glass reactor and the differential region. The rise in Θ_T between 25 and 40 W occurs concomitant with an increase in brightness at the orifice to the differential region. We attribute this increase in brightness at the orifice to the onset of coupling between the coil and the differential wall. Coupling between the coil and the differential region would increase the total amount of translational energy along the axis of the coil, thus explaining the sudden increase in Θ_T.

The IRIS data presented here for the SiH molecule is not meant to provide the final word in the debate over the most important precursors for a-Si:H deposition. Rather, we hope to provide further insight into the mechanisms for a-Si:H deposition by performing IRIS experiments on other radicals present in SiH_4-based systems. By developing a more complete picture of the interactions of radicals with surfaces during deposition of a-Si:H films, we can draw better conclusions about the role of silicon hydride species in film growth.

REFERENCES

1. P. Ho, W. G. Breiland, and R. J. Buss, J. Chem. Phys. **91**, 2627 (1989).

2. L. Klynning and B. Lindgren, Ark. Fys. **33**, 73 (1966).

3. A. E. Douglas, Can. J. Phys. **35**, 71 (1957).

4. C. V. Jackson, Proc. R. Soc. A **126**, 373 (1930).

5. J. Perrin and E. Delafosse, J. Phys. D: Appl. Phys. **13**, 759 (1980).

6. E. R. Fisher, P. Ho, W. G. Breiland, and R. J. Buss, J. Phys. Chem. **97**, 10287 (1993).

7. G. Bruno, P. Capezzuto and G. Cicala in *Plasma Deposition of Amorphous Silicon-Based Materials*, edited by G. Bruno, P. Capezzuto, and A. Madan (Academic Press, Boston, 1995), p. 27.

8. K. H. A. Bogart, J. P. Cushing, and E. R. Fisher, J. Phys. Chem. B **101**, 10023 (1997).

9. R. d'Agostino in *Plasma Deposition, Treatment and Etching of Polymers*, edited by Riccardo d'Agostino (Academic Press, San Diego, 1990), p. 528.

10. R. Robertson and A. Gallagher, J. Appl. Phys. **59**, 3402 (1986).

11. N. Itabashi, N. Nishiwaki, M. Magane, T. Goto, A. Matsuda, C. Yamada, and E. Hirota, Jap. J. Appl. Phys. **29**, 585 (1990).

12. J. M. Jasinski and S. M. Gates, Acc. Chem. Res. **24**, 9 (1991).

13. J. P. M. Schmitt, P. Gressier, M. Krishnan, G. De Rosny, and J. Perrin, Chem. Phys. **84**, 281 (1984).

14. M. H. Begemann, R. W. Dreyfus, and J. M. Jasinski, Chem. Phys. Lett. **155**, 351 (1989).

15. G. Inoue and M. Suzuki, Chem. Phys. Lett **122**, 361 (1985).

16. J. M. Jasinski and J. O. Chu, J. Chem. Phys. **88**, 1678 (1988).

17. D. A. Doughty and A. Gallagher, J. Appl. Phys. **67**, 145 (1990).

18. J. M. Jasinski, J. Phys. Chem. **97**, 7385 (1993).

19 J. Perrin and T. Broekhuizen, Appl. Phys. Lett. **50**, 433 (1987).

20. M. Kawasaki and Y. Kawaguchi, Appl. Phys. Lett. **62**, 3099 (1993).

21. R. Robertson and M. Rossi, J. Chem. Phys. **91**, 5037 (1989).

22. K. Tachibana, Mater. Sci. and Eng. **B17**, 68 (1993).

23. F. Kampas and R. Griffith, J. Appl. Phys. **52**, 1285 (1981).

24. C. Bohm and J. Perrin, J. Phys. D: Appl. Phys. **24**, 865 (1991).

25. J. Perrin, P. Cabarrocas, B. Allain, and J. Friedt, Jap. J. Appl. Phys. **27**, 2041 (1988).

26. V. A. Godyak and A. S. Khanneh, IEEE Trans. Plasma Sci. **PS-14**, 112 (1986).

CHAPTER 5

SURFACE INTERACTIONS OF THE NH_2 RADICAL IN NH_3 PLASMAS

5.1. INTRODUCTION

Ammonia plasmas are widely employed in industrial processes as a means of modifying surfaces for increased adhesion between polymer layers in composite materials;[1,2] for creating ultra thin nitride passivation layers on semiconducting devices, such as polycrystalline silicon[3] and GaAs;[4] and extensively (with mixtures of silane) to deposit amorphous, hydrogenated silicon nitride (a-SiN_x:H) as a passivation layer on integrated circuits.[5,6] Silicon nitride films produced from NH_3/SiH_4 plasmas are known to have low pinhole densities with good stoichiometry. In the past ten years, basic studies of NH_3 adsorption on Si(111)[7,8] and Si(100)[9] have been performed in an effort to understand mechanisms for creating thin nitrides through CVD or PECVD processes.

In many ammonia-based plasma systems, the NH_2 radical is considered an important intermediate.[10,11] It has been observed in these systems using OES,[10,12,13] and in the photosensitized decomposition of SiH_4 and NH_3 mixtures using LIF.[14] In NH_3/SiH_4 plasmas, NH_2 radicals are thought to react with SiH_x (x = 1-3) radicals to form tetra- and tri-aminosilane complexes [$Si(NH_2)_4$ and $Si(NH_2)_3$], which in turn react at a substrate surface to form a-SiN_x:H.[10,15] Films grown from these NH_3/SiH_4 plasmas had no measurable Si-H bonding and exhibited superior dielectric properties.[11] Direct

measurement of the surface interactions of gas-phase species, including aminosilane, SiH_x, and NH_2 radicals, during plasma treatment with ammonia-based plasmas have not, however, been investigated.

Our IRIS technique directly measures the reactivity of gas-phase species at a substrate during plasma processing. IRIS combines molecular beam and plasma technologies with LIF to provide spatially-resolved 2D images of plasma species. To date, the IRIS method has been used to investigate five different radical species in several plasma systems. The surface reactivity of these species vary from near unity (SiH),[16,17] to intermediate (OH),[18,19] to low (SiO and NH),[20,21] to surface production of the species (CF_2).[22,23] Here, the interactions of NH_2 with a variety of surfaces, specifically Si, SiO_2, Si_3N_4, polyimide, polytetrafluoroethylene (PTFE), and Pt, using 100% NH_3 and SiH_4/NH_3 plasma molecular beams were investigated. With the exception of polyimide, NH_2 is generated at the surface of these substrates during processing with a 100% NH_3 plasma. With the SiH_4/NH_3 plasma, an intermediate reactivity is observed for NH_2 during deposition of an a-SiN_x:H film on Si substrates.

In Chapter 3, the translational temperature for NH_2 molecules in the 100% NH_3 plasma molecular beam (Θ_{Tmb}) as a function of applied rf power by exploiting the time delay on our detector were reported. A linear relationship was observed between Θ_{Tmb} and the applied power, P, from 5 to 150 W. Here the translational temperature for the NH_2 radicals scattering from substrates (Θ_{Tsc}) were measured. For NH_2 scattered from a Si substrate, Θ_{Tsc} was significantly lower than Θ_{Tmb}, but was notably higher than the

substrate temperature (T_s). Possible explanations for these observations are discussed along with mechanisms for surface production of NH_2.

5.2. RESULTS

5.2.1. SPECTROSCOPY

Spectroscopic studies of the NH_2 radical date to the early work of Dressler and Ramsey who reported NH_2 as the first Renner–Teller molecule in 1959.[24] In its ground electronic state, NH_2 is bent and is a highly asymmetric top; in its excited state, however, the molecule vibrates about a linear configuration.[24] Another unique characteristic of the NH_2 radical is its relatively long radiative lifetime of ~10 μs.[25] Figure 5.1 shows an experimental fluorescence excitation spectrum for NH_2 formed in a 20 sccm NH_3 plasma (P = 45 W) for a portion of the $^2B_1\tilde{X}$ - A^2A_1 electronic transition. Most of the scattering and velocity data presented here were collected using the most intense line at 597.725 nm which contains three overlapping rotational transitions (3_{03}–3_{13}; 4_{04}–4_{14}; and 5_{05}–5_{15}). Other states used to collect additional scattering data were the 1_{01}-1_{11}, the 7_{07}-7_{17}, and the 3_{03}-2_{11} rotational transitions in the same vibrational band found at 597.642, 597.218 and 596.255 nm, respectively.

5.2.2. FORMATION OF NH_2 RADICALS

NH_2 LIF intensity was measured as a function of applied rf power, Fig. 5.2a. Because we are saturating the transitions, these intensities correspond to the relative species densities. Formation of NH_2 in an NH_3 plasma increases rapidly with rf power, and reaches a maximum at ~100 W, decreasing rapidly at higher powers. Figure 5.2b

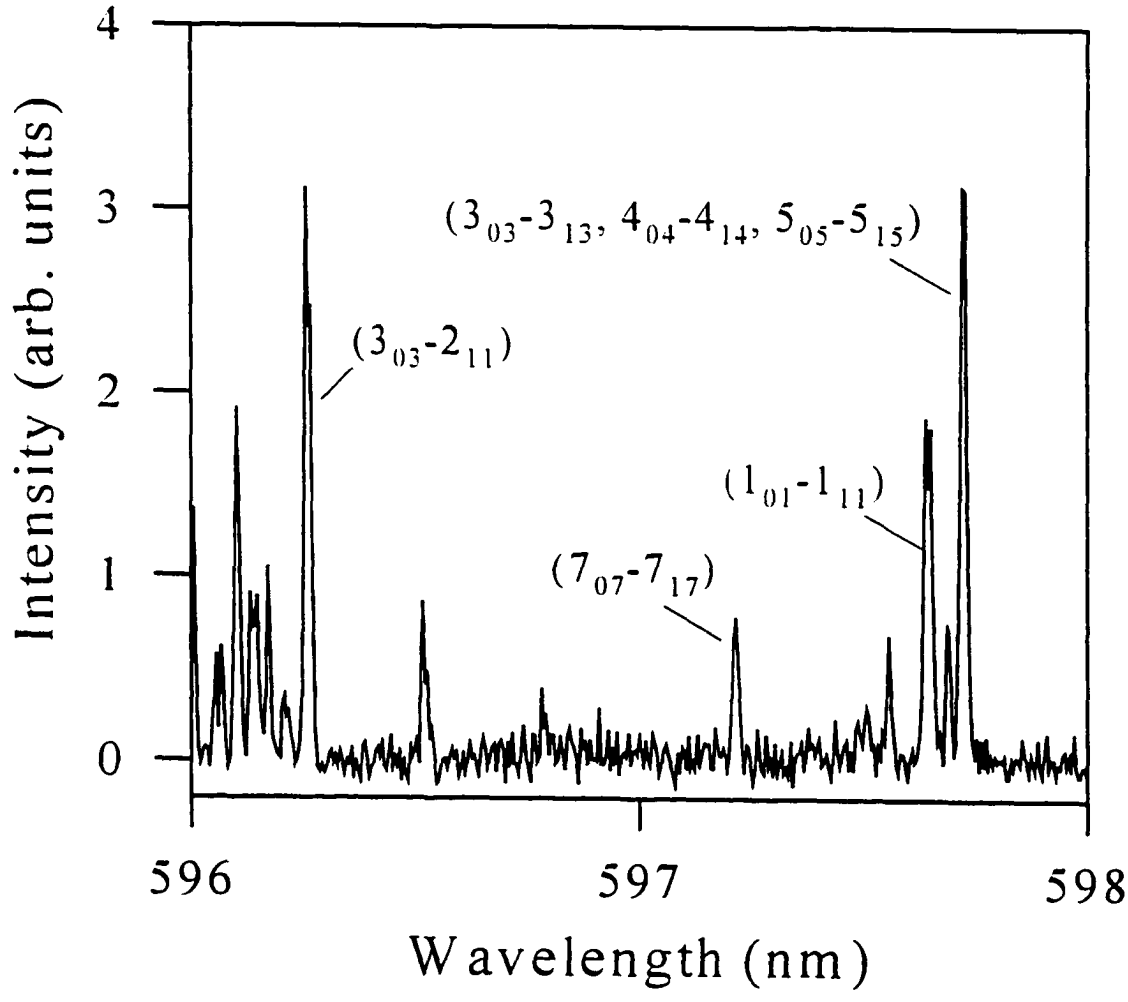

Figure 5.1. Experimental fluorescence excitation spectrum of NH_2 in the molecular beam formed from a 100% NH_3 plasma (P = 45 W, 20 sccm). The spectrum was taken with 0.005 nm steps on the dye laser.

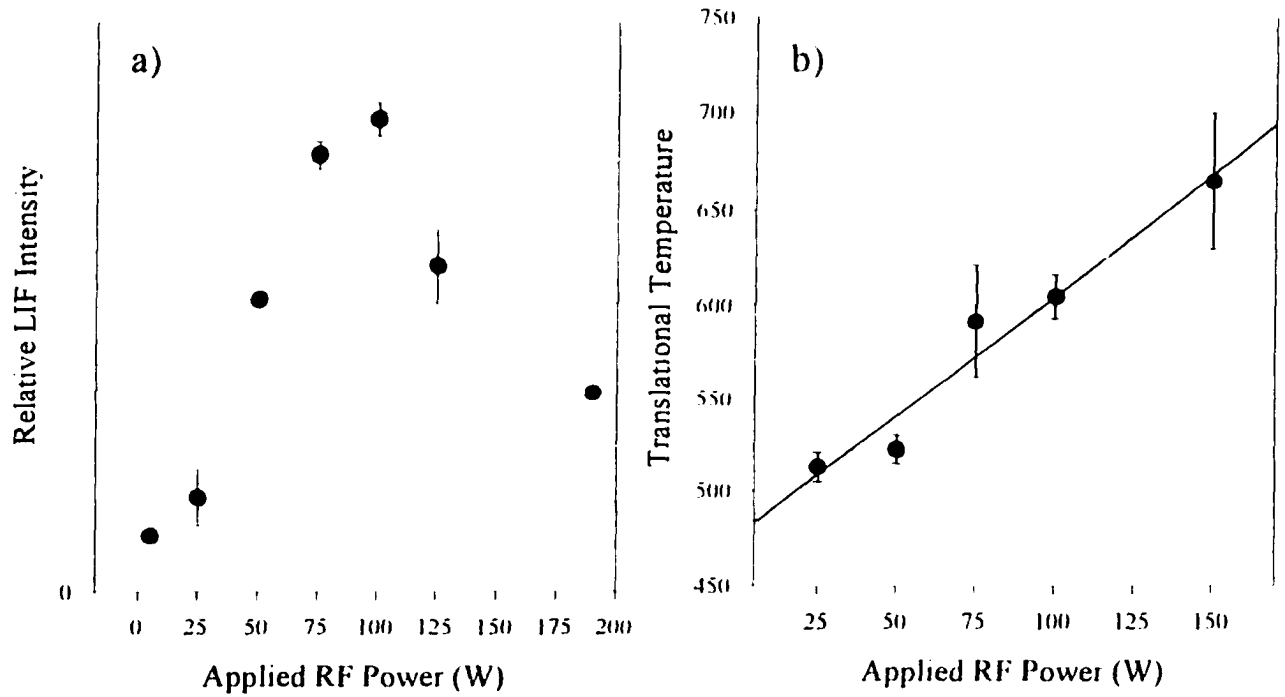

Figure 5.2. (a) Relative intensities of NH_2 radicals in the 100% NH_3 molecular beam as a function of applied power. (b) The relationship of Θ_{Tmb} and P for NH_2 radicals in the NH_3 molecular beam. The line represents a least-squares linear regression analysis of the data with an r^2 value of 0.977.

shows Θ_{Tmb} for NH_2 as a function of rf power,[26] which clearly shows there is a linear relationship between P and Θ_{Tmb}. This is interesting, as increased fragmentation of gas phase species is known to be one of the most important ways to dissipate power in rf plasmas.[27] Moreover, the decrease in NH_2 density with increasing rf power, Fig. 5.2a, suggests some fragmentation of the NH_2 radicals occurs at higher power.

5.2.3. SPATIAL DEPENDENCE

Figure 5.3 shows the two-dimensional ICCD images of the LIF of NH_2 using a pure NH_3 plasma molecular beam (P = 45 W). LIF from NH_2 radicals in the incident molecular beam is shown in Fig. 5.3a. In Fig. 5.3b, a room temperature (300 K) Si(100) substrate with native oxide removed has been rotated into the path of the molecular beam and the LIF signal includes both NH_2 radicals in the molecular beam and those scattering from the surface. Figure 5.3c is the difference between Figs. 5.3b and 5.3a, showing the signal of NH_2 radicals scattered from the surface. The broad spatial distribution and the shift of the scattered signal peak maximum away from the incident molecular beam signal maximum indicates the NH_2 radicals scatter with a cosine distribution.

Figure 5.4 shows the one-dimensional cross sections corresponding to Figs. 5.3a and 5.3c along with the simulated curves for the incident beam and for scattered molecules assuming an adsorption-desorption mechanism with S = 1.4. Scaling this result by F_D yielded S = 1.23. Averaging all data sets taken over a period of 9 months yielded a recommended scattering value of S = 1.23 ± 0.06 on the Si substrates. A scattering value greater than unity indicates that surface production of NH_2(g) contributes to the observed

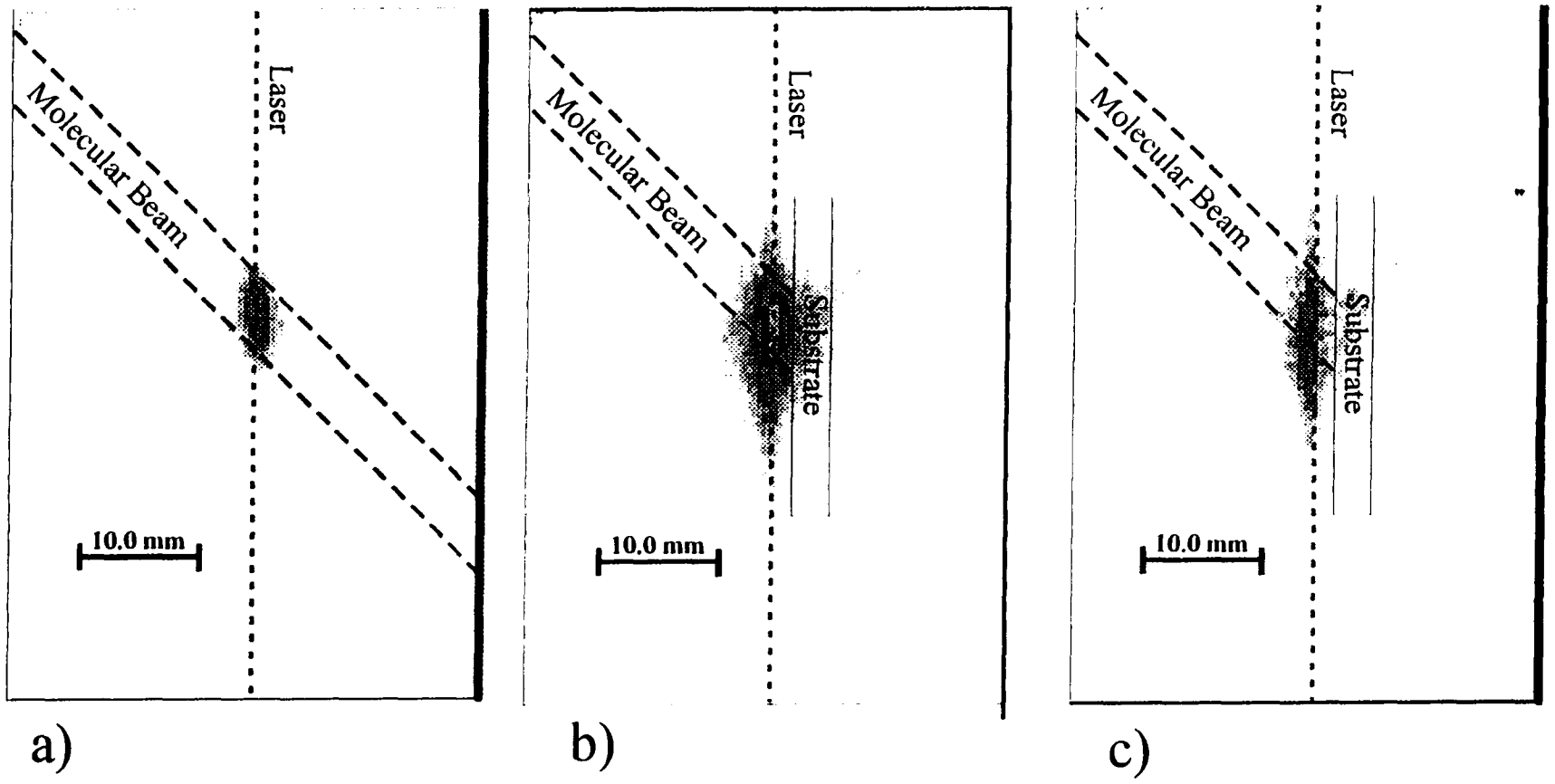

Figure 5.3. Spatially-resolved two-dimensional ICCD images of LIF signals produced by NH_2 molecules (a) in the 100% NH_3 molecular beam only (no substrate) and (b) with a 300 K Si substrate in the path of the molecular beam at a distance of 2.0 mm from the laser. The image shown in (c) is the difference between the images shown in (a) and (b), corresponding to NH_2 molecules scattering from the substrate. The lines indicate the path of the molecular beam and the laser in the images. LIF signals with the highest intensity appear as the darkest regions in the image.

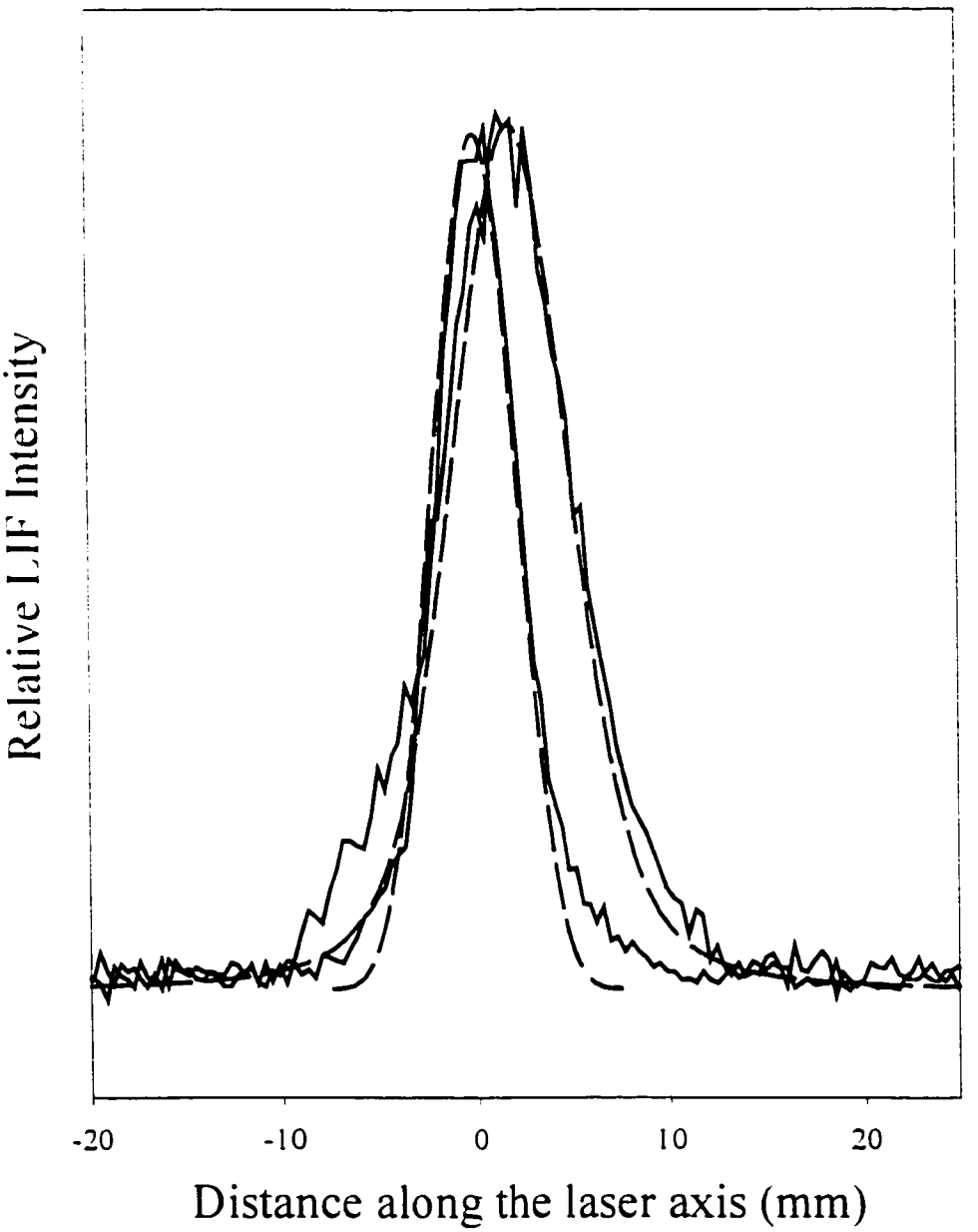

Figure 5.4. Cross-sectional data converted from the images shown in Fig. 5.2 for the LIF of NH_2 in the incident molecular beam and scattered from the Si substrate. The dashed lines are simulated curves from the reactivity simulation described in the text with $S = 1.4$. With the F_D correction factor $S = 1.23$.

scattering signal. Surface generation of a radical has only been observed previously in IRIS experiments with CF_2 radicals using various fluorocarbon precursors.[22,23]

In separate experiments, the native oxide was not removed from the Si substrate prior to use in IRIS experiments. These SiO_2 substrates [i.e. Si (100) with native oxide] were processed in the IRIS apparatus and $S = 1.05 \pm 0.06$ was measured , somewhat lower than that found for the etched substrates. $S = 1.23 \pm 0.06$, Table 5.1. The difference in scatter may be the result of a change in surface interactions or an increase in surface roughness with the etched surface, leading to greater scatter. Although analysis of scanning electron microscopy (SEM) images showed no difference in surface roughness for both etched and unetched Si wafers, the possibility of an increase in surface roughness at the nm scale could not be eliminated.

To further explore the surface generation phenomenon, IRIS measurements for NH_2 were performed using a variety of substrates. Table 5.1 shows S values for NH_2 from a 45 W NH_3 plasma on silicon-based, polymeric, and metallic substrates. On all substrates, NH_2 showed a high degree of scatter, especially with Si_3N_4 substrates. After removal from the IRIS apparatus, substrates were examined using transmission FTIR. None of the substrates showed any appreciable film deposition. On each of the silicon-based substrates, however, there was an area apparent to the eye that has been modified by the molecular beam [i.e. it is the size and shape of the molecular beam].

In addition to FTIR analysis, substrates were also analyzed using SEM. Charging was observed with the processed substrates, suggesting the surface was modified with a non-conductive layer. In contrast, no charging was observed with the unprocessed surface, or

Table 5.1. NH_2 Scatter

Substr.	Rotational Transition	T_r (K)	Appl. Power (W)	Scatter w/o correction factor	Velocity ratio factor‡	Scatter with correction	Special Conditions
Si	3-3,4-4,5-5	300	45	1.40±0.04	0.87±0.05	1.23±0.11	
Si	3-3,4-4,5-5	300	45	0.95±0.07	0.76±0.06	0.72±0.13	grounded mesh
Si	3-3,4-4,5-5	300	150	2.10 ±0.07	0.77±0.06	1.63±0.19	
Si	3-3,4-4,5-5	300	150	1.00±0.05	0.67±0.07	0.67±0.14	grounded mesh
Si	7-7	300	45	1.23±0.11	0.87±0.05	1.07±14	
Si	3-2	300	45	1.50±0.11	0.87±0.05	1.31±14	
Si	3-3,4-4,5-5	373	45	1.30	0.91±0.05	1.18±7	
Si	7-7	373	45	1.40±0.07	0.91±0.05	1.27±12	
Si	3-2	373	45	1.25±0.07	0.91±0.05	1.14±12	
Si	3-3,4-4,5-5	423	45	1.05±0.07	1.00±0.05	1.05±0.12	
Si	7-7	423	45	1.15±0.07	1.00±0.05	1.15±0.12	
Si	3-2	423	45	0.95±0.07	1.00±0.05	0.95±0.12	
Si	1-1	300	45	0.95±0.07	0.76±0.06	0.72±0.13	grounded mesh
Si	1-1	300	150	2.30±0.10	0.77±0.06	1.78±0.21	
Si	1-1	300	150	0.95±0.10	0.67±0.07	0.64±0.17	grounded mesh
Si	1-1	723	45	0.69±0.07	1.24±0.07	0.85±0.16	
Si	3-3,4-4,5-5	723	45	0.76±0.05	1.24±0.07	0.94±0.12	
Si	3-2	723	45	0.69±0.07	1.24±0.07	0.85±0.16	
Si	3-3,4-4,5-5	300	45	1.40±0.10	0.87±0.05	1.23±0.14	NH_3/H_2 (20:20)
Si	3-3,4-4,5-5	300	45	1.00±0.05	0.87±0.05	0.87±0.10	SiH_4/NH_3 (3:20)
SiN	†	300	45	1.85±0.05	0.87±0.05	1.62±0.13	
SiO_2	†	300	45	1.20±0.04	0.87±0.05	1.05±0.10	
Pt	†	300	45	1.40±0.09	0.87±0.05	1.23±0.14	
Teflon	†	300	45	1.53±0.07	0.76±0.06	1.16±0.16	
Polyimide	†	300	45	1.06±0.04	0.76±0.06	0.80±0.11	

†Three rotational lines (1_{01}-1_{11}), (3_{03}-3_{13}, 4_{04}-4_{14}, 5_{05}-5_{15}), and (3_{03}-2_{11}) were used for determining the scattering ratio.

‡No velocity data was collected for Si_3N_4, SiO_2, or Pt, therefore the velocity ratio factor for Si was used for these data sets.

after rubbing the processed substrate with a cotton tip swab. Polymer substrates showed no visible surface modifications as a result of processing with the IRIS apparatus. Goniometry measurements of plasma processed polymer surfaces, however, showed significant decreases occurred in the static water contact angle.[28] For polyimide, the contact angle changed from 72 ± 2° to 28 ± 1° after a 10 minute treatment with a 40 W NH_3 plasma. Likewise, the same treatment with a PTFE substrate showed a significant decrease in contact angle, from 105 ± 2° to 53 ± 2°. This suggests that a significant change in surface polarity occurs with plasma treatment using an NH_3 plasma. Similar changes have been observed previously in ammonia plasma treatment of polymer substrates.[29]

Si_3N_4 substrates showed one of the largest scattering of NH_2, Table 5.1. As with the processed Si substrate, there was a visible streak on the Si_3N_4 wafers, corresponding to the molecular beam. SEM images revealed no change in the surface morphology of the Si_3N_4 wafer after processing; however, the crystalline surface did show a high degree of surface roughness. This roughness, and corresponding large surface area, may contribute to the significantly higher surface production of NH_2 from Si_3N_4 substrates.

5.2.4. ADDITION OF SILANE AND HYDROGEN

As noted in section 5.1, NH_2 is believed to be an important precursor in the gas-phase formation of aminosilane complexes [$Si(NH_2)_3$ and $Si(NH_2)_4$] in silane/ammonia plasmas.[10] These large gas-phase species can then react on a substrate and contribute to the formation of a-SiN_x:H films in SiH_4/NH_3 plasmas. If this is true, we would expect that

addition of silane to our 100% NH_3 plasma would decrease the gas-phase density of NH_2. Figure 5.5 shows the relative LIF intensity of NH_2 with a constant NH_3 flow and an increasing SiH_4 flow. As is clear from these data, the NH_2 signal is strongly dependent on the amount of SiH_4 in the feed and no NH_2 LIF signal was detected above a 1:4 ratio of SiH_4/NH_3. NH_2 scattering experiments were performed in the IRIS apparatus using a NH_3/SiH_4 plasma and a Si substrate. Results showed $S = 0.87 \pm 0.10$ ($\bar{R} = 0.13 \pm 0.10$) for NH_2, a significant decrease from the results given in Table 5.1 for a 100% NH_3 plasma.

Hydrogen gas is often added to plasmas as a reactive diluent. As it is possible that H atoms play a role in the surface production of NH_2 in our experiments, H_2 was added to our NH_3 plasma to investigate this possibility. With 20.0 sccm of H_2 added to the feed (i.e. 1:1 NH_3:H_2), the operating pressure in the plasma source tube rose only slightly to ~80 mtorr. The relative signal intensity of NH_2 in the molecular beam, however, decreases by a factor of four from that observed with 100% NH_3. With H_2 added, there was no detectable change in the NH_2 scatter, Table 5.1.

5.2.5. ROTATIONAL TEMPERATURE DETERMINATION

Two methods were applied to estimate the rotational temperature of NH_2 radicals in the molecular beam, Θ_{Rmb}. In the first method, excitation spectra of NH_2 in the molecular beam and NH_2 scattering from a surface were collected simultaneously. Figure 5.6 shows the LIF excitation spectra for NH_2 in the molecular beam ($P = 45$ W) and for NH_2 scattering from a 300 K Si substrate. From these spectra, it is clear that little variance is seen in the ratio of peak heights for NH_2 in the molecular beam to NH_2

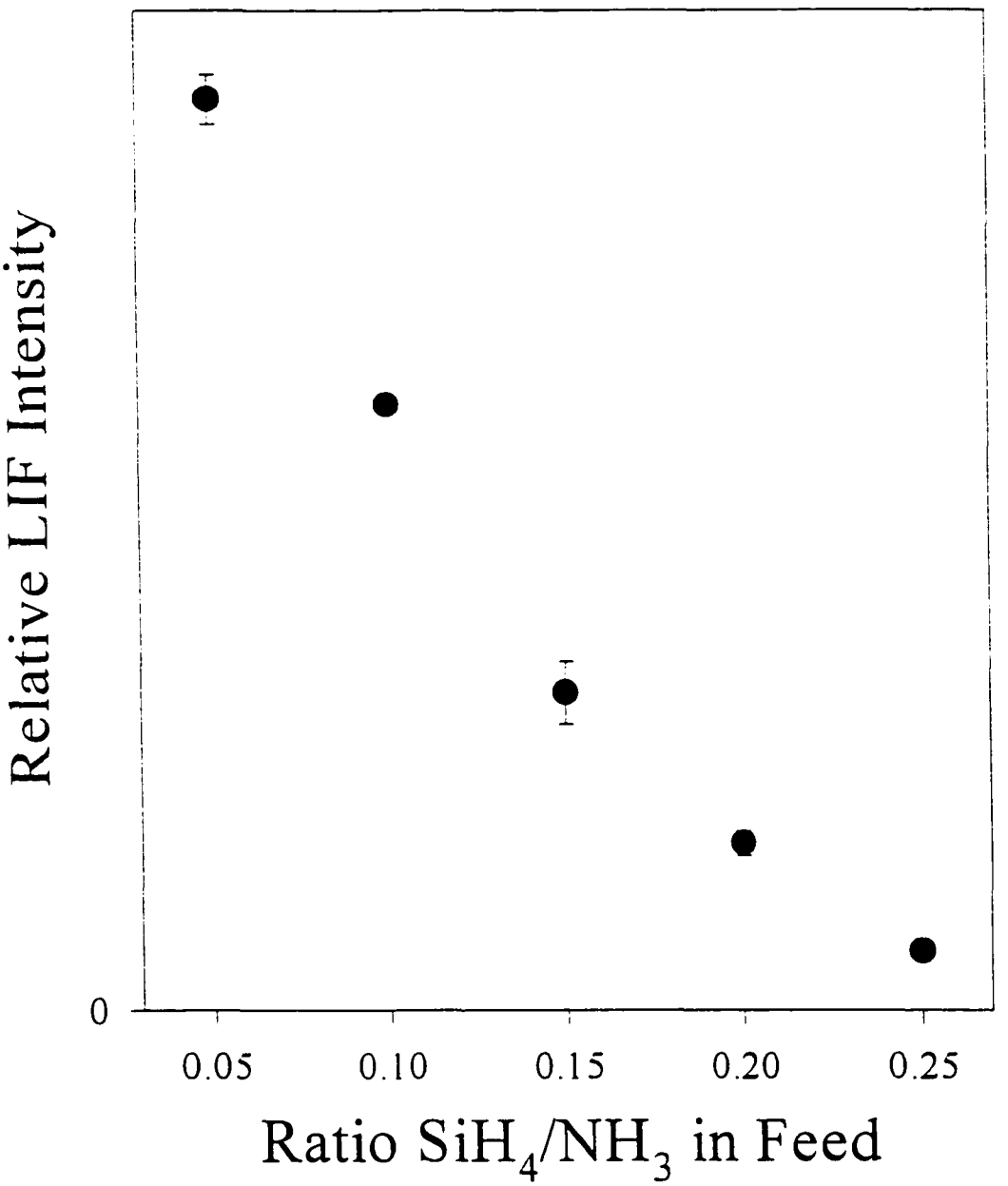

Figure 5.5. Relative intensity of the NH_2 LIF signal as a function of the SiH_4/NH_3 ratio in the feed. NH_3 flow was hel constant at 20.0 sccm. Pressure was 67 ± 3 mtorr in the plasma source.

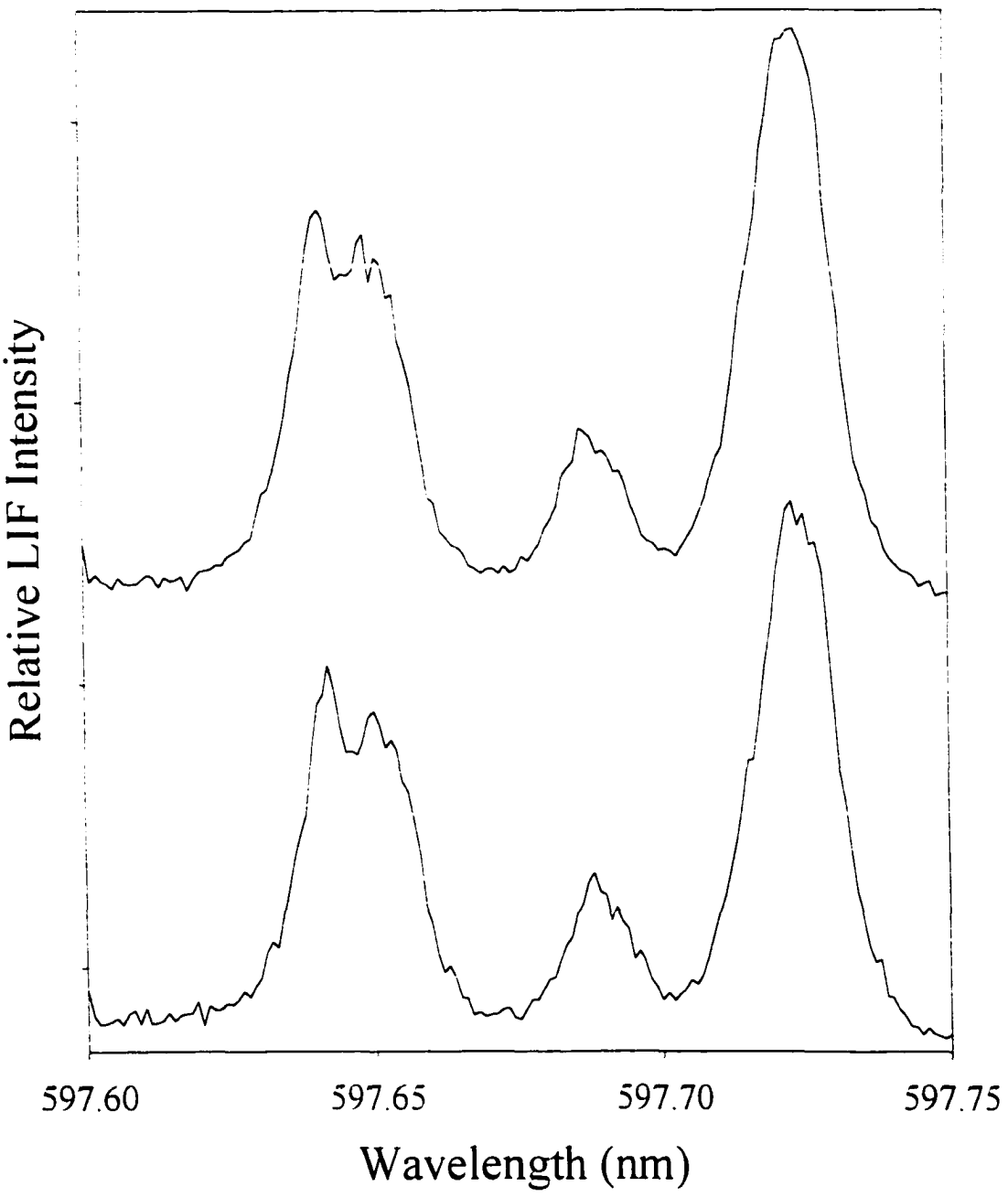

Figure 5.6. Excitation spectra for NH_2 desorbing from a 300 K Si substrate (upper spectrum) and in the molecular beam (lower spectrum). The spectra were taken simultaneously using a time delay of 0.9 μs and a gate width of 15 μs to achieve separation of the two signals.

scattering from the surface. This suggests that the populations in these states were roughly equivalent before and after collision with the substrate. Assuming the molecules equilibrated thermally on the substrate surface before desorbing, the data suggests $\Theta_{Rmb} \approx 300$ K.

The second method used involves analysis of the rotational state dependence of the radical's surface scattering ratio as a function of T_s. If the $\Theta_{Rmb} = T_S$, the population of a specific rotational state in the incident beam is the same as that for the molecules coming from the surface (assuming complete energy accommodation with the surface). The rotational temperature of the molecules then no longer affects the measurement, and all rotational states will exhibit the same value for S. By examining the S values for different rotational states as a function of T_S, Θ_{Rmb} can be determined.

Figure 5.7 displays the scattering ratio for three prominent rotational lines found in the NH_2 spectra, the 3_{03}-2_{11} transition at 596.255 nm, the overlapping (3_{03}-3_{13}, 4_{04}-4_{14} and 5_{05}-5_{15}) transitions at 597.725 nm, and the 7_{07}-7_{17} transition at 597.210 nm, as a function of T_s. At $T_s = 300$ K, modeling the data yields corrected weighted averages of $S = 1.31 \pm 0.12$, $S = 1.23 \pm 0.06$, and $S = 1.07 \pm 0.12$ for the three lines, respectively. Modeling the data at $T_S = 373$ K yields different S values for the three rotational lines, with $S = 1.14 \pm 0.09$, 1.18 ± 0.07, and 1.27 ± 0.09, respectively. The highest rotational state showed an increase in S, while the other two rotational states showed lower values for S when compared to the room temperature data. This was likely because the population of the highest rotational state for desorbed NH_2 increased at the higher substrate temperatures, while those of the lower rotational states decreased.[19,21] Above 373 K, all rotational levels

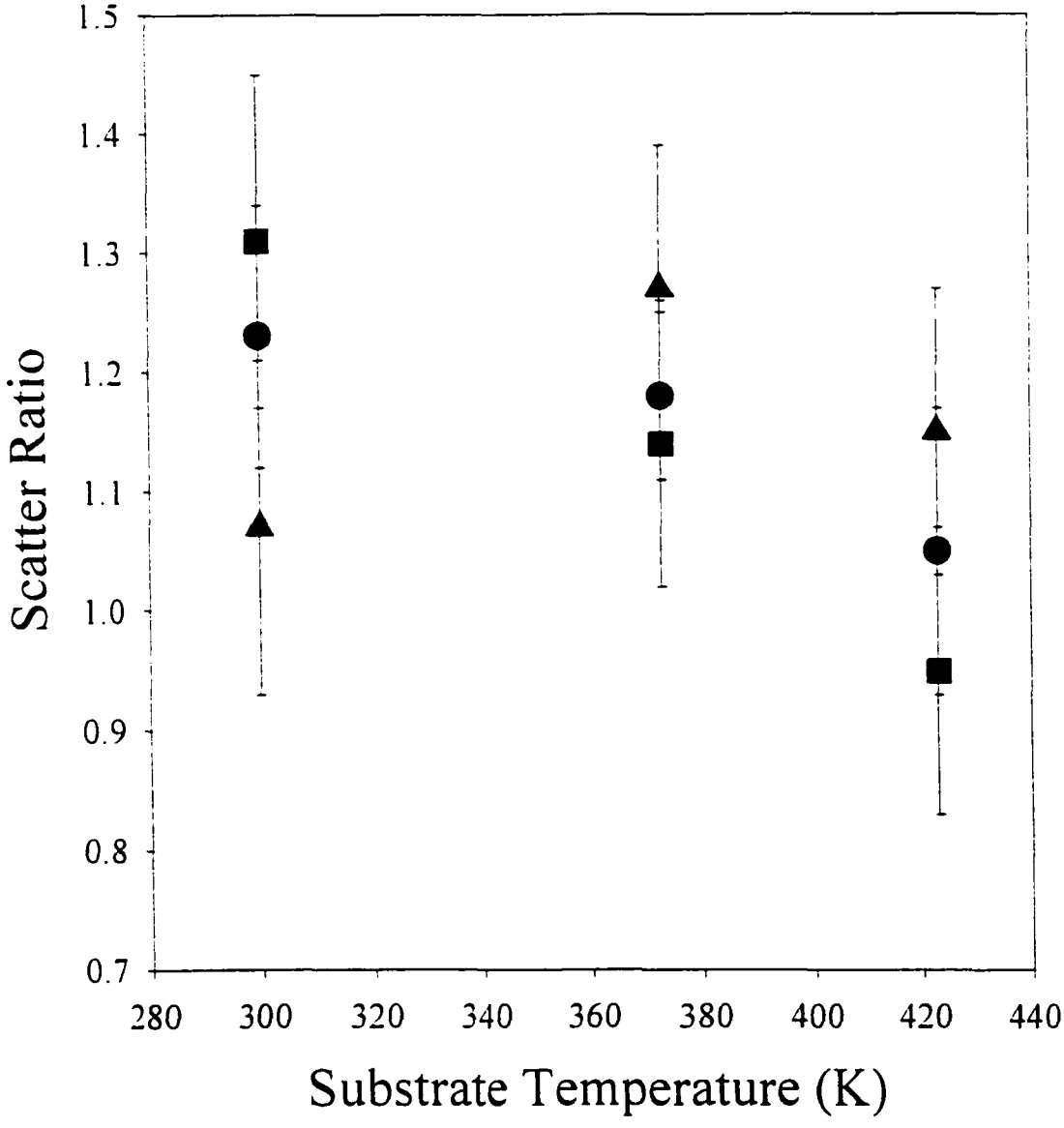

Figure 5.7. Substrate temperature dependence of scattering ratio for the ■ (3_{03}-2_{11}), ●(3_{03}-3_{13}, 4_{04}-4_{14}, 5_{05}, 5_{15}), and ▲(7_{07}-7_{17}) rotational lines of the (0,9,0) vibrational band of NH_2. The scattering ratio is the maximum peak height of the scatter signal divided by the peak height of the signal from the molecular beam. The values used are the corrected values given in Table 5.1.

showed a decrease in scattering ratio. Assuming NH_2 equilibrates energetically on the substrate, analysis of all data points in Fig. 5.7 yield $\Theta_{Rmb} \sim 340$ K.

5.2.6. ION EFFECTS

A possible source of surface generated NH_2 is chemical sputtering of adsorbed species as a result of ion bombardment. Indeed, other work in our laboratories has shown that ion bombardment contributes significantly to the surface production of CF_2 radicals in a variety of fluorocarbon systems.[22,23] We tested this in the present system by placing a grounded mesh screen on the collimating slit. As the molecular beam passes through this slit, a molecular beam consisting of radicals and parent gas, with little or no charged species is produced. IRIS measurements made with the grounded mesh screen in the molecular beam revealed a substantial reduction in the amount of NH_2 scattering from a Si substrate, Table 5.1. Additional evidence for the influence of ion bombardment comes from measurements made at P = 150 W. Under these conditions, $S = 1.63 \pm 0.19$ without the mesh, significantly higher than that at P = 45 W. With the mesh, however, S decreases significantly to 0.67 ± 0.14, Fig. 5.8.

5.2.7. VELOCITY DISTRIBUTIONS FOR SCATTERED NH_2 RADICALS

Figure 5.9 shows images of NH_2 LIF with a 300 K Si substrate in the path of the molecular beam using τ = 0.95, 2.95, and 4.95 μs. At the shortest τ, there appeared to be only one distribution of signal intensity located along the path of the laser beam. As τ was

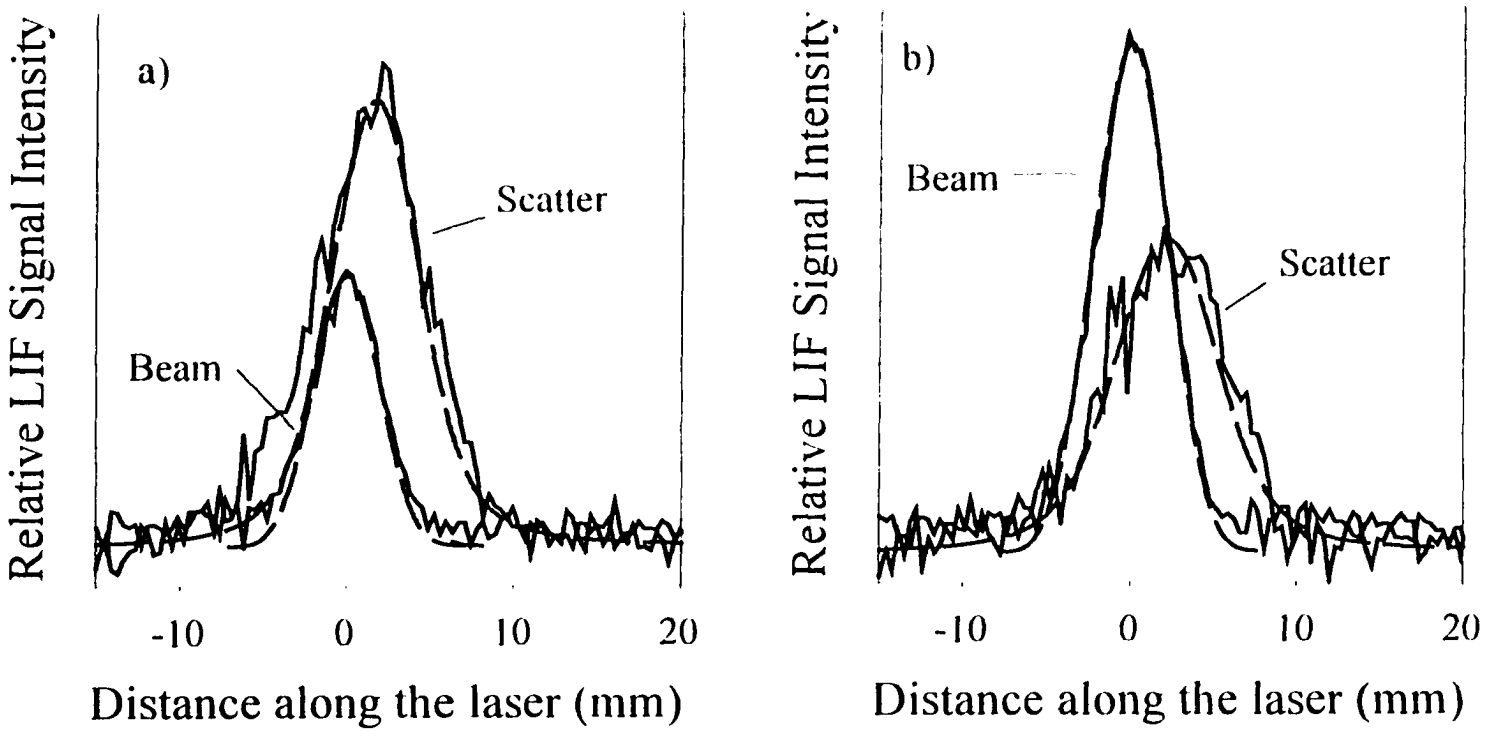

Figure 5.8. Cross-sectional data for the LIF of NH_2 scattered from a Si substrate using a 100% NH_3 plasma molecular beam with 150 W plasma a) with no mesh, and b) with a grounded mesh placed in the path of the molecular beam. Dashed lines are the simulations to the data with the values given in Table 5.1.

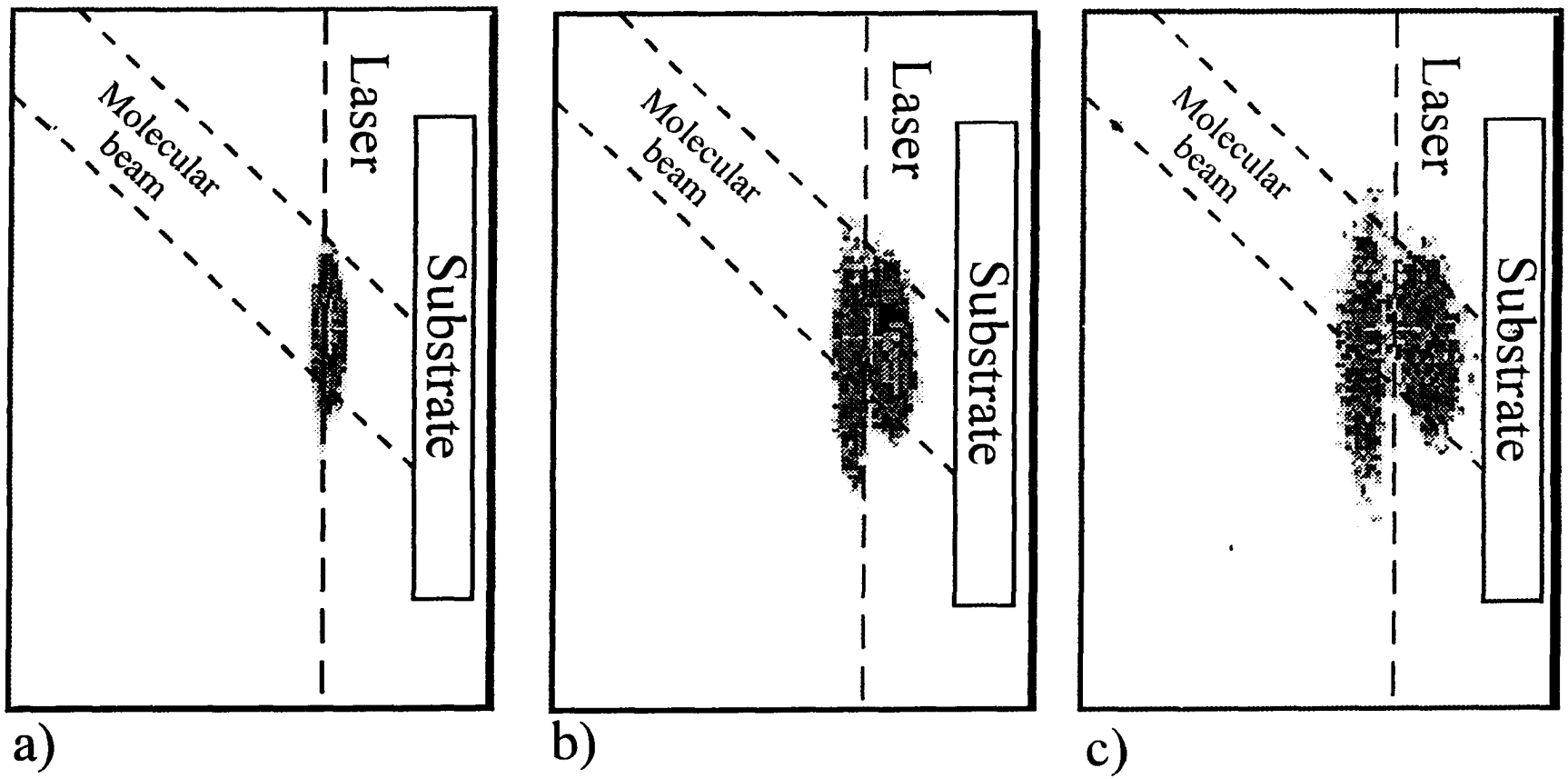

Figure 5.9. ICCD images of LIF signals produced by NH_2 molecules at (a) $\tau = 0.95$ μs, (b) $\tau = 2.95$ μs, and (c) $\tau = 4.95$ μs with a Si(100) substrate in the path of the molecular beam, 9 mm from the laser. The dashed lines indicate the location of the molecular beam and the laser beam in the images.

increased, however, two different regions of intensity appear in the image, corresponding to NH_2 radicals in the incident molecular beam traveling towards the substrate and NH_2 radicals scattering off of the substrate. At the longest τ, the two spots are almost completely separated as a result of the different velocity distributions of the incident and scattered species. By examining the time dependence of these images, Θ_{Tsc} for NH_2 radicals were determined.

To simulate the data for scattered molecules, the initial distribution of NH_2 radicals after excitation was fit with a Gaussian distribution to represent the laser cross-section. This distribution was then allowed to evolve in time with a Maxwell-Boltzmann distribution of velocities and a cosine distribution of densities along the laser axis. As the density of NH_2 radicals measured was related to the velocity distribution, we were able to derive Θ_T, by using a Maxwell-Boltzmann distribution,[30] equation. 2.2.

Figure 5.10 shows a cross section of the signal along the laser beam and demonstrates that the scattered NH_2 signal is well-described by a cosine distribution. Figure 5.11 shows cross sectional data along the molecular beam for molecules scattered from a 300 K Si substrate with τ = 0.75, 4.75, 6.75, and 8.75 μs along with the simulated velocity distributions with Θ_{Tsc} = 400 K, which reproduce the data well. This simulation suggests that the desorbed NH_2 molecules were translationally hotter than the Si substrate, but colder than NH_2 in the molecular beam. For Si substrates, $\Theta_{Tsc} = 400 \pm 30$ K for NH_2 formed in both 45 and 150 W plasmas. In contrast, velocity measurements made with the polymer substrates of polyimide and PTFE yielded $\Theta_{Tsc} = T_S = 300 \pm 30$ K, Table 5.2.

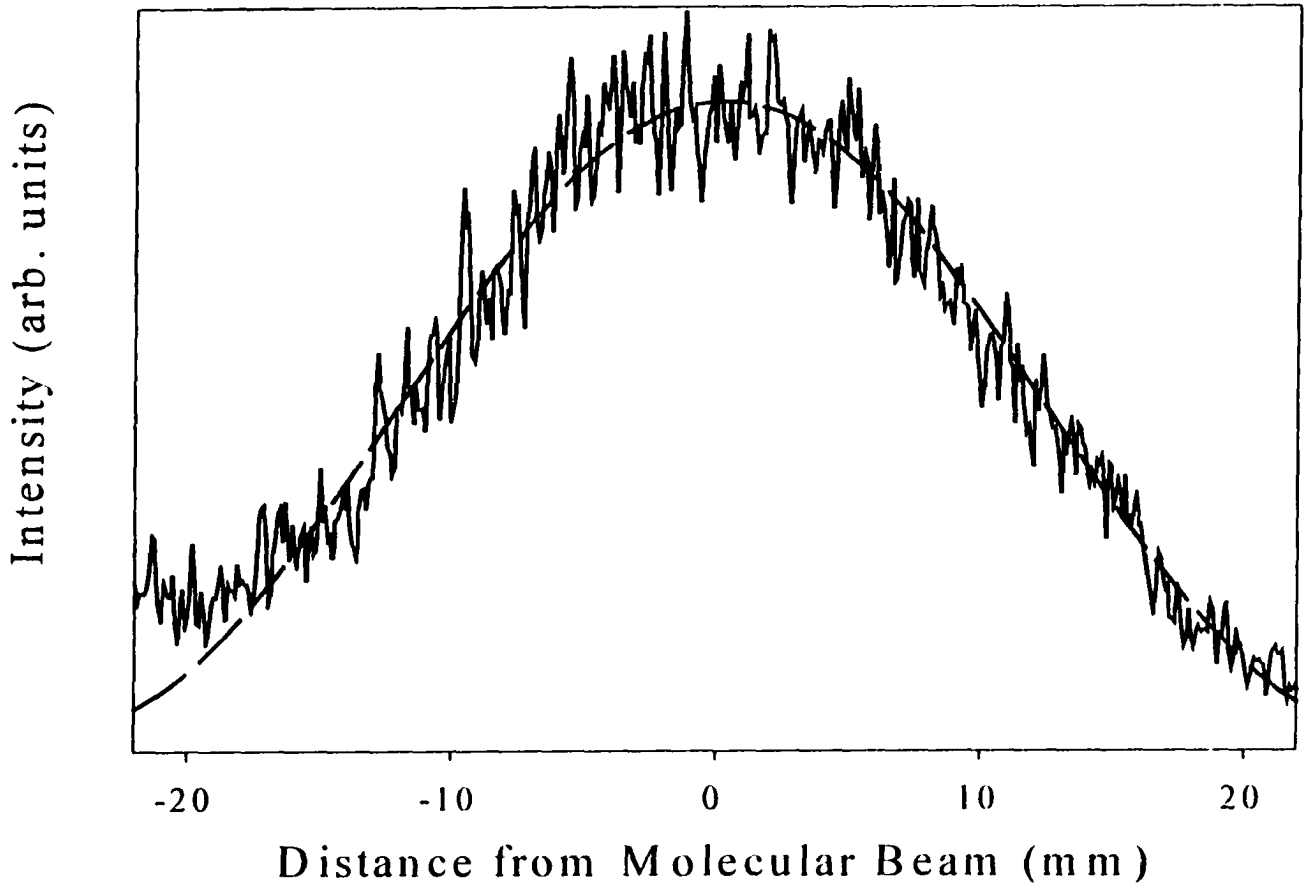

Figure 5.10. Spatial distribution of NH_2 scatter as cross sectional data *along* the laser (solid line) This is an average of 100 columns of pixels over the most intense portion of the LIF signal The simulated curve for a cosine distribution is shown as a dashed line.

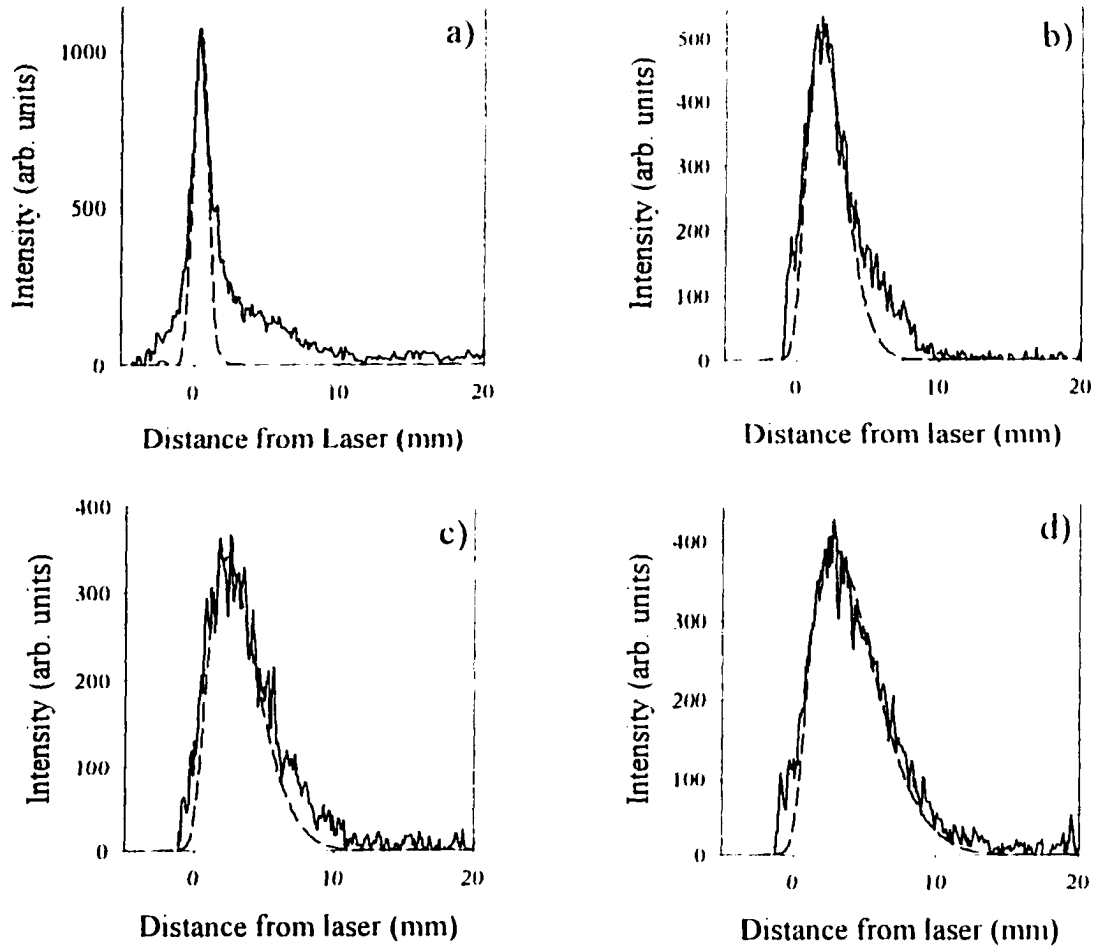

Figure 5.11. Cross sectional data for NH_2 radicals scattered from a Si substrate taken *across* the laser beam. These data were collected with (a) τ = 0.75, (b) τ = 4.75, (c) τ = 6.75 and (d) τ = 8.75 μs, a laser-surface distance of 2.0 mm, and T_S = 300 K. The dashed lines are a simulation using the model described in the text with Θ_{tsc} = 400 K.

Table 5.2.

Θ_T for NH_2 radical scattering from a surface.[a]

Substrate	T_s (K)	Avg. $\Theta_{T\,scat}$ (K)[b]	Avg. v (ms^{-1})[b,c]	Ion removal
Si	300	400±30	726±27	
Si	723	800±100	1028±64	
Si	300	300±29	630±30	X
Polyimide	300	300±29	630±30	
Teflon	300	300±29	630±30	

[a] Calculated from the model described in the text.

[b]Errors are weighted averages of all measurements, best fits were determined using a least squares calculation of data versus simulation.

[c]Average velocity of NH_2.

To determine if charged particles influence the value of Θ_{Tsc}, velocity distributions were collected with the grounded mesh screen in the path of the molecular beam. In this configuration, Θ_{Tsc} = 300 ± 30 K for NH_2 scattering from a room temperature (300 K) Si substrate. This was significantly lower than what was observed when ions were present, Table 5.2. To rule out the possibility that Θ_{Tmb} was affected by the presence of the mesh, additional velocity measurements were made for NH_2 radicals in the molecular beam. For NH_2 radicals in a high power plasma molecular beam (P = 150 W), Θ_{Tmb} = 664 ± 34 K. This was within experimental error of that measured without the grounded mesh, Θ_{tmb} = 650 ± 50 K, clearly demonstrating that the mesh does not affect the energy distribution in the molecular beam.

5.3. DISCUSSION

Characterization of plasma species and their interactions with a surface is critical to understanding the chemical mechanisms of plasma processing. With the complex mixture of reactive species present in a plasma, deconvoluting individual interactions at the interface is difficult. When mixtures of gases are used, such as in the SiH_4/NH_3 system, additional fragmentation and recombination pathways exist and understanding the contribution of species formed in these reactions adds an additional layer of complexity to the plasma chemistry. The IRIS techniques used here allow identification of a specific plasma species and measurement of internal and translational energies as well as surface reactivities of the radical of interest. Here, the implications of our work on the surface

interactions of NH_2 radicals and on the energetics of NH_2 radicals both in the plasma and scattered from the substrate are discussed.

5.3.1. SURFACE PRODUCTION OF NH_2.

One of the major observations of these experiments is that more NH_2 is leaving the surface relative to the flux of NH_2 reaching the surface from the plasma. This high degree of scatter indicates that NH_2 must be generated at the surface during processing with the NH_3 plasma molecular beam. We have observed this behavior previously in IRIS experiments with only one other species, CF_2 radicals in CHF_3 and C_2F_6 plasmas.[22,23]

Surface analysis of the substrates used in these IRIS experiments reveals that no film is deposited during exposure to a molecular beam generated from a pure NH_3 plasma.[31] We believe it plausible that at steady-state, the surface is predominantly terminated with NH_x groups, although unpaired electrons and physisorbed NH_3 molecules could also be present. Yates and coworkers have determined that under ultrahigh vacuum (UHV) conditions, at high NH_3 exposures, molecular NH_3 adsorbs as a second layer and multilayer species which do not dissociate.[32] Additional UHV studies have shown that NH_3 dissociatively adsorbs on Si(100)-(2x1) reconstructed surfaces[33,34,35] as well as on Pt and other transition metals at low surface coverage (i.e. <0.86 monolayer).[36,37] The NH_2(ads) species produced through this dissociative adsorption at T_S = 120 K are stable up to ~600 K. In our high vacuum system, the flux of NH_3 plasma species is ~3 monolayers when the substrate is in the path of the molecular beam. Thus, it is likely that our substrates are covered with multilayers of NH_3 when T_s = 300 K. As T_s is increased,

these multilayers, as well as any adsorbed $Si(NH_2)_x$ species decompose, creating a much more disordered surface.[7,8] At substrate temperatures above 600 K, NH_2(ads) decomposes into N(ads) and H(ads) and there is some recombination to form NH_3(g).[32] Above T_S = 700 K, nitride formation is occurring along with N(ads) diffusing into the bulk material, becoming part of the Si(100) lattice.[32] Thus, loss of adsorbed nitrogen on the surface via diffusion into the Si lattice may contribute to the observed decrease in scatter for NH_2 on Si substrates with T_s > 700 K.

There are several possible reactions that could account for the observed production of NH_2 radicals. First, dissociative adsorption of NH_3 molecules on the substrate would result in formation of NH_2(a) and H(a). Yates and coworkers have shown that NH_3 adsorbs onto Si(100) surface dimers, dissociating into NH_2(a) and H(a) with unit probability up to 0.85 monolayer coverage at T_S = 120 K.[32] The bond formed between the NH_2(a) and the Si dimer, however, is covalent with a calculated bond energy of 42 kcal/mol.[38] Thus, it is unlikely that NH_2(a) would spontaneously desorb from the surface at room temperature.

A second possibility is that another species in the molecular beam may abstract an adsorbed species such as a H atom to form gas-phase NH_2, as in reaction 5.1,

$$NH(g) + H(a) \rightarrow NH_2(g) + * \qquad (5.1)$$

where * represents an adsorption site on the exposed surface. If reaction 1 were contributing to formation of NH_2, we would expect to see a loss of NH radicals on the surface in an IRIS experiment. A previous IRIS study of NH radicals formed under similar conditions (P = 40 W) showed, however, that NH desorbs with 100% probability

from both Si and Si_3N_4 substrates.[21] This suggests that NH is not making a significant contribution to the surface production of NH_2.

Another probable source of NH_2 is either physical or chemical sputtering of the adsorbed NH_x (x = 1-3) layer that likely exists on the surface during our experiments. High energy ions from the plasma could impart large amounts of energy to adsorbed NH_3 molecules, causing them to fragment and desorb from the surface as NH_2 (g) and H (g). Moreover, ion bombardment would likely be able to break the covalent Si-N bond formed when NH_3 dissociatively adsorbs on the surface. This type of mechanism for surface production of NH_2 could also account for the high translational temperatures (i.e. $\Theta_{Tsc} > T_S$) measured for desorbing NH_2 radicals. This is discussed further below.

Results using increased applied rf power with and without a grounded mesh screen, Table 5.1, do suggest charged particles play an important role in the scattering mechanism for NH_2 from a Si substrate. Increasing the applied plasma power has several effects on plasma composition. For example, the number density of charged species (both electrons and ions) increases with rf power,[43] as can the ion energy.[39] Thus, if charged species are important in the surface production of NH_2, S should increase at higher P. As shown in Table 5.1, a significant increase in scatter is measured for the 150 W plasmas compared to the 45 W plasmas. Also, if charged species are responsible for the increase in NH_2 scatter, selective removal of the charged particles from the plasma molecular beam should result in a decrease in S. As shown by the data in Fig. 5.8 and in Table 5.1, this is indeed what is observed for both high and low power plasmas.

Although there is no evidence in the literature to support the idea of ion-enhanced

dissociation of NH_3(a) or ion-enhanced desorption of NH_2(a) there is direct evidence for electron-induced dissociation of NH_3(a) on Pt(111),[36,40] and on Cu(110).[41] Stechel and coworkers showed H atoms desorb from the surface of Pt dosed with NH_3 and subsequently irradiated with electrons.[40] Two types of NH_3(a) were observed, a strongly bonded α state (~1 eV), and a weakly bonded β state (~0.4 eV). The α state occurs at low NH_3 coverages (≤0.25 monolayer), while at higher coverages, β state adsorbates are present. There was no evidence, however, for the desorption of NH_2(a) in this study or in others.[42]

The increase in S after removing the SiO_2 layer on the Si (100) substrates indicates a change in the interaction of plasma species with the surface. Etching the native oxide from a Si substrate with an HF solution causes significant changes in the surface. Not only is the native oxide etched away, but surface "dangling bonds" are capped by hydrogen, helping to passivate the surface with respect to air oxidation. Moreover, the etched surface has a much higher static water contact angle (~10°) than the native oxide surface (~70°). This suggests that the etched substrate is much more hydrophilic than the unetched substrate, which could also be a factor in the observed scattering coefficients.

Surface production of NH_2 was observed for all substrates with the exception of polyimide where a net surface loss was observed, (S = 0.80 or R = 0.20). While the reason for this change is unclear, it is likely due to the polymeric nature of this substrate. In addition, the static water contact angle we measured for polyimide was 72 ± 2°, very similar to that observed for the SiO_2 substrate, and substantially lower than that observed for PTFE (106 ± 2°). Other factors such as the porosity of the films could also contribute

to the significant decrease in S and the subsequent increase in R. The correlation between S and contact angle for both polymeric and Si-based substrates suggests the hydrophilicity of the substrate material may be important to the scattering mechanisms for NH_2.

5.3.2. ROTATIONAL AND TRANSLATIONAL ENERGIES FOR NH_2.

To fully understand the chemistry of low-temperature plasmas, knowledge of the energy partitioning between species must be acquired. While kinetic energy distributions of plasma species are relatively difficult to determine,[43] the energetics of species that desorb from a substrate during plasma processing are even more difficult to determine directly in a plasma. The IRIS method allows one to obtain velocity distributions of radicals in the plasma molecular beam as well as for scattered species. In Fig. 2b, the relationship of Θ_{Tmb} and P for NH_2 radicals in the NH_3 molecular beam is shown. Under the conditions used here (P = 45 W) for our reactivity studies, Θ_{Tmb} = 520 ± 8 K, (see Chapter 3). In contrast, the scattered NH_2 radicals show a significantly higher value, Θ_{Tsc} = 400 ± 40 K, Fig. 5.11. If the NH_2 radicals were adsorbing on the substrate, equilbrating energetically, and desorbing,[19] one would expect that the desorbing radicals to have internal and translational temperatures characterized by T_S. Although Θ_{Tsc} is significantly higher than T_S, it is lower than Θ_{Tmb}. This suggests there may be partial energy accommodation on the surface. The source of the "extra" translational energy found for desorbing NH_2 molecules (i.e. $\Theta_{Tsc} > T_S$), however, is likely other beam species that are bombarding the substrate during the IRIS experiments.

The best explanation for these observations lies in the proposed mechanism for the

surface generation of NH_2 discussed in the previous section. We believe that a significant fraction of the NH_2 radicals desorbing from the substrate are formed through ion bombardment of adsorbed NH_x (x = 2 or 3) species. To determine if this is plausible on an energetic basis, the ion kinetic energy is needed. Calculating the ion kinetic energy lost at a surface, ε_i, is not straightforward, however, as it depends on the electron temperature, T_e, substrate bias, and sheath voltage, V_s.[43] For a non-biased substrate, however, V_s can be estimated by eq. 5.1,

$$V_S = \frac{T_e}{2}\ln(\frac{M}{2\pi m}) \qquad (5.1)$$

where M is the ion mass, and m is the mass of an electron.[43] ε_i is then given by the sum of the ion energy entering the sheath, $0.5T_e$, and V_S.[43] Assuming $T_e \sim 3$ eV and M = 0.01703 kg,[44] we estimate $\varepsilon_i \sim 14$ eV. This is clearly enough energy to break any surface bonds and to produce $NH_2(g)$ or other species. Thus, not only do charged species in the molecular beam contribute to the surface production of NH_2 radicals, they also contribute to the translational temperature of the desorbed NH_2.

5.4. SUMMARY

Surface loss coefficients for NH_2 radicals have been measured on room temperature Si, SiO_2, Si_3N_4, polyimide, PTFE and Pt during plasma processing with a 100% NH_3 plasma. All NH_2 surface interactions can be modeled with an adsorption-desorption mechanism. For all substrates except polyimide, $S > 1$. S values greater than

one indicate NH_2 is being produced through surface reactions. Rf plasma power dependence experiments demonstrate that the amount of NH_2 scatter increases with applied rf power. When charged particles are selectively removed from the plasma molecular beam, however, S decreases significantly. Moreover, with the grounded mesh screen in the plasma molecular beam, surface loss of NH_2 is observed (i.e. $S < 1$), suggesting that charged species in the molecular beam are contributing to the surface formation of NH_2. Velocity distribution measurements for NH_2 radicals scattering from 300 K Si substrates indicate $\Theta_{Tsc} > T_s$. Removal of charged species from the molecular beam yields $\Theta_{Tsc} = T_S$, again implicating charged species in the mechanism for surface production of NH_2.

5.5. REFERENCES

1. Badey, J. P.; Espuche, E.; Duc,T. M. *Polymer* **1996**, *37*, 1377.

2. Tatoulian, M.; Arefi-Khonsari, F.; Amouroux, J. *Int. J. Adhes Adhes.* **1995**, *15*, 177

3. Cheng, H.-C.; Wang, F.-S.; Huang, C.-Y. *IEEE Trans. Elec. Devices* **1997**, *44*, 64.

4. Jones, M. E.; Shealy, J. R.; Engstrom, J. R. *Appl. Phys. Lett.* **1995**, *67*, 542.

5. Lee, K. R.; Sundaram K. B.; Malocha, D. C. *J. Mater. Sci.* **1993**, *4*, 283.

6. Reif, R.; Kern, W. In *Thin Film Processes II*; Vossen J. L.; Kern W., Eds. Academic, San Diego, CA, 1991, p. 537.

7. Tanaka, S.; Onchi M.; Nishijima, M. *Surf. Sci. Lett.* **1987**, *191*, L756.

8. Isu T.; Fujiwara, K. *Solid State Commun* **1982**, *42*, 477

9. Kubler, L.; Hlil, E. K.; Bolmont K.; Gewinner, G. *Surf. Sci.* **1987**, *183*, 503.

10. Murley, D. T.; Gibson, R. A. G.; Dunnett, B.; Goodyear, A.; French, I. D. *J. Non-Cryst. Solids* **1995**, *187*, 324.

11. Smith, D. L.; Alimonda, A. S.; Chen, C.-C.; Ready S. E.; Wacker, B. *J. Electrochem. Soc.* **1990**, *137*, 614.

12. Hicks, S. E.; Gibson, R. A. G. *Plasma Chem. Plasma Process.* **1991**, *11*, 455.

13. Vervloet, M.; Merienne-Lafore, M. F. *J. Chem. Phys.* **1978**, *69*, 1257.

14. Fuyuki, T.; Allain B.; Perrin, J. *J. Appl. Phys.* **1990**, *68*, 3322.

15. Kushner, M. J. *J. Appl. Phys.* **1992**, *71*, 4173.

16. Ho, P.; Breiland, W. G.; Buss, R. J. *J. Chem. Phys.* **1989**, *91*, 2627.

17. McCurdy, P. R.; Bogart, K. H. A.; Dalleska, N. F.; Fisher, E. R. *Rev. Sci. Instrum.* **1997**, *68*, 1684.

18. Fisher, E. R.; Ho, P.; Breiland, W. G.; Buss, R. J. *J. Chem. Phys.* **1993**, *97*, 10287.

19. Bogart, K. H. A.; Cushing, J. P.; Fisher, E. R. *Chem. Phys. Lett.* **1997**, *267*, 377. Bogart, K. H. A.; Cushing, J. P.; Fisher, E. R. *J. Phys. Chem. B* **1997**, *101*, 10016.

20. Buss, R. J.; Ho, P.; Weber, M. E. *Plasma Chem. Plasma Process.* **1993**, *13*, 61.

21. Fisher, E. R.; Ho, P.; Breiland, W. G.; Buss, R. J. *J. Phys. Chem.* **1992**, *96*, 9855.

22. Mackie, N. M.; Venturo, V. A.; Fisher, E. R. *J. Phys. Chem. B* **1997**, *101*, 9425; Mackie, N. M.; Capps, N. E.; Fisher, E. R. *J. Am. Chem. Soc.*, manuscript in preparation.

23. Capps, N. E.; Mackie, N. M.; Fisher, E. R. *J. Appl. Phys.* **1998**, *84*, 4736.

24. Dressler, K.; Ramsey, D. A.; *Phil. Trans. A* **1959**, *251*, 553.

25. Halpern, J. B.; Hancock, G.; Lenzi, M.; Welge, K. H. *J. Chem. Phys.* **1975**, *63*, 4808.

26. Actual values for both the translational temperatures and velocity distributions are provided in reference 7.

27. Grill, A. *Cold Plasma in Materials Fabrication:* IEEE Press: Piscataway, NJ, 1994.

28. Static contact angles for water were measured using the sessile drop method with a contact angle goniometer (Ramé-Hart Model 100).

29. Liston, E. M.; Martinu, L.; Wertheimer, M. R. *J. Adhesion Sci. Technol.* **1993**, *7*, 1091, and references therein.

30. Serway, R. A. *Physics for Scientists and Engineers*, 2nd Ed.; Saunders: New York, 1986.

31. This is based on FTIR analysis of the substrates and on the previous IRIS studies of NH radicals, Reference 21.

32. Dresser, M. J.; Taylor, P. A.; Wallace, R. M.; Choyke W. J.; Yates, J. T., Jr., *Surf. Sci.* **1989**, *218*, 75.

33. Johnson, A. L.; Walczak, M. M.; Madey, T. E. *Langmuir* **1988**, *4*, 277.

34. Bozso, F.; Avouris, Ph. *Phys. Rev. B* **1988**, *38*, 3937.

35. Larsson, C. U. S.; Flodström, A. S. *Surf. Sci.* **1991**, *241*, 353.

36. Sun, Y.-M.; Sloan, D.; Ihm, H.; White, J. M. *J. Vac. Sci. Technol A* **1996**, *14*, 1516.

37. Zemlyanov, D. Y.; Smirnov, M. Y.; Gorodetskii V. V. *Surf. Sci.* **1997**, *391*, 37.

38. Fattal, E.; Radeke, M. R.; Reynolds G.; Carter, E. A. *J. Phys. Chem. B* **1997**, *101*, 8658

39. Grill, A. in *Cold Plasma in Materials Fabrication* (IEEE, Piscataway, NJ, 1994).

40. Stechel, E. B.; Burns, A. R.; Jennison, D. R. *Surf. Sci.* **1995**, *340*, 71.

41. Mocuta, D.; Ahner, J.; Yates, J. T., Jr. *Surf. Sci.* **1997**, *383*, 299.

42. Selwyn, G. S.; Fujimoto, G. T.; Lin, M. C. *J. Phys. Chem.* **1982**, *86*, 760.

43 Lieberman, M. A.; Lichtenberg, A. J. *Principles of Plasma Discharges and Material Processing*; Wiley and Sons: New York, 1994.

44. This corresponds to the mass of NH_3^+ ions in the plasma. If the most significant ionic species in the plasma is some other species, the value of ε_i decreases.

CHAPTER 6

EXPERIMENTAL METHODS FOR THE DEPOSITION AND ANALYSIS OF THIN FILMS

6.1 INTRODUCTION

Thin films of a-$Si_{1-x}C_x$:H were deposited from silane/methane plasmas produced in an inductively coupled rf reactor. This reactor configuration offers high flexibility, low cost, and low maintenance. Deposition parameters such as applied rf power (P), substrate bias, and the pulse duty cycle were varied to investigated the effects on the deposition process and film composition. In a typical deposition experiment, the vacuum chamber was evacuated to base pressure (~1-3 mTorr), silane (1.00 sccm) and methane (4.00 sccm) were then admitted into the plasma chamber and their steady state pressure allowed to stabilize. A plasma was ignited and the reflected power minimized. The deposition proceeded for a set time and the rf power was terminated. After pump-down to base pressure, the chamber was vented and substrates were removed for analysis by Fourier transform infrared spectroscopy (FTIR), X-ray photoelectron spectroscopy (XPS), scanning electron microscopy (SEM), and profilometery.

6.2 PLASMA REACTOR

All films were deposited in our home-built inductively coupled rf plasma reactor,

Figure 6.1.[1] The chamber was pumped by a direct-drive Alcatel 2012A (4.2 Ls^{-1}) mechanical pump. The chamber consists of two cylindrical Pyrex glass tubes (150 mm long) with a 50 mm o-ring joint, allowing easy access to the interior of the reactor. Glass sleeves (48 mm) were used to reduce deposits on the walls of the reactor. The reactor and sleeves were routinely cleaned in a saturated KOH bath, then rinsed with water and methanol. Pressure in the chamber was measured using an MKS Baratron capacitance manometer, which was insensitive to gas composition. An MDC thermocouple vacuum gauge mounted on the foreline was used to confirm the base pressure of the system. The chamber was pumped to a base pressure of < 3 mTorr.

Gaseous starting materials were admitted at the upstream end of the reactor. Gas flow rates were controlled and monitored using MKS mass flow controllers which enable accurate and reproducible metering of gases. Flow rates are reported in standard cubic centimeters per minute (sccm). Nupro shut off valves were located just downstream of the flow controllers to isolate them from the plasma system when venting or not in use. In case of a malfunction of the silane flow controller, it was equipped with an emergency flow by-pass with a Nupro shut off valve.

An eight turn, nickel plated copper coil was used to transfer 13.56 MHz rf power to the reaction chamber. In order to impedance match the capacitance of the chamber with the rf power supply, the rf voltage was tuned with a Jennings 100 pF variable capacitor. The chamber was tuned to resonance by minimizing the reflected power that was returned to the rf power supply and was monitored with the rf power meter on the

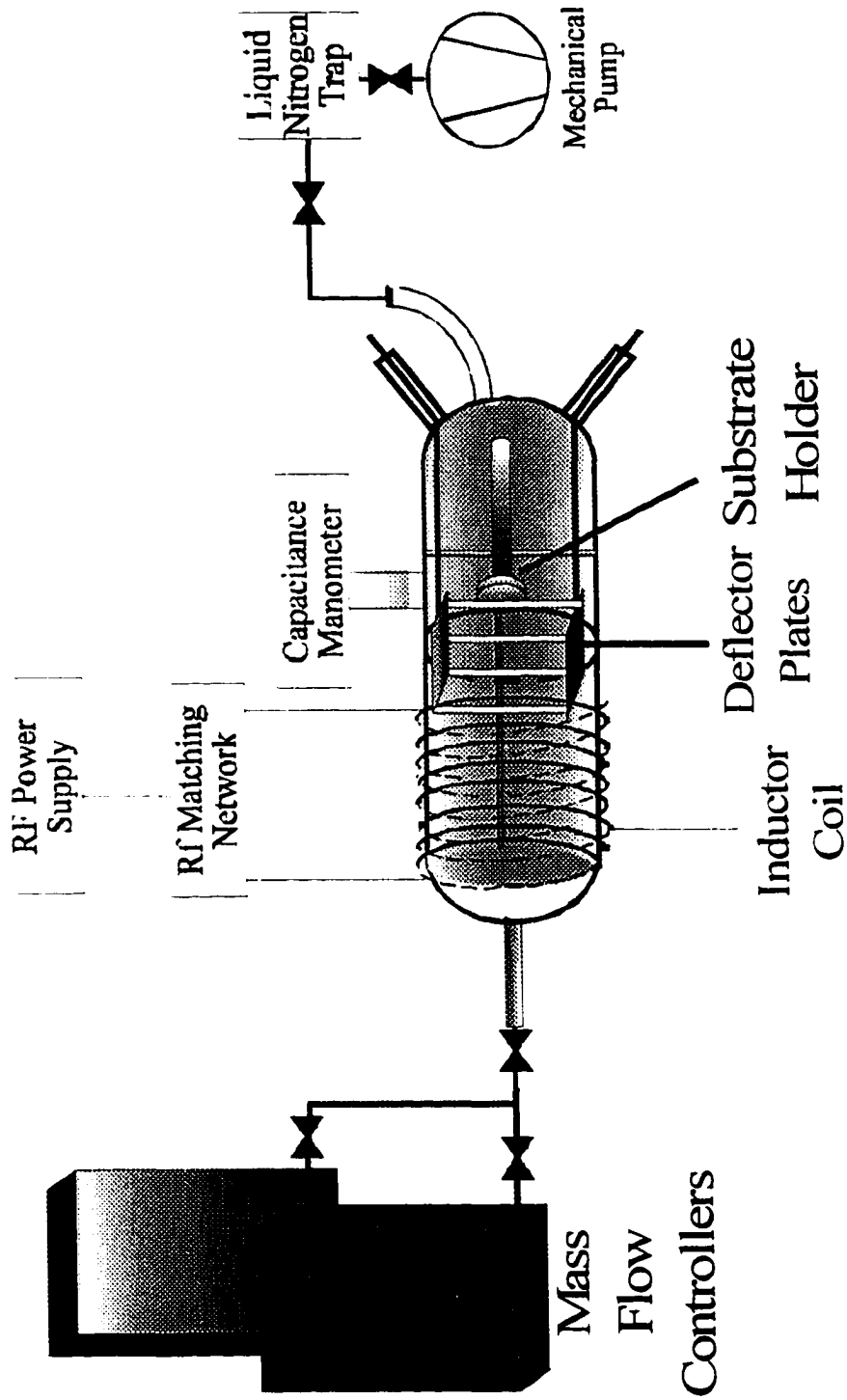

Figure 6.1 Schmatic of the inductively coupled rf plasma reactor apparatus used for depositons of a-$Si_{1-x}C_x$:H

power supply. The rf power was supplied by an RF Power Products (RFPP) RF5S 13.56 MHz power supply.

Silicon substrates were mounted perpendicular to the gas flow 1.0 cm downstream from the coil region and were grounded by mounting them on an Al stub with Cu tape, Fig 6.1. The stub was then grounded to an electrical feed-though into the chamber. Substrates were biased using an Ortec reversible bias, high voltage power supply. Ungrounded substrates were mounted to a glass rod using double stick tape, which was held in position by brackets on a glass sleeve. In Chapter 7, all substrates were ungrounded, while in Chapter 8 all substrates were grounded unless otherwise noted. The deflector plates were made out of two 25 x 33 mm pieces of 1 mm thick Al sheet metal separated by 25 mm ceramic spacers. For experiments using deflector plates, they were placed immediately downstream from the coil, with the length of the plates perpendicular to the flow. The substrate was then mounted ~0.5 cm downstream from the deflector plates (~3 cm behind the last coil), Fig. 6.1.

6.3. PULSED PLASMAS

Pulsed plasmas were used for experiments in both Chapters 7 and 8. Timing for pulsed plasmas was controlled using the internal pulse generator of the RFPP RF5S power supply. This power supply allows variation of peak power delivered during the pulse cycle, the duration of the pulse on time (t_{on}) and the duty cycle of the system. Duty cycle is defined as:

$$Duty\,cycle = \left(\frac{t_{on}}{t_{on} + t_{off}} \right) x100. \qquad 6.1$$

where t_{off} is the time the plasma is off during one cycle. On times can be varied from 2 to 98 ms and duty cycles can be varied from 1 to 99%. It is also important to determine the CW equivalent power. This is simply the time averaged rf power delivered to the system and is defined as:

$$Equivalent\ power = \left(\frac{t_{on}}{t_{on} + t_{off}} \right) (P), \qquad 6.2$$

where P is the peak rf power during the on time. Equivalently powered plasmas provide equal time-averaged applied rf power inputs.

6.4. DEPOSITION CONDITIONS

All gases, CH_4 (Air Products, 99.99%), SiH_4 (Matheson, 99.999%), Ar (Liquid Air, 99%), H_2 (Liquid Air, 99%), He (General Air, >99.5%), were used without further purification. Flows for each gas were as follows: CH_4 = 4.0 sccm, SiH_4 = 1.0 sccm, and diluent gases = 20.0 sccm. Pressure was maintained at 200 mTorr when no diluent gas was used and 400 mTorr when a diluent gas was in the feed.

Ambient substrate temperature was measured immediately after deposition for pulsed and CW plasma samples with an Omega K-type thermocouple and an Omega 115KC thermometer readout. Initial FTIR spectra were taken within 5 minutes of

breaking vacuum on the deposition chamber. Samples were kept under normal atmospheric conditions away from light except when collecting FTIR spectra.

6.5. THIN FILM ANALYSIS

Thin films deposited using our inductively-coupled rf reactor were removed from the plasma chamber and analyzed using a variety of analytical tools. FTIR was used to determine the bonding environment in the bulk of the film. XPS was used to determine film composition (top ~80 Å). SEM was used to determine surface topography. Profilometery was used to determine film thickness and subsequent deposition rates.

6.5.1. FTIR SPECTROSCOPY

Fourier transform infrared (FTIR) spectroscopy is used to identify molecular functional groups by monitoring the absorbance of infrared energy frequencies upon excitation of vibrational (and rotational) states of molecular bonds.[2] To be IR active, a molecule must undergo a net change in dipole moment as a consequence of vibrational (or rotational) motion. The change in dipole moment will create an electromagnetic field which can interact with the IR radiation. For excitation to occur, a molecular bond must absorb IR radiation of the same frequency as its natural vibrational frequency. If the frequency of the natural vibration equals the frequency of the IR radiation, a net transfer of energy will increase the amplitude of the vibration, hence absorption of IR radiation.

Thin a-$Si_{1-x}C_x$:H films deposited in Chapters 7 and 8 were analyzed by transmission FTIR using a Nicolet Magna 760 FTIR spectrometer. The thin films were analyzed by the

transmission through the sample deposited on a Si(100) wafer. Background measurements through a piece of Si(100) from the same wafer as the sample were taken. Each spectrum recorded was the average of 128 scans with a resolution of 8 cm^{-1} or higher over a 4000-500 cm^{-1} range. A HgCdTe (MCT) narrow band detector and KBR beam splitter were used. Spectra shown were converted into absorbance units, and multipoint baselined.

6.5.2. X-RAY PHOTOELECTRON SPECTROSCOPY

XPS is a surface-sensitive spectroscopic tool that provides information about the chemical state and concentration of elements comprising the outermost surface of a solid.[3] When a solid is exposed to a flux of photons with energy $h\nu$ from a monochromatic X-ray source, a core (K) orbital electron is displaced with some measurable energy. If we know the energy of the X-ray source and can measure the energy of the displaced electron we can determine not only the element the electron came from, but also something about its bonding environment.

The kinetic energy of the emitted electron, E_k, is measured in an electron spectrometer. The binding energy, E_b, can then be calculated by means of the equation

$$E_b = h\nu - E_k - w \qquad 6.3$$

where w is the work function of the spectrometer, a factor that corrects for the electrostatic environment in which the electron is measured.[4]

Photoelectrons are generally characterized by short mean free paths within a solid. Photoemitted electrons traveling through a solid have a relatively high probability of

interacting with neighboring atoms and undergoing inelastic energy loss processes before leaving the sample surface. Only photoelectrons that are generated very near the surface (~80 Å or less) escape without loss in energy and appear in the spectra at discrete energies above a background of inelastically scattered electrons.

XPS analyses were performed on a Surface Science Instruments S-probe spectrometer located at the University of Washington, NESAC-BIO center. This system has a monochromatic Al Kα X-ray source ($h\nu$ = 1486.6 eV), hemispherical analyzer and resistive strip multichannel detector. A low energy (~5 eV) electron gun was used for charge neutralization on the nonconducting samples. The binding energy (BE) scales for the samples were referenced to the Si_{2p} peak of SiC at 100.2 eV.[5] The high-resolution C_{1s} spectra were acquired at an analyzer pass energy of 25 eV and a X-ray spot size of 1000 μm. XPS elemental compositions of samples were obtained using a pass energy of 150 eV. All XPS analyses were performed at a photoelectron take-off angle of 55°.

6.5.3. SCANNING ELECTRON MICROSCOPY

The primary use of SEM is the study of the surface topography of solid samples.[6] The resolution of the SEM is typically between 1.5 and 3.0 nm, approximately two orders of magnitude better than optical microscopes and one order of magnitude less than transmission electron microscopes, thereby bridging the gap between these two techniques. One advantage of SEM imaging over these other techniques is its enhanced depth of field.

The general principle of SEM is that an electron beam passing through an

evacuated column is focused by electromagnetic lenses onto the sample surface. The electron beam is rastered over the spectrum simultaneously with an electron beam that 'paints' the cathode ray tube (CRT). Secondary electron emission from the sample (determined by surface topography) is then used to modulate the electron flux to the CRT, thereby forming the image. Back-elastically scattered electrons can also be used to form the image. Here, image contrast is determined largely by compositional differences of the sample surface rather than topographical features.

Film morphology was determined using a Philips 505 scanning electron microscope with an accelerating voltage of 20 kV and a spot size of 20 nm. The films were sputtered with 20 nm of gold prior to SEM analysis.

6.5.4. PROFILOMETRY AND FILM DEPOSITION RATE

A portion of the silicon wafer was masked with transparent tape prior to deposition. Immediately after deposition the tape was removed, leaving a clean edge between the deposited film and the substrate. Film thicknesses were then obtained by measuring the resulting step height from the substrate to the film surface using a profilometer (Tencor Alpha Step 100). Deposition rates for films are reported in Å/min. For pulsed plasma depositions rates are also reported in Å/pulse.

6.6. PLASMA ANALYSIS

Optical methods are important in plasma processing because they provide in-situ monitoring of the plasma composition.[7] Measurements of the plasma composition can

provide insight into the processes occurring in the plasma, as well as on the surface being processed. The unique capability of optical methods is that they can provide real-time analysis of species without disturbing the plasma or interfering with the process.

In particular, optical emission spectroscopy (OES) has found extensive use as a plasma diagnostic tool. This largely is because plasmas naturally emit light, so only a spectrometer or monochrometer is required for this technique.

6.6.1. OPTICAL EMISSION SPECTROSCOPPY

OES is widely used to characterize plasmas.[8] The method relies on detection of emission from plasma species in their electronically excited states. The electronic excitation is imparted by some process occurring within the discharge, most often simply electron impact excitation.[9] It is usually straightforward to identify the emitting species and follow qualitative changes in plasma properties as a function of various plasma parameters. However, because OES measures the emission from the excited state, and the majority of the species in a plasma are in their ground electronic state, OES does not necessarily give a good indication of the overall populations of the various plasma species.[10]

Optical emission spectra were obtained by adding a fused silica window located at the downstream end of the reactor. The placement of the window allows for coaxial observation of emission from the plasma. Emissions were collected by optical fibers and transmitted to the entrance of a modified Ocean Optics S2000 triple spectrometer. In order to achieve high spectral resolution and to cover a reasonable range of

wavelengths–253 - 703 nm–3 separate spectrometers are used. Each spectrometer contains a 10 mm slit, a 1800 lines/mm holographic grating and a 2048 element charge-coupled device. The spectrometer had a resolution of < 0.3 nm, with wavelength ranges of 253.65 - 456.96 nm, 453.84 - 579.07 nm, and 576.96 - 703.24 nm.

REFERENCES

1 K. H. A. Bogart, N. F. Dalleska, G. R. Bogart, and E. R. Fisher, J. Vac. Sci. Technol. *A* **13**, 476 (1995).

2. D. A. Skoog and D. M. West, *Principles of Instrumental Analysis, 2nd ed.* (Holt, Rinehart and Winston, Philidelphia, 1980).

3. E. A. Leone and A. J. Signorelli, *Materials Characterization and Chemical Analysis, 2nd ed.* edited by J. P. Sibilia (VCH, New York, 1996).

4. D. A. Skoog and J. L. Leary, *Principles of Instrumental Analysis, 4th ed.* (Saunders College, Orlando, FL, 1992).

5. K. L. Smith and K. M. Black, J. Vac. Sci. Technol A **2**, 744 (1984).

6. R. E. Lee, *Scanning Electron Microscopy and X-ray Microanalysis* (Prentice Hall, Englewood Cliffs, NJ, 1993).

7. I. P. Herman, *Optical Diagnostics for Thin Film Processing* (Academic, San Diego, CA, 1996).

8 R. W. Dreyfus, J. M. Jasinski, R. E. Walkup, and G. S Selwyn, Pure and Appl. Chem., *57*, 1265 (1985).

9. W. L. Fite, *Chemical Reactions in Electrical Discharges*, edited by R. F. Gould (American Chemical Society, Washington D.C. 1969)

10. G. Hancock, L. Lanyi, J. P. Sucksmith, B. K Woodcock, Pure Appl. Chem., 66, 1207 (1994).

CHAPTER 7

COMPARISON OF OXIDATION RATES FOR a-$Si_{1-x}C_x$:H FILMS DEPOSITED FROM PULSED AND CONTINUOUS WAVE RF PLASMAS

7.1. INTRODUCTION

Hydrogenated amorphous silicon carbide (a-$Si_{1-x}C_x$:H) has been studied extensively for the past several years due to its unique properties.[1,2,3] This interesting material has found applications in solar cells,[4,5] flat panel displays, photoreceptors,[6] and more recently as a photoresist material.[7] The ratio of Si to C (as well as the amount of H) in a-$Si_{1-x}C_x$:H films can vary over a wide range, as can the mechanical and optical properties.[8] For example, the optical band gap of a-$Si_{1-x}C_x$:H can vary from that of a-Si:H, ~1.75 eV, to that of a-C:H which has a band gap as large as 4.0 eV.[9] The electrical properties of these films, however, tend to rapidly deteriorate as the C content increases.[10,11] It has also been shown that the amount of H and its bonding environment in these films are extremely important to film quality.[12] Because of preferential bonding of hydrogen to carbon over silicon,[13] CH_3 groups are introduced into the a-$Si_{1-x}C_x$:H film structure. These methyl groups are believed responsible for microvoids and electrical instability in a-$Si_{1-x}C_x$:H films.[14,15] If this microstructure is eliminated from a-$Si_{1-x}C_x$:H films, better photoconductivity and higher band gap materials would be possible.[4] There is, however, a lack of understanding of both the chemical structure of these films and how the structure

affects their physical and electrical properties.

Another serious issue affecting the mechanical and electrical properties of plasma deposited a-$Si_{1-x}C_x$:H films is their tendency to oxidize rapidly upon exposure to atmosphere. Eldridge and coworkers have characterized the oxidation of a-$Si_{1-x}C_x$:H by X-ray photoelectron spectroscopy (XPS), Rutherford backscattering (RBS) and profilometry.[16] Their work demonstrated that the kinetics of oxidation are sensitive to film composition, and that the oxidation rate increased with increasing amounts of both carbon and hydrogen in the films. John et al. demonstrated that normally stable a-$Si_{1-x}C_x$:H films can be photo-oxidized at room temperature in air using UV/visible light from a Xe arc lamp or an Ar ion laser.[17,18] They also noted that the rate of this process increased with increasing carbon content of the film, but found the bonding environment was also critical in the oxidation process. Specifically, microvoids associated with Si-CH_3 terminating groups were considered a key factor in increasing the rate of the photo-oxidation of a-$Si_{1-x}C_x$:H. Oxygen is believed to diffuse into the film through these microvoids and insertion of an O atoms into Si-Si bonds then occurs through photooxidation.[17]

Alok and Baliga used ion implantation of hexagonal SiC to deliberately amorphize its surface and study the effects of oxidation with and without amorphization.[19] As a result of this amorphization, they were able to grow a thermal oxide layer more rapidly on the surface of hexagonal SiC than on an untreated surface using a dry oxygen atmosphere. Additionally, the oxide growth rate was parabolic in the amorphized region while the monocrystalline region exhibited a mixed linear-parabolic growth rate. This difference was attributed to the increased number of reactive surface sites in the amorphized region.[19]

Moreover, Alok and Baliga concluded that diffusion of reactant through the oxide, rather than surface reaction, was the rate-determining step for the amorphized material. Kodama et al. exposed a-$Si_{1-x}C_x$:H films to a corona discharge and monitored the resulting oxidation species using FTIR.[20] They found evidence of adsorbed water (Si-OH and H-OH stretching frequencies) along with oxidation species (Si-O-Si) which increased with exposure time. Contact angles for these films also changed with discharge exposure time. Thus, the ability to control the rate of oxidation for a-$Si_{1-x}C_x$:H is important for the application of these materials in semiconducting devices.

We have previously reported the use of pulsed rf plasmas to produce a variety of organic films with a high degree of controllability over film composition.[21,22] The feed gases we have examined include mixtures of saturated fluorocarbons (primarily C_2F_6) and H_2,[21] as well as aromatic precursors (C_6H_6, 1,2,4-$C_6H_3F_3$, and C_6F_6),[22] benzaldehyde,[23] acetonitrile and acrylonitrile.[24] Use of pulsed sources to create organic films has been shown to reduce trapped radicals in the depositing films, lower deposition surface temperatures, decrease high energy ion bombardment and UV flux to the surface, and provide greater control over the resulting film chemistry.[25] Since oxidation of a-$Si_{1-x}C_x$:H films can be affected by the concentration of trapped radicals in the film, the present work was undertaken to determine if oxidation of a-$Si_{1-x}C_x$:H films can be controlled through the use of pulsed plasmas. Additionally, having the control over film chemistry possible with pulsed plasmas is vital to achieving desired film properties for these films.

While there has been considerable work on the use of continuous wave (CW) plasmas to deposit a-$Si_{1-x}C_x$:H films,[2,26,27] there has only been one previous study using a

pulsed plasma.[25] In this study, a-$Si_{1-x}C_x$:H was deposited in a pulsed, capacitively-coupled plasma using vinyltrimethyl-silane [$(CH_3)_3Si\text{-}C_2H_3$] as the precursor. Oxidation rates for the films, however, were not measured. Here, we use Fourier transform infrared (FTIR) spectroscopy to determine relative oxidation rates of a-$Si_{1-x}C_x$:H films deposited from CW and equivalently powered pulsed SiH_4/CH_4 plasmas. Oxidation rates for films produced from SiH_4/CH_4 plasmas with the diluent gases Ar, He, H_2 added to the feed are determined, and XPS analysis is also provided on aged samples.

7.2. RESULTS

FTIR Spectra. Figure 7.1 shows two FTIR spectra of an a-$Si_{1-x}C_x$:H film deposited using a 5 W CW SiH_4/CH_4 plasma, taken immediately after deposition and five days later. The major difference in the two spectra is a significant increase in intensity of the Si-O-Si bridging absorbance at ~1030 cm^{-1} with time. Other differences between the two spectra include: a large decrease in the SiH_x rocking and wagging modes at ~685 cm^{-1}, a broadening of the SiH stretching frequency at ~2100 cm^{-1}, a shift to slightly higher frequency of the SiH stretch, and a decrease in intensity of the CH_3 ν_{sym} stretch at ~2900 cm^{-1}. The decrease in the SiH intensity and shift to higher stretching frequency are likely the result of Si-H bonds in the film being replaced by Si-O bonds.[16]

Interestingly, there is only a small absorbance peak at ~3400 cm^{-1} in Fig. 7.1b, the Si-OH stretching region. Presence of SiOH moieties would be expected if oxidation was occurring through reaction with atmospheric H_2O. To determine if the observed oxidation was the result of exposure to atmospheric oxygen or atmospheric water, two a-$Si_{1-x}C_x$:H

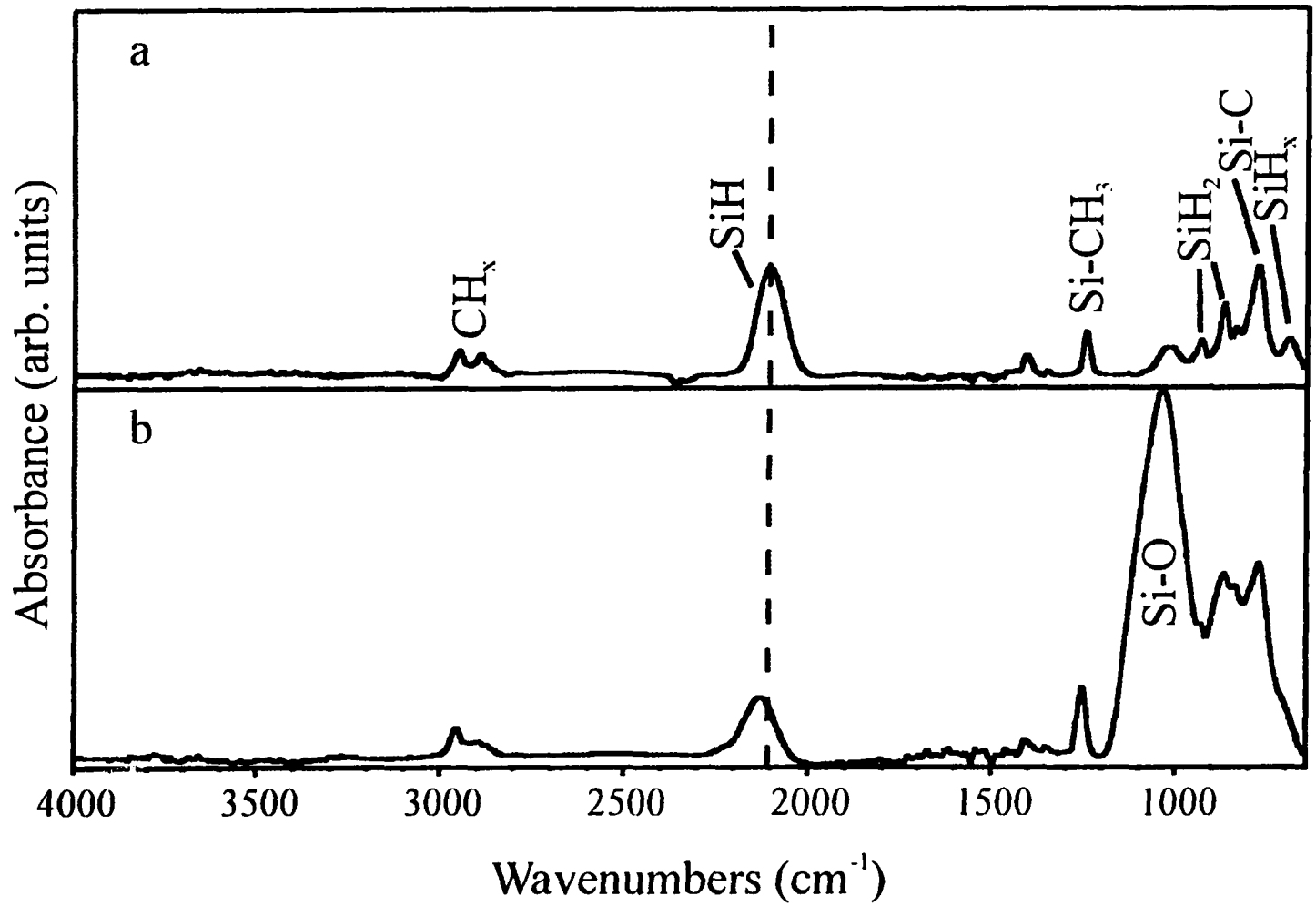

Figure 7.1. FTIR transmission spectra for an a-$Si_{1-x}C_x$:H film deposited from a 5 W CW SiH_4/CH_4 plasma: (a) immediately after deposition and (b) 5 days after deposition. The line indicates the the peak of the initial Si-H stretching frequency at 2105 cm^{-1}. A shift of 26 cm^{-1} is observed during oxidation.

films were produced under identical CW plasma conditions, but were given different post deposition treatments. One film was placed in a desiccator immediately after deposition, while the other was exposed to ambient laboratory conditions. Both films showed the same large increase in the SiO stretch, with only small amounts of SiOH stretching even after many days.

Figure 7.2 contains two FTIR spectra of an a-$Si_{1-x}C_x$:H film deposited using a 500 W, 1% duty cycle pulsed SiH_4/CH_4 plasma. The spectra shown in Figure 7.2a, taken immediately after deposition, is much less complicated than that shown in Fig. 7.1a for the CW film. Most significantly, there are no SiH/SiH_2 bending modes at 685 cm^{-1}, 840 cm^{-1}, and 890 cm^{-1} and the Si-C peak is broader and shifted to higher frequency (830 cm^{-1} versus 770 cm^{-1}). Wieder et al. have noted that this band in amorphous unhydrogenated SiC shifts to higher frequencies upon crystallization.[28] Also, while the 2800-3000 cm^{-1} region shows primarily CH_3 moieties in the CW film, the pulsed plasma film shows both CH_2 and CH_3 stretching modes. Figure 7.2b is the FTIR spectrum of the same film, five days after deposition. Although this spectra shows an increase in the Si-O-Si stretching at 1030 cm^{-1}, the change is not as pronounced as with the CW film, Fig. 7.1b. There is no significant Si-OH stretching absorbance at ~3400 cm^{-1}, suggesting very little absorption of water occurs on these films during oxidation.

Relative amounts of Si-H and C-H bonds for the a-$Si_{1-x}C_x$:H films can be obtained by integrating the area under the absorbance peaks for the C-H stretching region (2800-3000 cm^{-1}) and the Si-H stretching region (~2100 cm^{-1}). Table 7.1 lists the C-H/Si-H ratios obtained by this analysis for films deposited from both pulsed and CW plasmas

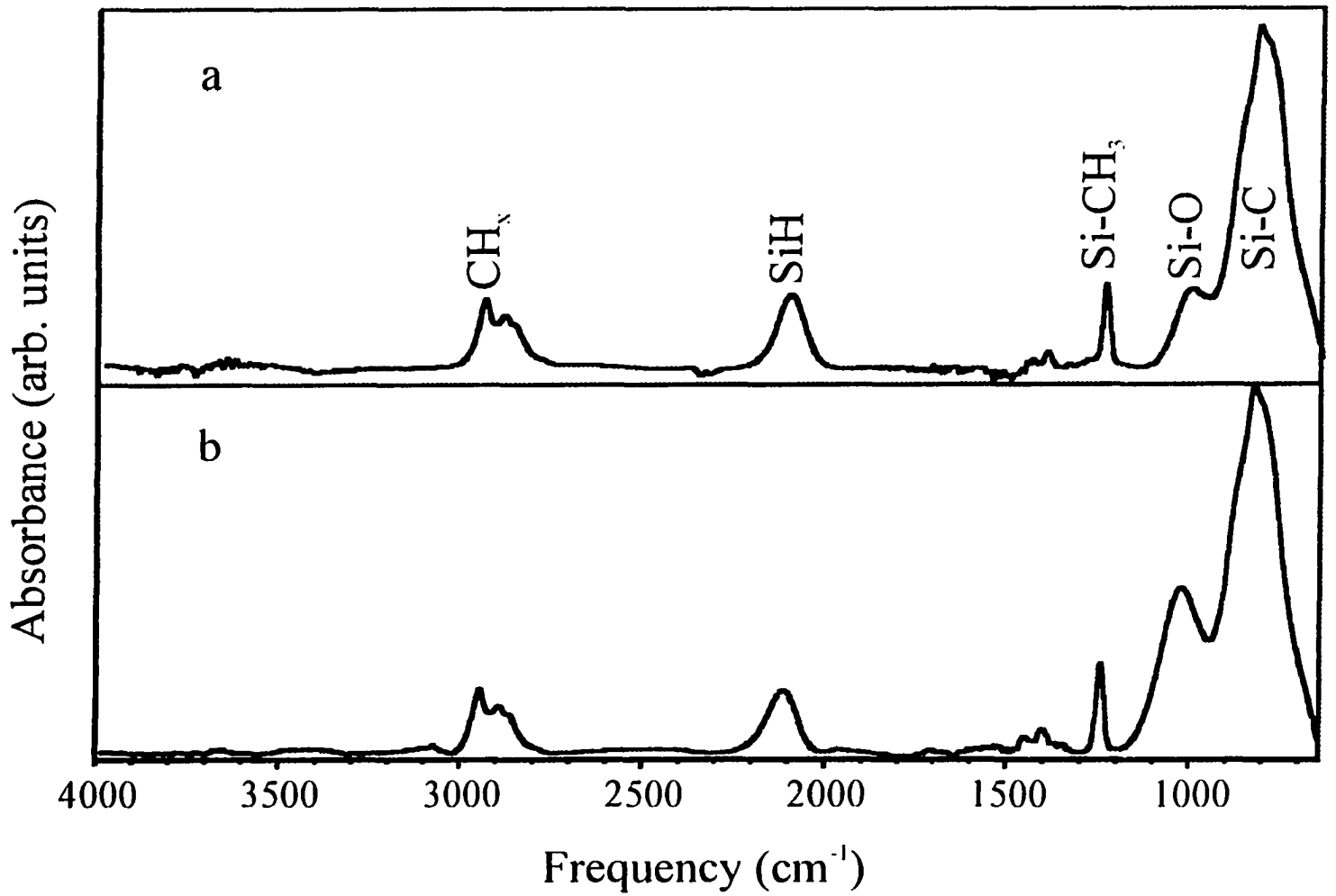

Figure 7.2. FTIR transmission spectra for an a-$Si_{1-x}C_x$:H film deposited from a pulsed SiH_4/CH_4 plasma: (a) immediately after deposition and (b) 5 days after deposition.

Table 7.1. Relative Si-H and C-H content of a-$Si_{1-x}C_x$:H Films[a]

Plasma Reactants	C-H/Si-H	$Si-CH_3$/Si-H
CW SiH_4/CH_4	0.24 ± 0.08	0.08 ± 0.02
Pulsed SiH_4/CH_4	1.03 ± 0.39	0.23 ± 0.05
CW SiH_4/CH_4/Ar	0.56 ± 0.15	0.17 ± 0.05
Pulsed SiH_4/CH_4/Ar	0.91 ± 0.16	0.14 ± 0.03
CW SiH_4/CH_4/He	0.22 ± 0.03	0.08 ± 0.01
Pulsed SiH_4/CH_4/He	0.70 ± 0.04	0.16 ± 0.02
CW $SiH_4/CH_4/H_2$	0.14 ± 0.04	0.07 ± 0.01
Pulsed $SiH_4/CH_4/H_2$	0.50 ± 0.20	0.13 ± 0.05

[a]Based on integrating the area under the absorbance peaks for the C-H stretching region (~2900-3000 cm^{-1}), the Si-H stretching region (~2100 cm^{-1}), and the $Si-CH_3$ bending mode (~1250 cm^{-1}) [see Ref. 32]. Analysis was performed on spectra taken of films immediately after deposition. Error limits are one standard deviation of the average values for a minimum of three samples, and indicate the reproducibility of the analysis.

(initial values).[29] Also listed in Table 7.1 are the Si-CH_3/Si-H ratios (using the Si-CH_3 bending mode at ~1250 cm^{-1}). As can be seen from these data, the C-H/Si-H ratio is higher for the films produced in the pulsed systems. The lowest ratio occurs in the H_2 system, while the highest occurs in the SiH_4/CH_4 pulsed system. The latter is also the system with the highest Si-CH_3/Si-H bonding ratio.

XPS Analysis. XPS analysis was performed on a-$Si_{1-x}C_x$:H films deposited on Si substrates from pulsed and CW plasmas with no dilution, H_2 dilution, and He dilution. Analysis was performed ~4 days after the films were deposited. Surface elemental composition for these films are listed in Table 7.2. For all samples, only Si, C, and O were detected. Regardless of the dilution, the amount of oxygen present in the CW films is approximately twice that of the pulsed films. Note that we observe the same amount of O incorporated in all three CW films, even though the oxidation rate is significantly decreased in the H_2 system, as measured by FTIR. We believe this is a result of the difference in sampling depths of the two analysis techniques. The XPS analysis is only sampling the outer ~80 Å of the film, whereas the FTIR analysis yields the bulk film properties.

The stoichiometric Si:C ratio for the CW films is significantly different with H_2 dilution, changing from 0.56:0.44 and 0.53:0.47 with no dilution and He dilution, respectively, to 0.65:0.35 with H_2 dilution. In contrast, for the pulsed films, the stoichiometric Si:C ratio stays nearly constant at ~0.4:0.6 for all gas compositions, Table 7.2. These results suggest that the gas composition does not greatly alter the film chemistry in the pulsed systems, but the addition of H_2 in the CW plasma does play a

Table 7.2. Atomic Stoichiometries for aged a-$Si_{1-x}C_x$:H Films[a]

	atom %		
Plasma Reactants	**Si**	**C**	**O**
CW SiH_4/CH_4	37.7	29.2	33.1
Pulsed SiH_4/CH_4	36.5	48.2	15.4
CW SiH_4/CH_4/He	36.1 ± 0.3	32.3 ± 0.5	31.7 ± 0.3
Pulsed SiH_4/CH_4/He	35.2 ± 0.7	52.3 ± 0.8	12.5
CW $SiH_4/CH_4/H_2$	45.1 ± 0.1	24.6 ± 0.4	30.3 ± 0.4
Pulsed $SiH_4/CH_4/H_2$	32.4	51.5	16.2

[a]XPS analysis was performed on a-$Si_{1-x}C_x$:H films four days after deposition. Error limits given on selected samples are one standard deviation of the average values for the samples, and indicate the reproducibility of the analysis.

significant role in determining the film chemistry. This is discussed further below.

Deposition rates. Deposition rates for films in both the CW and pulsed systems are listed in Table 7.3. These should be considered as average deposition rates for the entire deposition period (30 min). Note that deposition rates for the pulsed systems are consistently higher than for the CW systems by 200-400 Å/min. This suggests significant deposition occurs during the off times, as well as during the on times in the pulsed systems. This has been observed previously for different monomers.[21,22] For the SiH_4/CH_4, SiH_4/CH_4/He, and SiH_4/CH_4/Ar gas mixtures, the deposition rates are essentially the same for the pulsed systems, ~650 Å/min, and range from ~250-400 Å/min for the CW systems. With H_2 as the diluent gas, however, the deposition rates decrease significantly for both the pulsed and CW systems, dropping to ~440 Å/min and ~180 Å/min, respectively.

Relative Oxidation Rates. Relative oxidation rates were determined by measuring the change in the ratio of the absorbance peak height of the Si-O-Si bridging vibration at ~1030 cm^{-1} to the peak height of the Si-C absorbance band at ~800 cm^{-1} as a function of time for both CW and pulsed systems, Fig. 7.3. Figure 7.3a shows the change in oxidation as a function of time for films deposited from SiH_4/CH_4 plasmas with no dilution gas. Clearly, the CW film oxidizes much more rapidly than the film deposited in the pulsed plasma. For both films, the Δ(Si-O-Si/Si-C) absorbance ratio increases rapidly with time before leveling off at longer times.

Figures 7.3b and 7.3c show the Δ(Si-O-Si/Si-C) absorbance ratios for films deposited with He or Ar added as a diluent. Under these conditions, CW plasma

Table 7.3. Average Deposition Rates for a-$Si_{1-x}C_x$:H Films[a]

Reactants	Pulsed	CW
SiH_4/CH_4	670 ± 40	380 ± 20
$SiH_4/CH_4/He$	670 ± 110	240 ± 30
$SiH_4/CH_4/Ar$	650 ± 80	260 ± 40
$SiH_4/CH_4/H_2$	440 ± 40	180 ± 30

[a]Values given in Å/min. Error limits represent one standard deviation of the mean for several samples.

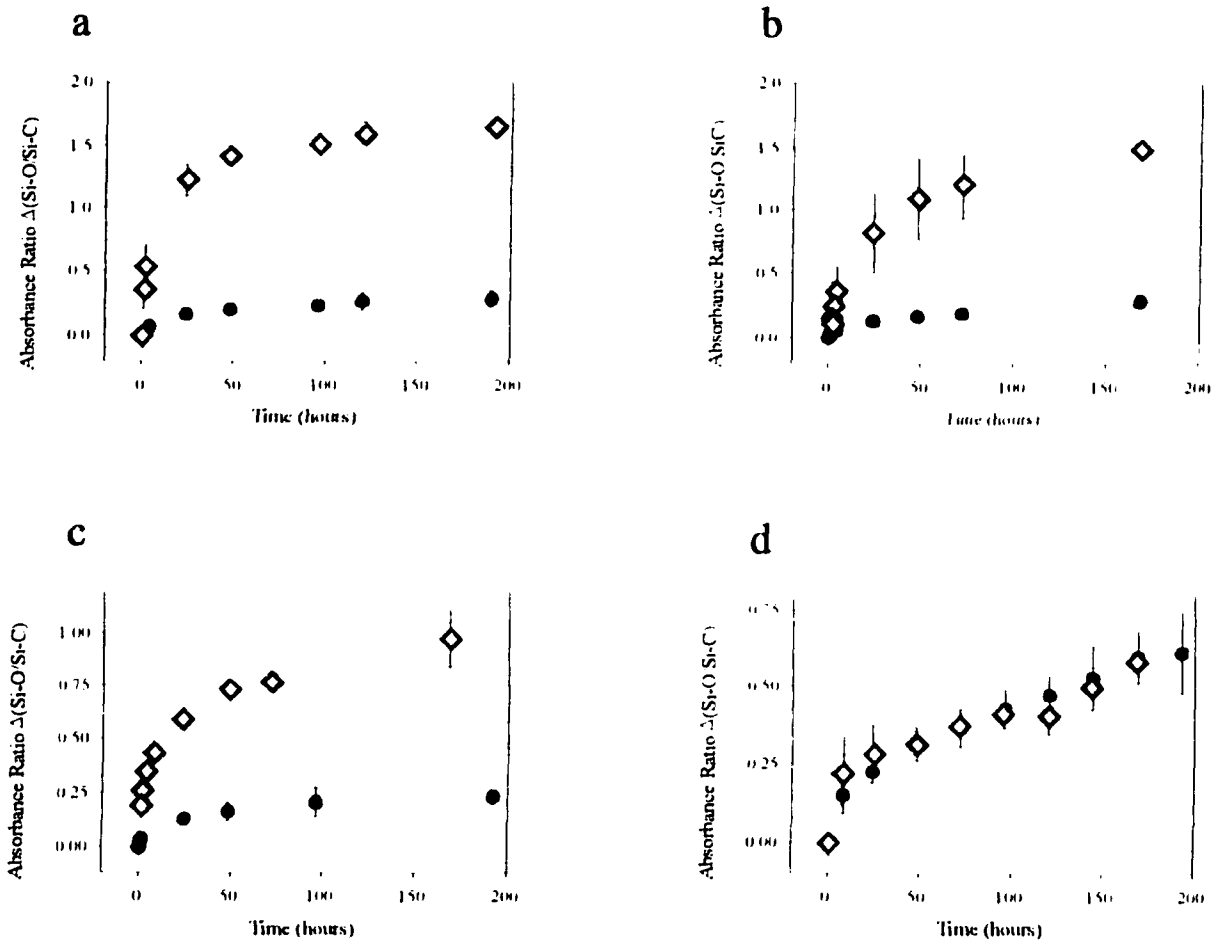

Figure 7.3. Change in the ratio of peak absorbance values for the Si-O-Si bridging absorption (1030 cm^{-1}) to the Si-C stretch (~800 cm^{-1}) as a function of time for a-$Si_{1-x}C_x$:H films deposited from SiH_4/CH_4 pulsed (solid circles) and CW (open diamonds) plasmas with (a) no dilution gas; (b) with He diluent gas; (c) with Ar diluent gas, and (d) with H_2 diluent gas. In (d) the CW deposition time was 90 min and the pulsed deposition time was 30 min. All other data shown are for 30 min depositions. Error bars represent one standard deviation of the mean values.

deposited films oxidized much more rapidly than their pulsed plasma counterparts, similar to the films formed with no dilution, Fig. 7.3a. Indeed, with He as the diluent, Fig. 7.3b, there is virtually no change in the amount of oxygen incorporated in the film deposited under pulsed conditions. Even after ~58 days exposure to atmosphere, we still observe little change in oxygen content. In the same CW system, however, there is nearly an order of magnitude change in the Si-O-Si/Si-C absorbance ratio over the same time period, Fig. 7.3b.

In contrast, when H_2 is used as the diluent gas, Fig. 7.3d, the film produced in the CW plasma oxidizes much more slowly than that formed in other CW plasma systems. Note that the CW data shown in Fig. 7.3d are for films deposited for 90 min rather than 30 min. This was done to account for the significant differences in film deposition rates between the CW and pulsed systems, Table 7.3. Note that the films produced under these CW conditions oxidize at the same rate as films produced in pulsed plasmas, Fig. 7.3d.

Figure 7.4 shows two FTIR spectra for a film deposited from a $SiH_4/CH_4/H_2$ CW plasma (deposition time, 30 min), one taken immediately after deposition and the other 151 days after deposition. Note that after 151 days exposure to atmosphere, there is a small increase in the Si-O-Si absorbance at 1020 cm^{-1}, and that the film's FTIR spectrum is very similar to that of the CW film deposited with no diluent gas flow, Fig. 7.1a. There is, however, a significant decrease in the amount of CH_x bonding (absorbance bands at 2900-3000 cm^{-1}), and the $SiCH_3$ bending mode at 1250 cm^{-1}, relative to SiC bonding. In addition, the absorbance peaks unique to the CW depositions (i.e. the SiH_x bending modes at 685, 840, and 890 cm^{-1}) are very distinct in the film deposited with H_2, suggesting a

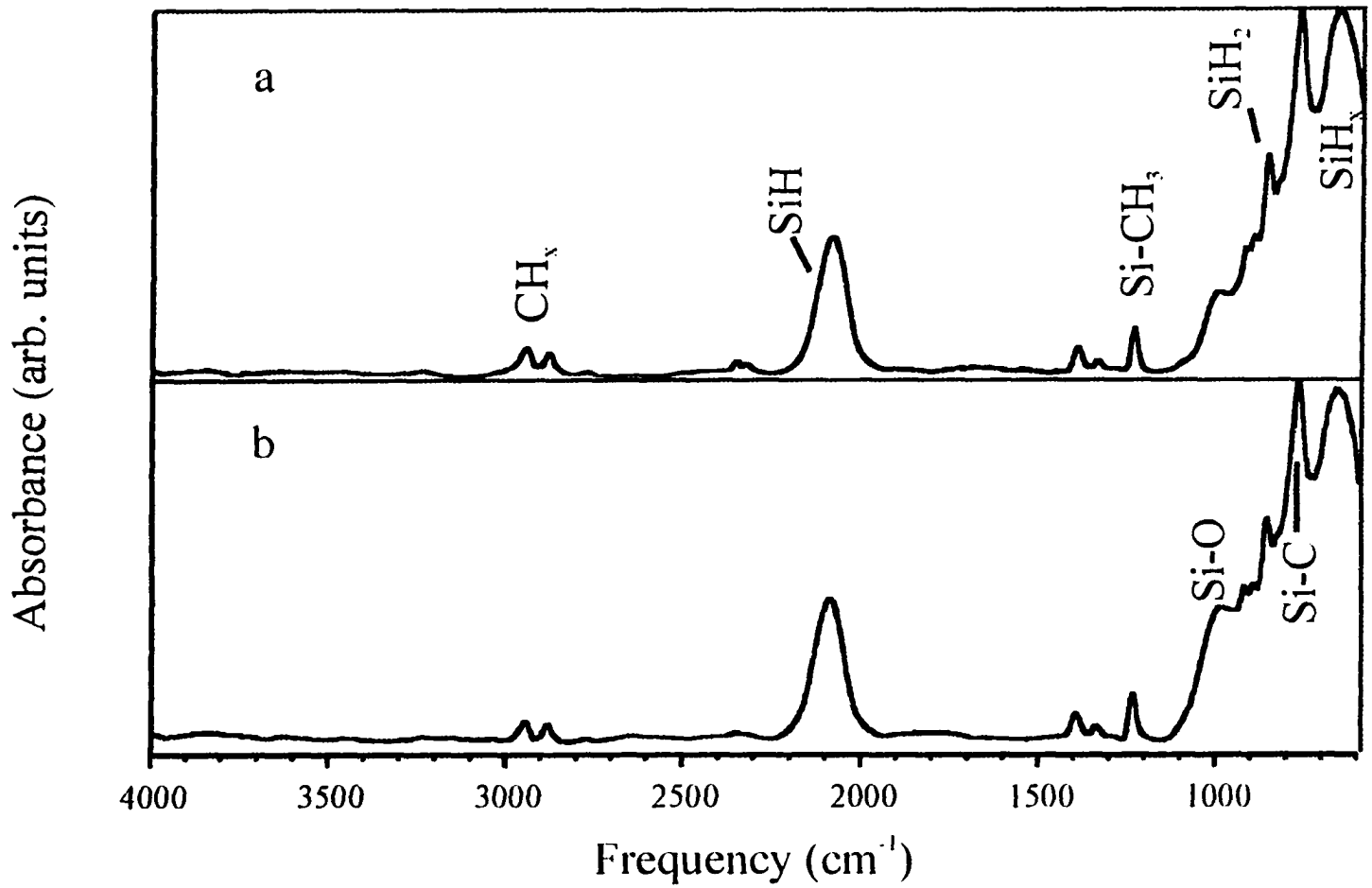

Figure 7.4. FTIR transmission spectra for an a-$Si_{1-x}C_x$:H film deposited from a pulsed $SiH_4/CH_4/H_2$ plasma: (a) immediately after deposition and (b) 151 days after deposition.

greater degree of Si-H bonding in these films. This is discussed in more detail below.

7.3. DISCUSSION

As noted in the Introduction, pulsed plasma systems offer an alternative to CW plasma deposition, and can provide films with unique structures not obtainable through other methods. Recently, we have conducted several studies of pulsed plasma polymerization of organic starting materials,[21-24] as have Timmons and coworkers.[25,30,31] It is generally believed that with pulsed plasmas, neutral radicals and molecules passivate the growing surface during the off time by reacting with dangling bond sites created by ion bombardment during the on time. In contrast, films deposited in CW plasmas are subject to constant ion bombardment, leading to trapped radicals within the material. These radicals can undergo subsequent reaction, including oxidation, when exposed to atmosphere.[32]

Our results on the oxidation of pulsed and CW plasma deposited a-$Si_{1-x}C_x$:H films support this hypothesis. Although silicon carbide is a relatively inert material, the surface of the carbide can oxidize rapidly upon exposure to air.[16] It is clear from Figs. 7.3a-c that films deposited in CW plasmas with SiH_4/CH_4, SiH_4/CH_4/He and SiH_4/CH_4/Ar gas mixtures oxidize considerably faster than films deposited from equivalently powered pulsed plasmas. Upon exposure to atmosphere, radical sites in the films react with O_2 to create Si-O-Si/Si-O-C moieties within the film. Since the CW-plasma deposited films have a greater degree of trapped radicals, they oxidize at a faster rate than the pulsed plasma deposited films. At longer times, the rate of oxidation slows for all films,

suggesting that the rate limiting step at long times is diffusion through the material, rather than reaction at the surface of the material.[19] It is likely that the surface is oxidized rapidly upon exposure to air, even before the initial IR can be taken. Indeed, all IR's show either a distinct peak or shoulder at ~1030 cm^{-1}, corresponding to the Si-O-Si bridging mode.

The a-$Si_{1-x}C_x$:H films deposited with H_2 as a diluent gas do not, however, exhibit the same oxidation behavior. With H_2 in the plasma, the films deposited in the CW system oxidize slower than those from the other CW systems. It is interesting to note that the Si/C ratio increases significantly with H_2 addition, Table 7.2. Moreover, film deposition rates are significantly decreased in the H_2 system, Table 7.3. These two observations suggest that H_2 is a factor in gas-phase reactions occurring in the plasma, as well as in the gas-surface interactions leading to film deposition.

This change in oxidation behavior is likely the result of hydrogen reacting with the depositing film. In a H_2-based plasma, the depositing film is constantly bathed with hydrogen molecules and radicals. It is generally believed that the latter species anneal the growing film surface by abstracting bonded hydrogen atoms and methyl groups,[33] accounting for the decreased hydrogen content in the films. This is also true for chemical vapor deposition (CVD) synthesis of diamond films,[34] and other tetrahedral semiconductor films.[36] With a-$Si_{1-x}C_x$:H depositions, H_2 dilution in the plasma has been shown to increase the fraction of Si-C bonds and to shift network vibrations in the resulting films to higher frequency.[13] We also note that the fraction of CH_x bonding in our films is decreased with H_2 addition, Fig. 7.4. This is in good agreement with the results of previous studies,[12,13-18] and suggests fewer microvoids are present in these films. Gas phase reactions between H

atoms and SiH_4 to create SiH_x, or recombination of H atoms with CH_3(g) radicals could also be a factor in the decreased carbon content of the H_2 diluted films.

All of this helps explain our observation that the addition of H_2 to the plasma feed gas reduces the oxidation rate of the CW films. Specifically, hydrogen "anneals" the surface of the CW film by reacting with dangling bonds in the CW film. The ability to anneal the surface by hydrogen addition assumes there are many surface active sites in the film. As noted above, if these active sites are essentially radical sites, there are likely to be fewer active sites with the pulsed system than with the CW system. Higher substrate temperatures have also been shown to anneal a-$Si_{1-x}C_x$:H films with and without H_2 present during deposition through hydrogen desorption.[35] Annealing at elevated substrate temperatures also slows the rate of oxidation.[36] With our films, substrate temperature is not a contributing factor to the observed annealing with H_2 dilution in the CW depositions. Indeed, the ambient substrate temperature is considerably lower in the CW systems (45 ± 5 °C) than that found with the pulsed depositions (75 ± 10 °C).

It is likely that O_2 is the primary species oxidizing the a-$Si_{1-x}C_x$:H films. This is supported by the minimal Si-OH stretching in the FTIR spectra (~3400 cm^{-1}) for both CW and pulsed films, which indicates little H_2O is adsorbing either in the microvoids or on the surface of the films, Figs. 7.1 and 7.2. A previous study of the oxidation of a-$Si_{1-x}C_x$:H films using a corona discharge as the oxidation source showed significant amounts of silanol incorporation in the films, along with the Si-O-Si species.[20] Additional adsorption species such as NO_3^- and CO_3^- were also observed in this study, indicating further reaction between ozone and other atmospheric molecules. Thus, exposure to corona discharge

leads not only to oxidation of a-$Si_{1-x}C_x$:H, but also to hydrophilic adsorbed species that further contribute to the degradation of the film properties.

Some insight into possible oxidation mechanisms for our a-$Si_{1-x}C_x$:H films can be gained by considering past studies of the thermal oxidation of silicon and silicon carbide. Deal and Grove developed a linear-parabolic model to describe the kinetics of thermal oxidation of silicon.[37] Costello and Tressler used this model to describe the oxidation kinetics of silicon carbide crystals.[38] While highly crystalline samples obeyed the Deal and Grove model reasonably well, higher impurity concentrations in the crystals significantly complicated the oxidation behavior. Eldridge and coworkers also attempted to use the Deal and Grove model to describe oxidation mechanisms for a-$Si_{1-x}C_x$:H films, and note that the oxidation of these films is extremely complex.[16]

In order to compare these results with ours, we have plotted the relationship between oxide thickness (assumed to be proportional to absorbance) and time on a logarithmic plot in Fig. 7.5. Slopes for these data range from 0.1 - 0.4, significantly lower than would be expected for pure parabolic behavior, $m = 0.5$. We have further manipulated our oxidation data to strictly apply the Deal and Grove model, eq. 7.1,

$$x_o^2 + Ax_o = B(t+\tau) \qquad y = (x_i^2 + Ax_i)/B \tag{7.1}$$

where x_o is the oxide thickness at time t, B is the parabolic rate constant, B/A is the linear rate constant and τ corresponds to a shift in the time coordinate correcting for the presence of an existing oxide of thickness x_i.[40] However, this analysis does not result in a linear plot of x_o vs t/x_o for any of the deposition conditions studied here. Thus, there is not

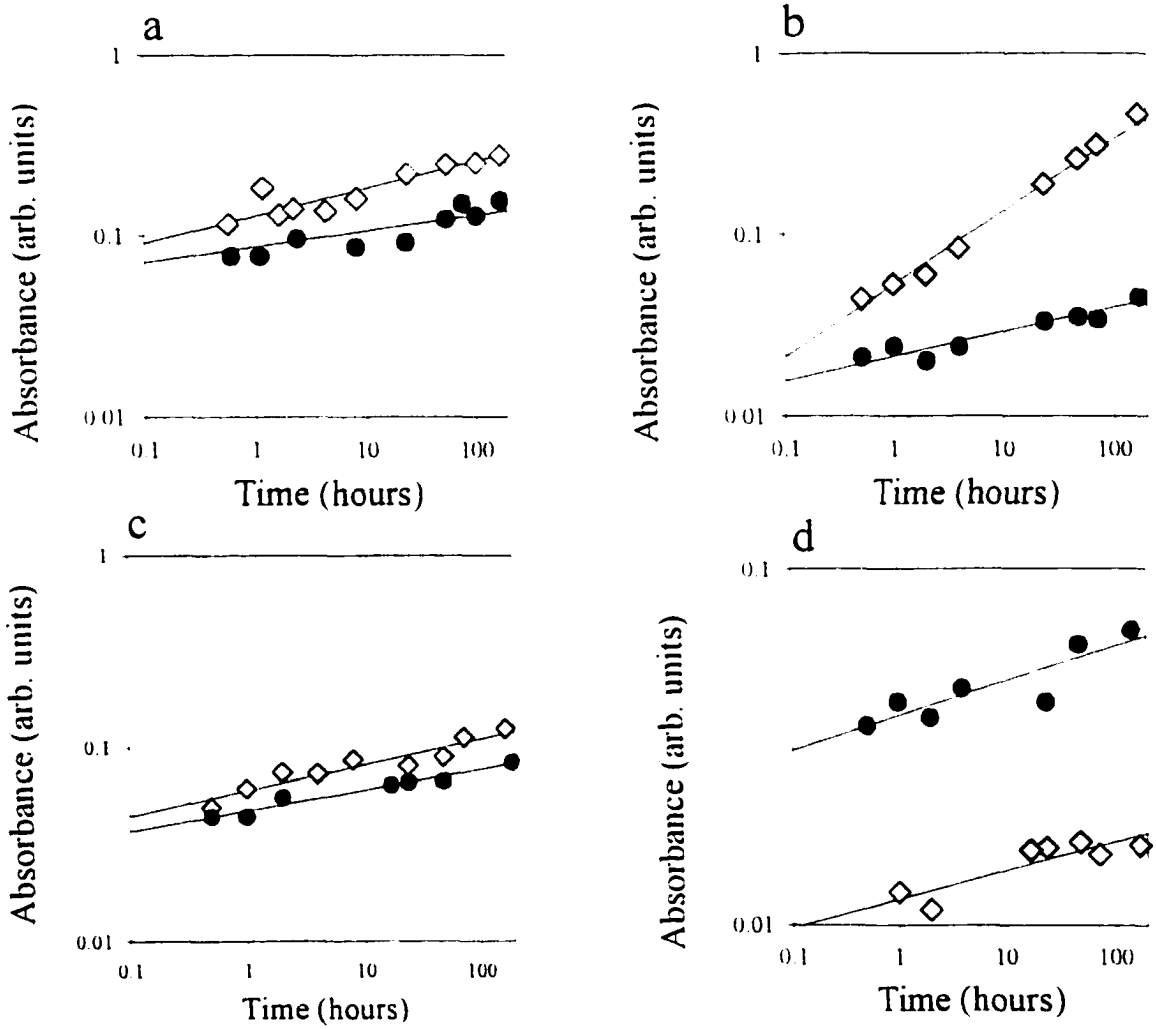

Figure 7.5. Oxide absorbance as a function of time for the oxidation of a-$Si_{1-x}C_x$:H films from pulsed (solid circles) and CW (open diamonds) plasmas with (a) no dilution gas; (b) He as the diluent gas; (c) Ar as the diluent gas; and (d) H_2 as the diluent gas. Lines represent linear least squares regression analysis fits to the data.

a simple parabolic or linear-parabolic relationship that can explain the kinetic behavior for the oxidation of our a-$Si_{1-x}C_x$:H films.

In general, Eldridge and coworkers observed that the reactivity of a-$Si_{1-x}C_x$:H films with oxygen increases with both hydrogen and carbon concentrations, and decreases with Si content in the film.[16] As noted in the section 7.1, much of this is attributable to the preference for formation of C-H bonds over Si-H bonds in these films.[16] Higher concentrations of CH_3 moieties in the films also leads to greater oxidation.[17] The microvoids associated with these structural features assist the inward transport of the oxidizing species to Si-Si bonds where the insertion of an oxygen atom is likely to happen. The oxidation of a-$Si_{1-x}C_x$:H is also complicated by the formation of CO and/or CO_2, and possibly H_2O.[16,41] Production of these species decreases the amount of oxygen available for formation of Si-O-Si groups and, by diffusing through the oxide layer, they may affect the structure of the film. Thus, the outward diffusion of these species introduces another candidate for the rate-limiting step in the oxidation process.

Another compositional feature of our a-$Si_{1-x}C_x$:H films arises from examining the Si-H bonding. The Si-H stretching frequency (~2100 cm^{-1}) in the film deposited from a SiH_4/CH_4 CW plasma, Fig. 7.1, occurs at a higher frequency upon oxidation (a shift of ~26 cm^{-1}); the same peak does not shift with oxidation in the pulsed plasma system. The intensity of the Si-H stretching frequency also decreases with oxidation. As noted above, this is likely the result of Si-O bonds replacing the Si-H bonds in the films, or simply a loss of hydrogen through the formation of H_2O as an oxidation product.[16] Koropecki et al. have studied the Si-H stretching band in the IR spectra of a-$Si_{1-x}C_x$:H films with varying

amounts of carbon incorporation.[39] They find that the Si-H stretching frequency shifts to the blue in films with higher carbon content ($x \geq 0.4$) during oxidation. Moreover, they conclude that the increase in the number of voids induced by the presence of carbon in the films is the most influential parameter affecting the shift of the Si-H stretching band. This is corroborated by the work of Lin et al. who found a similar correlation with films having a higher fraction of carbon content.[40] This suggests that our CW a-$Si_{1-x}C_x$:H films (with no dilution gas) have a high fraction of carbon, with $x \geq 0.4$, which is verified by the XPS analysis in Table 7.2.

In contrast, the Si-H stretching frequency does not shift in frequency or decrease in intensity with oxidation for films deposited from the pulsed plasmas, Fig. 7.2. Furthermore, the amount of hydrogen incorporation in the pulsed films is decreased overall, as evidenced by the absence of SiH/SiH_2 bending modes at 685, 840, and 890 cm^{-1} and by the decrease in CH_3 stretching modes (~2900 cm^{-1}). The pulsed films thus have a lower fraction of $-CH_3$ incorporation and thereby a lower concentration of microvoids, leading to an overall lower rate of oxidation. Similarly, Tabata et al. found the addition of H_2 to their CW silane/methane plasmas resulted in films with more carbon atoms with fourfold coordination (diamond-like) than with threefold coordination (graphite-like).[41] This suggests the a-$Si_{1-x}C_x$:H films produced in our pulsed plasma systems are more robust and may have better electrical and mechanical properties. Further characterization of a-$Si_{1-x}C_x$:H films produced in pulsed plasmas is given in chapter 8.

7.4. CONCLUSIONS

Relative oxidation rates have been measured for a-$Si_{1-x}C_x$:H films deposited from CW and equivalently powered pulsed rf plasmas using mixtures of SiH_4/CH_4 and diluent gases He, Ar, and H_2. Under most conditions, the CW films oxidize much more rapidly than their pulsed plasma counterparts. With H_2 dilution, the CW films do not oxidize appreciably upon exposure to atmosphere. This is likely the result of hydrogen radicals annealing the surface of the depositing film. A more detailed understanding of the structural, mechanical, and electrical properties of a-$Si_{1-x}C_x$:H films deposited from both pulsed and CW plasmas is vital to the further application of these potentially useful materials.

REFERENCES

1. D. A. Anderson and W. E. Spear Philos. Mag. **35**, 1 (1977).

2. W. K. Choi, Y. M. Chan, C. H. Ling, Y. Lee, R. Gopalakrishnan, and K. L. Tan, J. Appl. Phys. 77, 827 (1995).

3. Y. Catherine and A. Zamouche, Thin Solid Films **109**, 145 (1983).

4. A. H. Mahan, P. Raboisson, D. L. Williamson, and R. Tsu, Solar Cells **21**, 117 (1987).

5. A. Sproul, D. R. McKenzie, and D. J. H. Cockayne, Philos. Mag. *B* **54**, 113 (1986).

6. F. Demichelis, G. Crovini, C. F. Pirri, E. Tresso, G. Amato, U. Coscia, G. Ambrosone, and P. Rava, Thin Solid Films **241**, 274 (1994); M. A. El Khakani, M. Chaker, A. Jean, S. Boily, H. Pepin, J. C. Kieffer, and S. C. Gujrathi, J. Appl. Phys. **74**, 2834 (1993); D. Girginoudi and A. Thanailakis, J. Appl. Phys. **69**, 1490 (1991).

7. R. L. Kostelak, T. W. Weidman, S. Vaidya, O. Joubert, S. C. Palmeteer, and M. Hibbs, J. Vac. Sci. Technol. B **13**, 2994 (1995).

8. G. Leo, G. Galluzzi, G. Guattari, R. Vincenzoni, F. Demichelis, G. Crovin, C. F. Pirri, and E. Tresso, J. Non-Cryst. Solids **164-166**, 1035 (1993).

9. D. Kuhman, S. Grammatica, and F. Jansen, Thin Solid Films **177**, 253 (1989).

10. M. L. de Oliveira and S. S. Camargo, Jr., J. Appl. Phys. **71**, 1531 (1992).

11. W. A. Nevin, H. Yamagishi, and Y. Tawada, J. Appl. Phys. **72**, 4989 (1992).

12. G. DellaMea, F. Demichelis, C. F. Pirri, P. Rava, V. Rigato, T. Stapinski, and E. Tresso, J. Non-Cryst. Solids **137/138**, 95 (1991).

13. P. J. R. Honeybone, J. K. Walters, D. W. Huxley, R. J. Newport, W. S. Howells, J. Tomkinson, and C. Hotham, J. Non-Cryst. Solids **169**, 54 (1994).

14. A. H. Mahan, D. L. Williamson, B. P. Nelson, and R. S. Crandall, Solar Cells **27**, 465 (1989).

15. W. Beyer, J. Non-Cryst. Solids **97/98** 1027 (1987).

16. J. M. Eldridge, J. O. Moore, G. Olive, and V. Dunton, J. Electrochem. Soc. **137**, 2266 (1990).

17. F. Ibrahim, J. I. B. Wilson, and P. John, J. Non-Cryst. Solids **164-166**, 1051 (1993).

18. P. John, A. Qayyum, and J. I. B. Wilson, Electronics Lett. **25**, 930 (1989).

19. D. Alok and B. J. Baliga, J. Electrochem. Soc. **144**, 1135 (1997).

20. J. Kodama, S. Araki, M. Kimura, and T. Inagaki, Jpn. J. Appl. Phys. **29**, L867 (1990).

21. N. M. Mackie, N. F. Dalleska, D. G. Castner, and E. R. Fisher, Chem. Mater. **9**, 349 (1997).

22. N. M. Mackie and E. R. Fisher, Polym. Prepr. **38**, 1059 (1997). N. M. Mackie, D. G. Castner, and E. R. Fisher, Langmuir **14**, 1227 (1998).

23. M. A. Leich, N. M. Mackie, and E. R. Fisher, Macromolecules, **31**, 7618 (1998).

24. A. E. Lefohn, N. M. Mackie, and E. R. Fisher, Plasmas Polym., accepted for publication.

25. V. Panchalingam, X. Chen, C. R. Savage, R. B. Timmons, and R. C. Eberhart, J. Appl. Polym. Sci. Polym. Symp. **54**, 123 (1994).

26. R. Zedlitz, E. Lotter, and M. Heintze, J. Non-Cryst. Solids **164-166**, 1031 (1993); S. Ray, D. Das, A. K. Barua, Solar Energ. Mater. **15**, 45 (1987).

27. J. L. C. Fonseca, D. C. Apperley, and J. P. S. Badyal,Chem. Mater. **5**, 1676 (1993).

28. H. Wieder, M. Cardona, and C. R. Guarnieri, Phys. Stat. Sol. **92**, 99 (1979).

29. The presence of C atoms attached to Si has been shown to greatly enhance the oscillator strength of Si-H vibrations and that the oscillator strength of the C-H stretching band decreases as the number of Si atoms attached to the carbon increases.[31] No corrections for these changes in oscillator strengths were made.

30. X. Chen, K. Rajeshwar, R. B. Timmons, J.-J. Chen, and O. M. R. Chyan, Chem. Mater. **8**, 1067 (1996).

31. C. R. Savage, R. B. Timmons, and J. W. Lin, *Structure-Property Relations in Polymers, Advances in Chemistry Series*, **236**: Washington D. C., 1993; p. 745.

32. A. Grill, *Cold Plasma In Materials Fabrication: From Fundamentals to Applications*, IEEE Press, New York (1994).

33. K. Yasui, M. Muramoto, and T. Akahane, Jpn. J. Appl. Phys. **33**, 4395 (1994).

34. O. Matsumoto and T. Katagiri, Thin Solid Films **146**, 283 (1987); P. Barbarat, C. Accary, and W. L. Hase, J. Phys. Chem. **97**, 11706 (1993); L. N. Krasnoperov, I. J. Kalinovski, H.-N. Chu, and D. Gutman, J. Phys. Chem. **97**, 11787 (1993).

35. T. Friessnegg, M. Boudreau, J. Brown, P. Mascher, P. J. Simpson, and W. Puff, J. Appl. Phys. **80**, 2216 (1996).

36. R. Arce, R. R. Koropecki, R. H. Buitrago, F. Alvarez, and I. Chambouleyron, J. Appl. Phys. **66**, 4544 (1989).

37. B. E. Deal and A. S. Grove, J. Appl. Phys. **36**, 3770 (1965).

38. J. A. Costello and R. E. Tressler, J. Am. Ceram. Soc. **69**, 674 (1986).

39. R. R. Koropecki, F. Alvarez, and R. Arce, J. Appl. Phys. **69**, 7805 (1991).

40. W.-L. Lin, H.-K. Tsai, S.-C. Lee, W.-J. Sah, and W.-J. Tzeng, Appl. Phys. Lett. **51**, 2112 (1987).

41. A. Tabata, S. Fujii, Y. Suzuoki, T. Mizutani, and M. Ieda, J. Phys. D: Appl Phys. **23**, 316 (1990).

CHAPTER 8

PULSED AND CONTINUOUS WAVE PLASMA DEPOSITION OF AMORPHOUS, HYDROGENATED SILICON CARBIDE FROM SiH_4/CH_4 PLASMAS

8.1 INTRODUCTION

As mentioned in Chapter 7 there is a lack of understanding of both the chemical structure of a-$Si_{1-x}C_x$:H and the how the structure affects its physical and electrical properties. In addition to issues surrounding the chemical structure, the mechanism for plasma deposition from both continuous wave (CW) and pulsed systems is not well understood. Pulsing the plasma adds another dimension of control to the properties of film deposition, but also increases the complexity of the system. Indeed, pulsed plasmas have been shown to deposit very different films than their CW counterparts,[1] and have been successfully employed in the plasma polymerization of a variety of organic monomers.[2,3] With pulsed plasma polymerization, high retention of the monomer functional group in the resulting film can be achieved.[1,4] This is in marked contrast to most films formed in CW plasma depositions, where materials are generally amorphous with little structural resemblance to that of the original monomer.[1,5,6] Pulsed plasmas also reduce trapped radicals in the film, lower substrate temperatures, and in general, decrease ion bombardment and UV flux to the growing film.[7]

While there is a growing body of work using pulsed plasmas to deposit organic

polymer films, little work has been done using pulsed plasmas to deposit inorganic materials. One study investigated pulsed plasma deposition of TiN films from $TiCl_4$, N_2, and H_2 using a parallel plate reactor.[8] Films deposited in this pulsed plasma system showed low Cl contamination, evan at low substrate temperatures. The amount of Cl was also reduced with high rf peak powers, low duty cycles, and by supplying $TiCl_4$ to the feed only during every other pulse cycle. The importance of a high peak power was attributed to increased fragmentation of $TiCl_4$ and increased concentration of reactive hydrogen. The low duty cycle allowed hydrogen to react with $TiCl_x(g)$ (x = 1-4) to form $TiCl_{x-1}(g)$, thus reducing chlorine contamination in the Ti precursor for the deposited film.

Only two studies have investigated the use of pulsed plasmas for deposition of a-$Si_{1-x}C_x$:H films. Panchalingham et al.[7] deposited a-$Si_{1-x}C_x$:H in a pulsed, capacitively-coupled plasma using vinyltrimethylsilane as the precursor. In this work, it was shown that the Si-CH_3/Si-H absorbance ratio decreased progressively as the off time was increased (duty cycle decreased). In addition, film deposition rates increased significantly as the off time was increased. In Chapter 7 we examined the oxidation rates of a-$Si_{1-x}C_x$:H films deposited from SiH_4/CH_4 plasmas and found that films deposited in pulsed plasmas had significantly reduced oxidation rates. When H_2 was added to the feed, oxidation rates were reduced for films deposited in both pulsed and CW plasmas. In the present work, we continue to examine the effects of pulsed parameters on the properties of a-$Si_{1-x}C_x$:H films deposited from SiH_4/CH_4 plasmas. Here we report on the effect of pulse parameters on film composition, the bonding environment in the film, and deposition rates. The effect of hydrogen dilution in these systems is also investigated. Additionally, the effect of ions in

the deposition process is investigated by biasing the substrate and by ion deflection.

8.2. RESULTS

8.2.1. FOURIER TRANSFORM INFRARED SPECTROSCOPY

Table 8.1 lists the FTIR absorption bands we observe for our a-$Si_{1-x}C_x$:H films, along with assignments we have adopted and their literature references. It should be noted that there is some ambiguity in the literature about the assignment of the various absorption peaks for a-$Si_{1-x}C_x$:H films.[9] The major complication is that, unlike crystalline materials, a-$Si_{1-x}C_x$:H films are not well- defined bulk materials and their properties depend strongly on the deposition conditions, making comparison between different studies difficult.

8.2.1.1. PULSED vs CW PLASMA DEPOSITED FILMS

Figure 8.1 shows the FTIR spectra of films deposited from CW and pulsed SiH_4/CH_4 plasmas are very different. First, the pulsed plasma deposited film has a simpler spectra with fewer absorbance peaks than the spectrum of the film produced in the CW plasma. All of the additional peaks in the spectrum of the CW plasma deposited film are associated with SiH_x bending modes. Specifically, the spectrum for this film shows SiH_2 bending modes at ~870 cm^{-1} and ~930 cm^{-1},[10] and Si-H bending at ~680 cm^{-1}.[11,12] The most prominent absorbance in both spectra is the Si-C stretch at ~780 cm^{-1}.[13,14] In the pulsed system, this absorbance is more pronounced and broader than in the CW plasma deposited film. The SiH stretching absorbance band at 2100 cm^{-1} is present in all spectra,[15] but is more intense in the CW films, Fig. 8.1.

Table 8.1. Absorbance Band Assignments for a-$Si_{1-x}C_x$:H Films

Absorbance cm^{-1}	Assignment	Reference
630-670	SiH_x wagging or rocking	13, 11, 12
750-850	Si-C stretching	13, 14
870, 930	SiH_2 bending	10
1000-1100	Si-O-Si asymmetrical stretching	15, 17
	Si-CH_2-Si wagging	18
1248-1250	Si-CH_3 wagging	15, 18
1350	methyl symmetrical bending in CH_3-C	18
1405	CH_2 symmetrical scissoring in Si-CH_2	18
1455	methyl symmetrical bending in CH_3-C	18
~2100	Si-H stretching	13, 14, 15, 18
2800-3000	C-H_n stretching	13, 14, 15

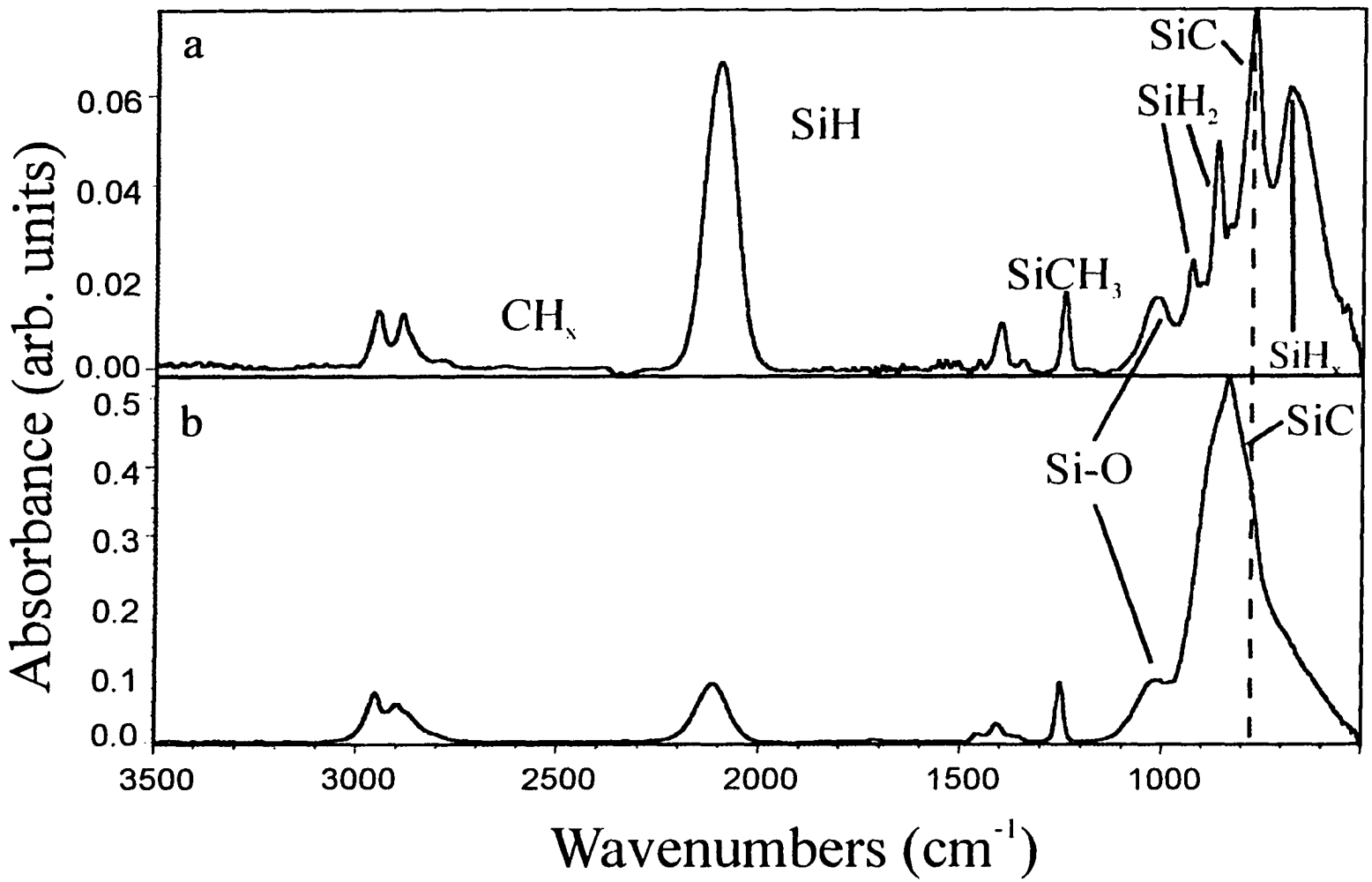

Figure 7.1. FTIR transmission spectra for an a-$Si_{1-x}C_x$:H film deposited from a 5 W CW SiH_4/CH_4 plasma: (a) immediately after deposition and (b) 5 days after deposition. The line indicates the the peak of the initial Si-H stretching frequency at 2105 cm^{-1}. A shift of 26 cm^{-1} is observed during oxidation.

8.2.1.2. DUTY CYCLE DEPENDENCE

To investigate the effect of varying pulsed plasma parameters on the bonding environment of the deposited a-$Si_{1-x}C_x$:H film the duty cycle was varied from 1-20% at equivalent powers. Figure 8.2 shows FTIR spectra of two films deposited on grounded substrates from equivalently-powered pulsed plasmas with duty cycles of 7% and 8%. Even though the duty cycle was only changed by 1% and peak pulse power (P) changed by only 9 W (72 W to 63 W), very different films were produced. The spectrum of the film deposited at the lower peak power (63 W) shows all of the SiH_x bending absorbances. These peaks are either not present or have been reduced to indistinguishable shoulders in the spectrum of the film formed at P = 72 W. Also in this spectrum, the relative intensity of the Si-C stretch at ~780 cm^{-1} is much greater than that for the film deposited at P = 63 W.

The spectra of all films deposited in equivalently-powered pulsed plasmas with P < 63 W were similar to that observed for films deposited at P = 5 W CW. Spectra of films deposited with P > 72 W were all similar, but some differences were observed. These include a gradual decrease in the intensity of the Si-CH_3 bending mode (1250 cm^{-1}), the CH_3 antisymmetric stretch (2955 cm^{-1}), and the Si-O/Si-CH_2-Si peak (1030 cm^{-1}),[16,17] and a broadening of the Si-C stretch at 780 cm^{-1} as the peak power increased.

8.2.1.3. SUBSTRATE GROUNDING EFFECTS

Initial FTIR spectra of films deposited from CW plasmas on grounded Si substrates are indistinguishable from those of films deposited on ungrounded substrates, Fig. 8.1a. Differences in the two films become apparent, however, in the spectra of aged

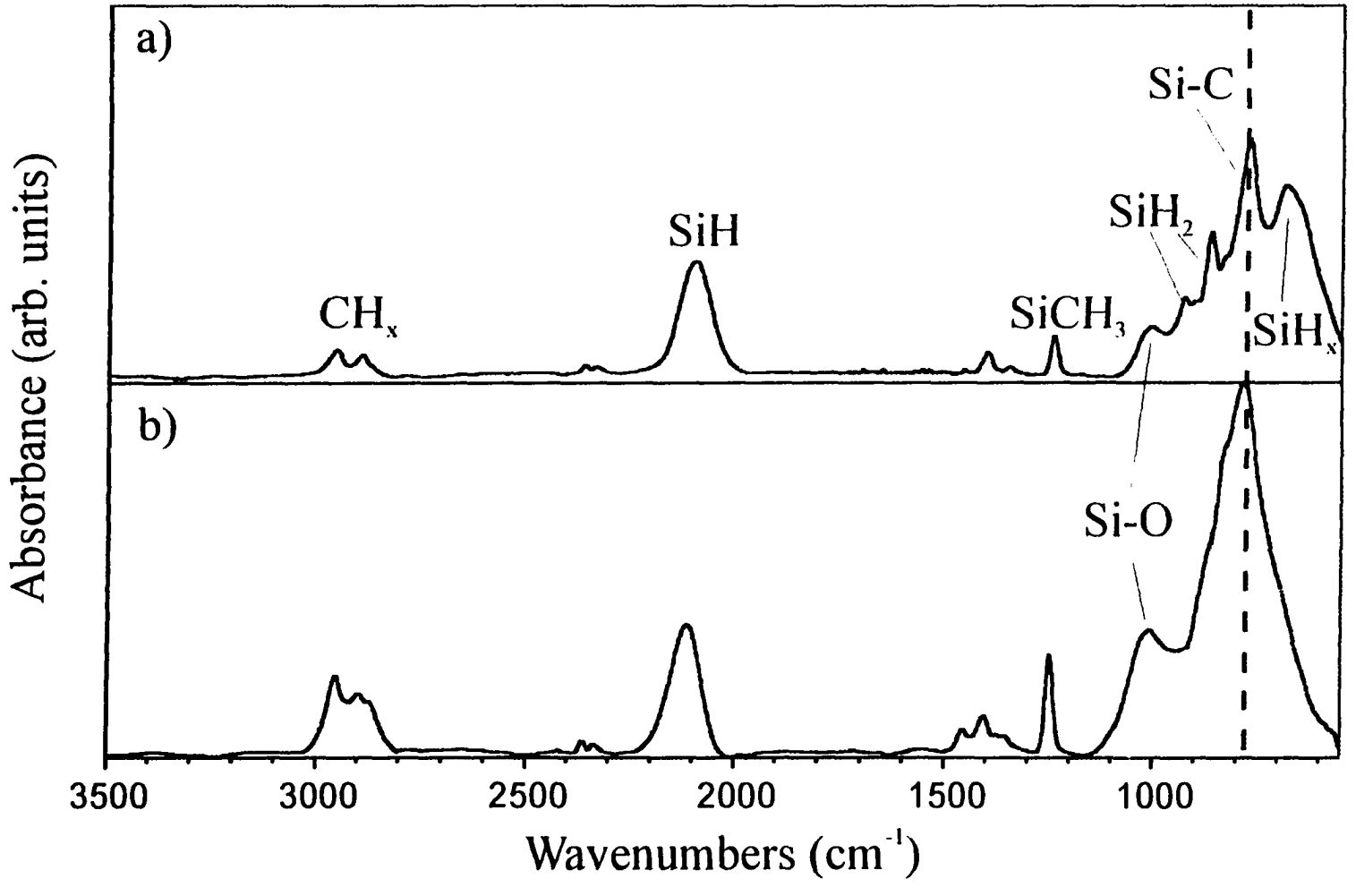

Figure 8.2. FTIR transmission spectra of a-$Si_{1-x}C_x$:H films deposited from equivalently powered pulsed plasmas: (a) 63 W with an 8 % duty cycle and (b) 72 W with a 7 % duty cycle.

films. Two FTIR spectra of CW plasma deposited films taken 24 hours after deposition are shown in Fig. 8.3. The Si-O absorbance peak at 1030 cm^{-1} has increased significantly for the ungrounded film while that for the grounded film increased only slightly. In contrast, grounding the substrate in the pulsed plasma has a significant effect on film composition, Fig. 8.4. The most notable difference between these spectra is the shift in the peak of the Si-C stretching absorbance from 837 cm^{-1} (ungrounded) to its normal position at 780 cm^{-1} (grounded). In addition, in the ungrounded substrate system, the Si-CH_3 bend is significantly larger relative to the Si-C stretch, and there is a pronounced CH_3 antisymmetric stretch at 2955 cm^{-1} This indicates a high level of methyl group incorporation in this film. In the grounded substrate system, the CH_x stretching absorbance peaks coalesce into one broad band, indicating greater fragmentation of the CH_x groups in the film. In addition, we observe only a slight increase of the Si-O-Si bridging mode at 1030 cm^{-1} of the a-$Si_{1-x}C_x$:H deposited on the grounded substrate in a pulsed plasma over a period of > 8 months. In contrast, a significant amount of oxidation occurred with ungrounded films deposited under otherwise identical conditions, Chapter 7.

8.2.1.4. ION BOMBARDMENT EFFECTS

To further investigate the effects of ion bombardment, silicon substrates were biased at both positive and negative voltages (±1 kV).[18] No significant changes in the IR spectra were noted between the biased substrates and their grounded counterparts for films deposited in both CW and pulsed plasmas. Oxidation rates were nearly identical for films deposited in both CW and pulsed plasmas, regardless of the bias of the substrate

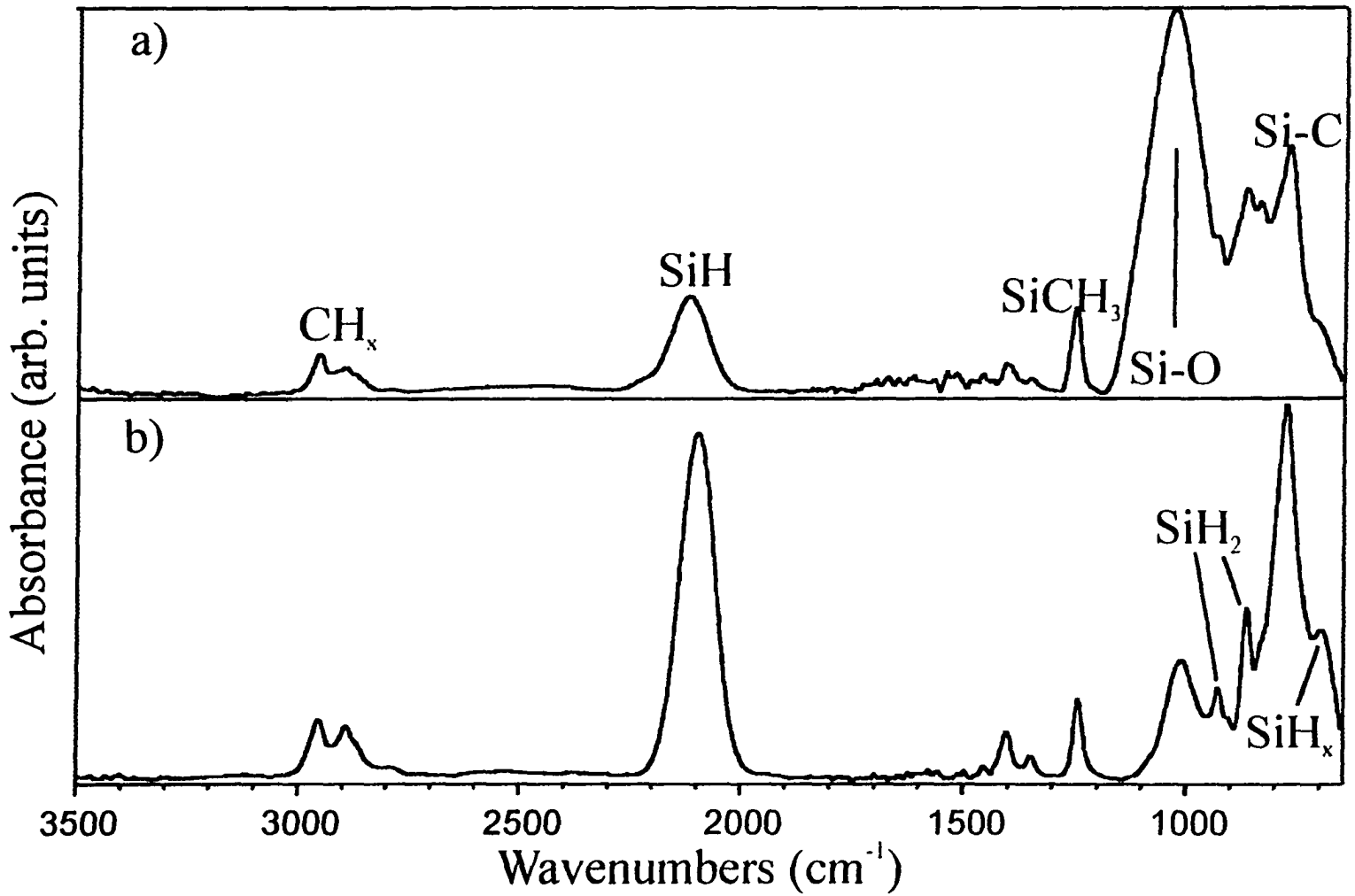

Figure 8.3. FTIR transmission spectra of a-$Si_{1-x}C_x$:H films 24 hours after deposition from 5 W, CW plasmas on (a) an ungrounded Si substrate and on (b) a grounded Si substrate.(positive, negative, or grounded).

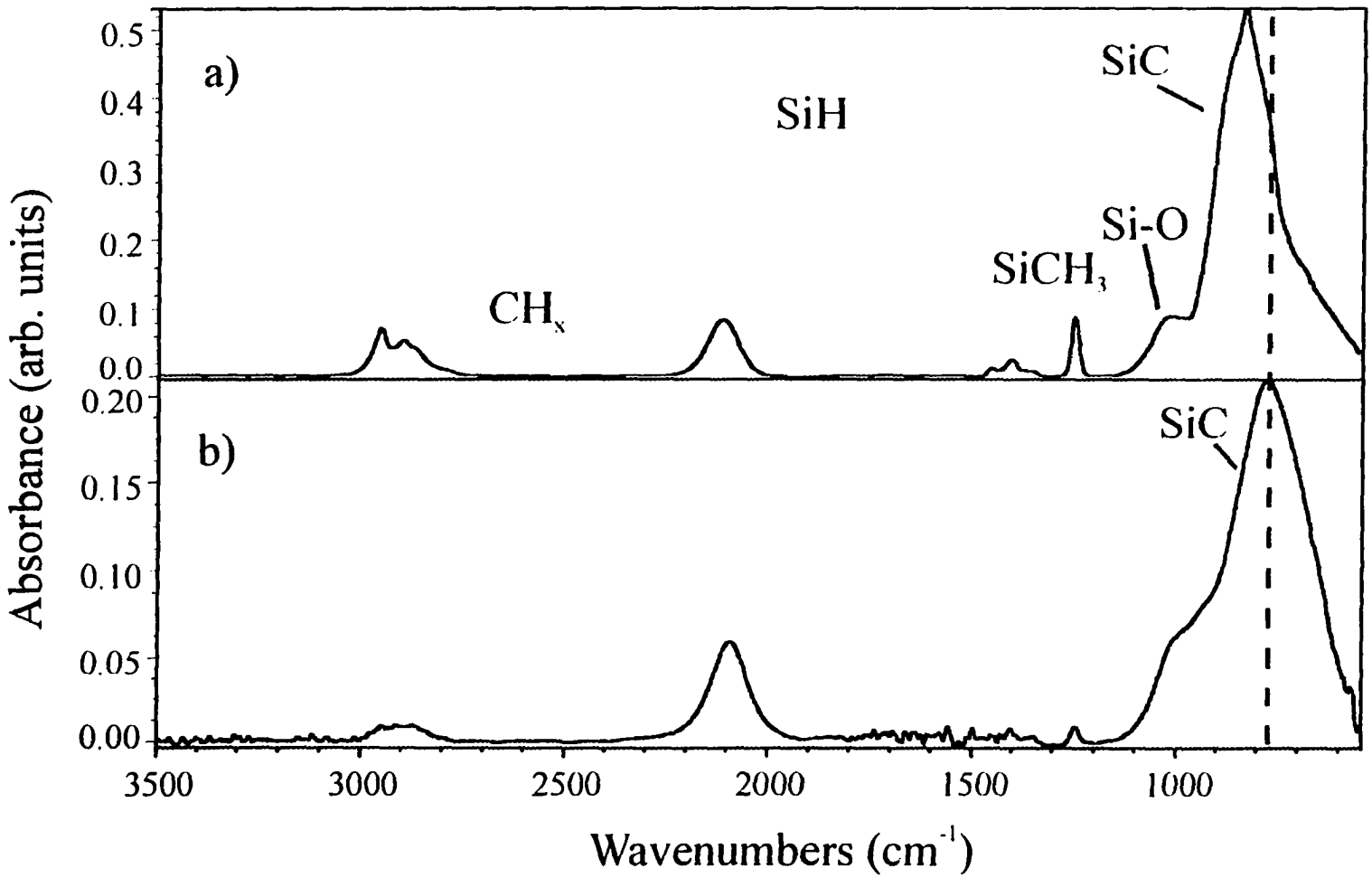

Figure 8.4. FTIR transmission spectra of a-$Si_{1-x}C_x$:H deposited film from pulsed plasmas on a) an ungrounded Si substrate and on b) a grounded Si substrate. The dashed line is the "normal" position of the Si-C in a-$Si_{1-x}C_x$:H films at 780 cm^{-1}.

(positive, negative, or grounded).

In separate experiments, biased deflector plates were inserted into the plasma chamber to minimize the number of charged particles bombarding the ungrounded Si substrate. The FTIR spectra of films deposited with charged deflector plates (±200 V) in CW plasmas look nearly identical to those of other CW plasma depositions.[19] Also, the oxidation rate of these films was similar to that for films deposited on ungrounded substrates without deflector plates.

In contrast, significant differences in film composition were observed for films deposited in pulsed plasmas with the deflector plates. Figure 8.5a shows the FTIR spectrum of a film deposited with a -200 V bias across the deflector plates. Note the similarities between Fig. 8.5a and the spectrum in Fig. 8.1a. The SiH_x bending modes, absent in spectra of pulsed plasma deposited films without deflector plates, are distinct in this spectra. Spectra of films deposited with +200 V bias, as well as unbiased but grounded deflector plates were similar to those with the -200 V bias. If ungrounded plates were allowed to self-bias, the FTIR spectra of deposited films were similar to those for ungrounded pulsed depositions, Fig 8.1b. Films deposited with the deflector plates biased or grounded, however, oxidized more rapidly than films formed without the deflector plates in pulsed plasmas, Fig. 8.5b.

8.2.1.5. EFFECT OF H_2 DILUTION

FTIR spectra of films deposited from CW and pulsed plasmas on grounded substrates with H_2 added to the gas flow are shown in Fig. 8.6. Little change is seen in the spectrum of the CW plasma deposition upon H_2 dilution, suggesting this does not

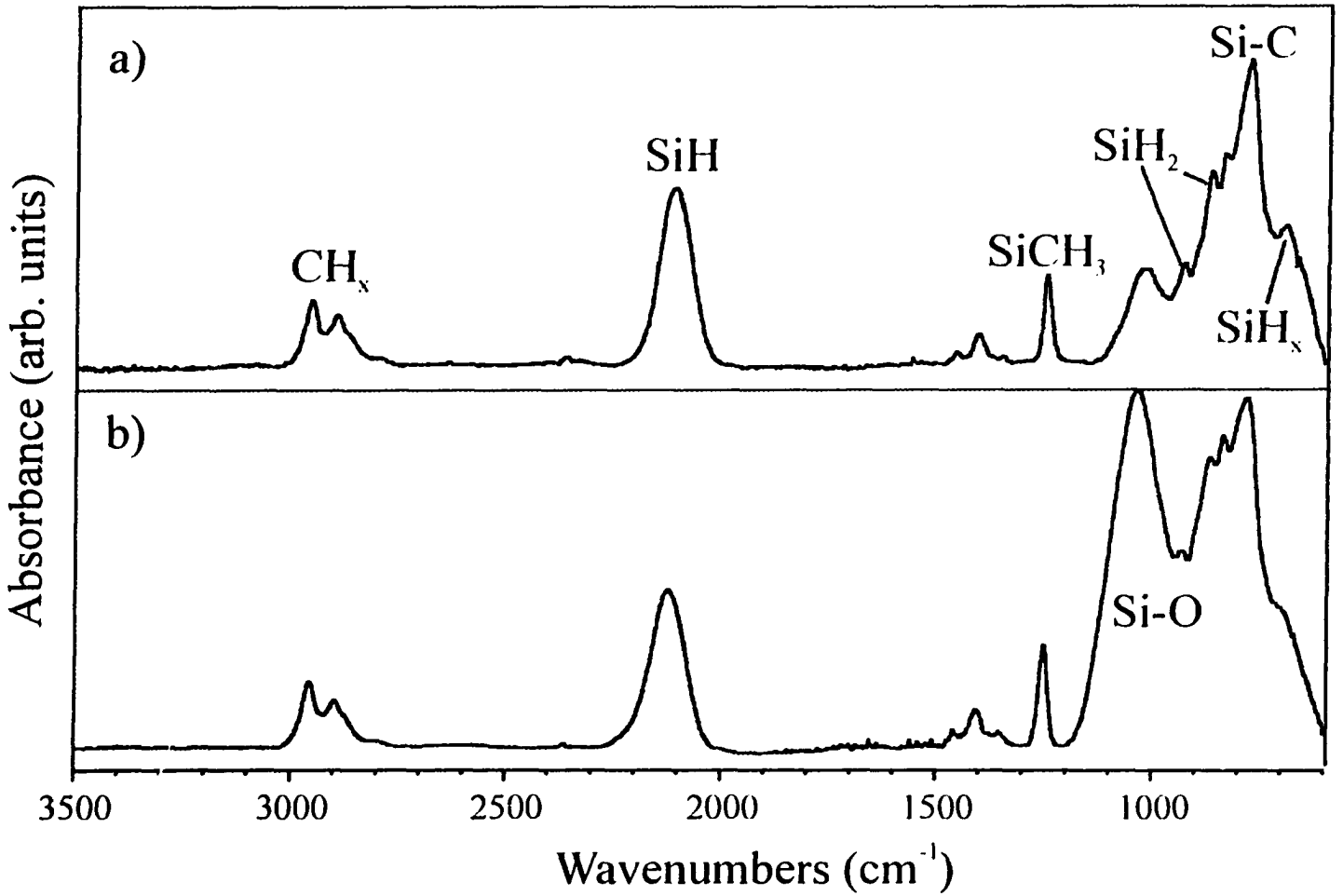

Figure 8.5. FTIR transmission spectra of a-$Si_{1-x}C_x$:H deposited film from a pulsed plasma (P = 500 W, 1 % duty cycle) with deflector plates biased at -200 V on an ungrounded Si substrate. Spectra shown were taken a) 5 minutes after deposition and b) 3 days after deposition.

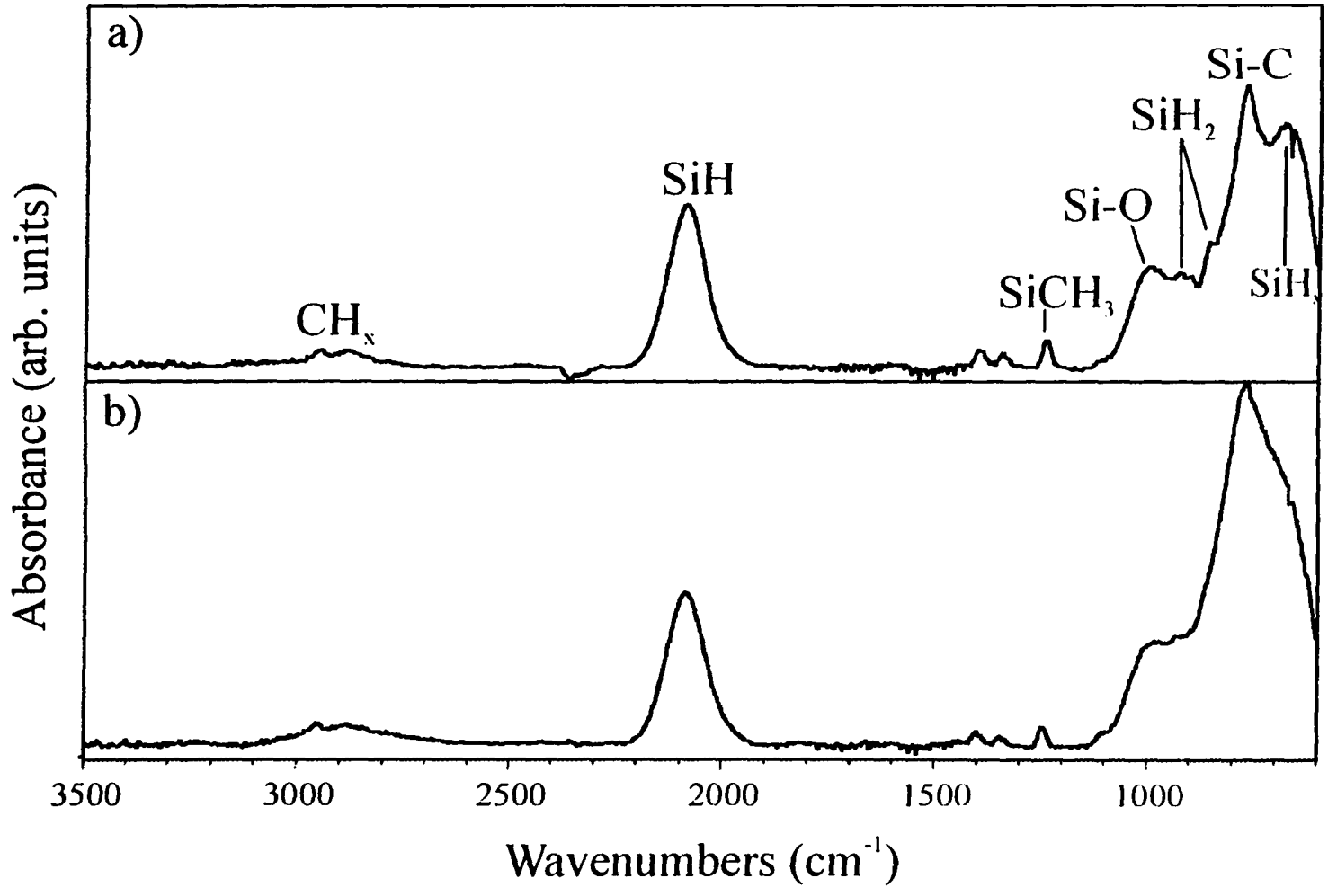

Figure 8.6. FTIR transmission spectra of a-$Si_{1-x}C_x$:H films deposited from $SiH_4/CH_4/H_2$ plasmas with (a) CW plasma (P = 5 W) and (b) a pulsed plasma (P = 500 W, 1% duty cycle).

significantly alter film composition under these conditions. The spectrum of the film from the pulsed plasma, however, shows a significant increase in the amount of SiH stretching (~2100 cm^{-1}), and a corresponding increase in the SiH_x bending mode at 670 cm^{-1}, Fig. 8.6b, relative to spectra of films formed under similar conditions without H_2 dilution, Fig. 8.1b and 8.4b. In Chapter 7, we reported that H_2 dilution lowered the oxidation rate of the films deposited on ungrounded substrates. Grounding the substrate reduces the oxidation rate even further. For CW plasma depositions with grounded substrates and H_2 dilution, the change in the Si-O/Si-C peak ratio after 150 days was only Δ=0.20 compared to Δ=0.90 on ungrounded substrates.

8.2.2. DEPOSITION RATES IN PULSED PLASMA SYSTEMS

Film deposition rates for both CW and pulsed systems have been given in Chapter 7. It was generally found that deposition rates for the pulsed systems were consistently higher than for the CW systems by 200-400 Å/min. This suggests significant deposition occurs during both the on and off times of the pulse cycle. Here, we further explore the effects of off time and total cycle time on film deposition rates in the SiH_4/CH_4 pulsed plasma.

8.2.2.1. OFF TIME DEPENDENCE

Pulse off time is an important parameter in determining film deposition rates as well as film composition for pulsed plasma polymerization systems.[1-4] Figure 8.7 shows the relationship between off-time and film deposition rate in SiH_4/CH_4 plasmas. The deposition rate per pulse initially increases as off time is increased, but at extended

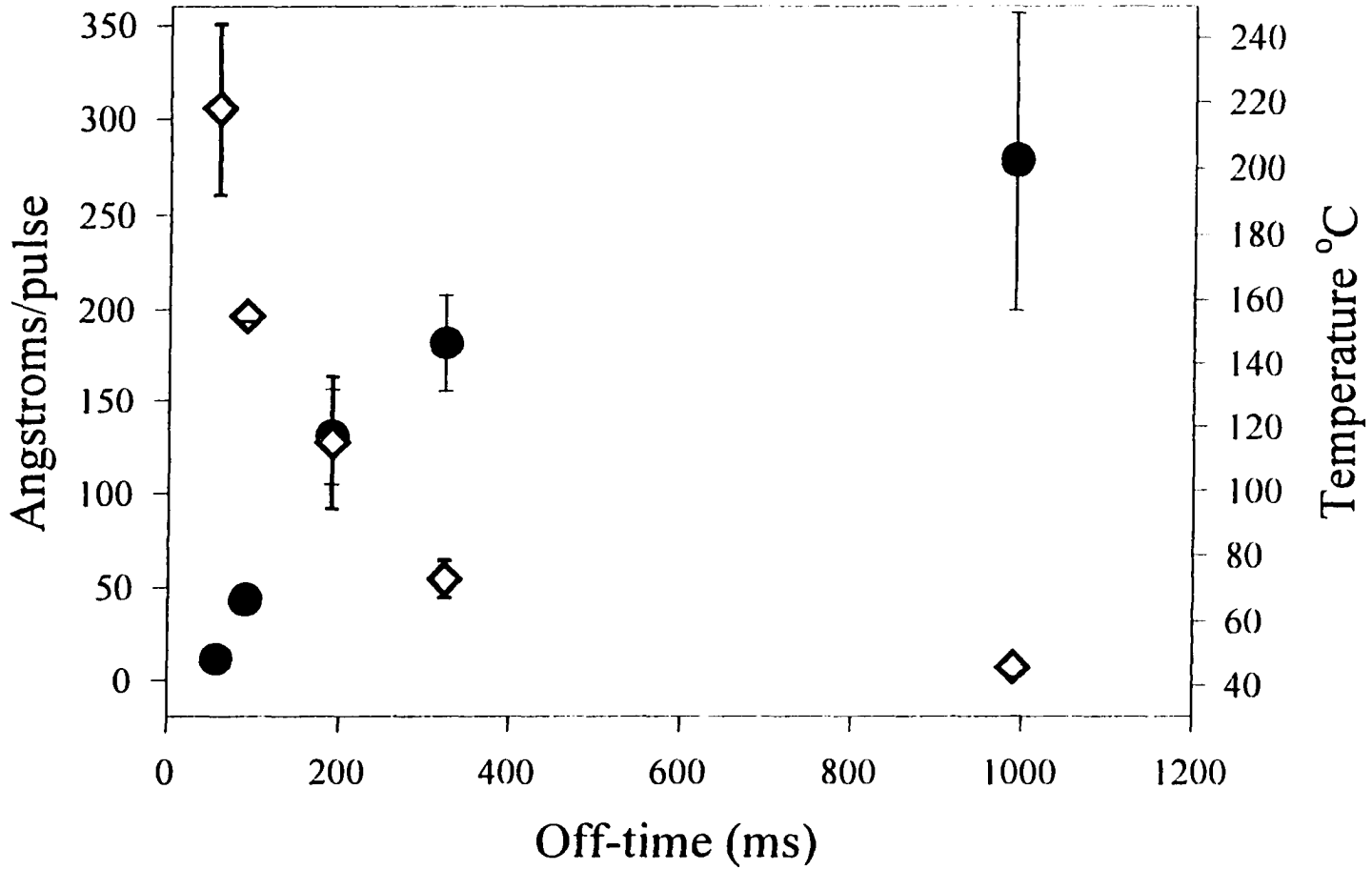

Figure 8.7. Deposition rate per pulse as a function off time, (closed circles, left y-axis). Final substrate temperature as a function of off time after 15 min. depositions, (open diamonds, right y-axis). All depositions were performed using 500 W pulsed plasmas with 10 ms on times.

off-times levels off at ~300 Å/pulse. Figure 8.7 also shows the final T_S as a function of pulse off time. From these data, there appears to be an inverse relationship between deposition rate and T_S.

8.2.2.2. CYCLE-TIME DEPENDENCE

As seen in Fig. 8.7 and previous studies,[20] variations in T_S can often contribute to film chemistry and deposition rate changes. To minimize this, the cycle time was varied while holding the duty cycle constant at 1% with P = 500 W. All depositions, therefore, had equivalent applied rf powers of 5 W with cycle times from 200 to 1600 ms. T_S measurements confirmed equivalent heating, with all depositions having a final T_S = 41 ± 1 °C. Figure 8.8 shows the deposition rate (Fig. 8.8a) and the deposition rate *per pulse* (Fig. 8.8b) as a function of cycle time in SiH_4/CH_4 plasmas. In these experiments, all a-$Si_{1-x}C_x$:H films had FTIR spectra similar to that shown in Fig. 8.4b. Clearly a linear relationship exists between both the cycle time, and deposition rate per pulse. Linear regression analysis of the data in Fig. 8.8b yields b = 1.40 Å/pulse, with m = 4.10 Å s^{-1} per cycle. Since the duty cycle is 1%, this implies the deposition rate is 410 Å s^{-1} during the on time.

8.2.3. X-RAY PHOTOELECTRON SPECTROSCOPY

XPS analyses were performed on a-$Si_{1-x}C_x$:H films deposited on Si substrates from pulsed and CW plasmas ~4 days after the films were deposited. Surface elemental compositions for these films are listed in Table 8.2. For all samples only Si, C, and O were detected at levels above 1%. Grounding the substrate showed almost no effect on

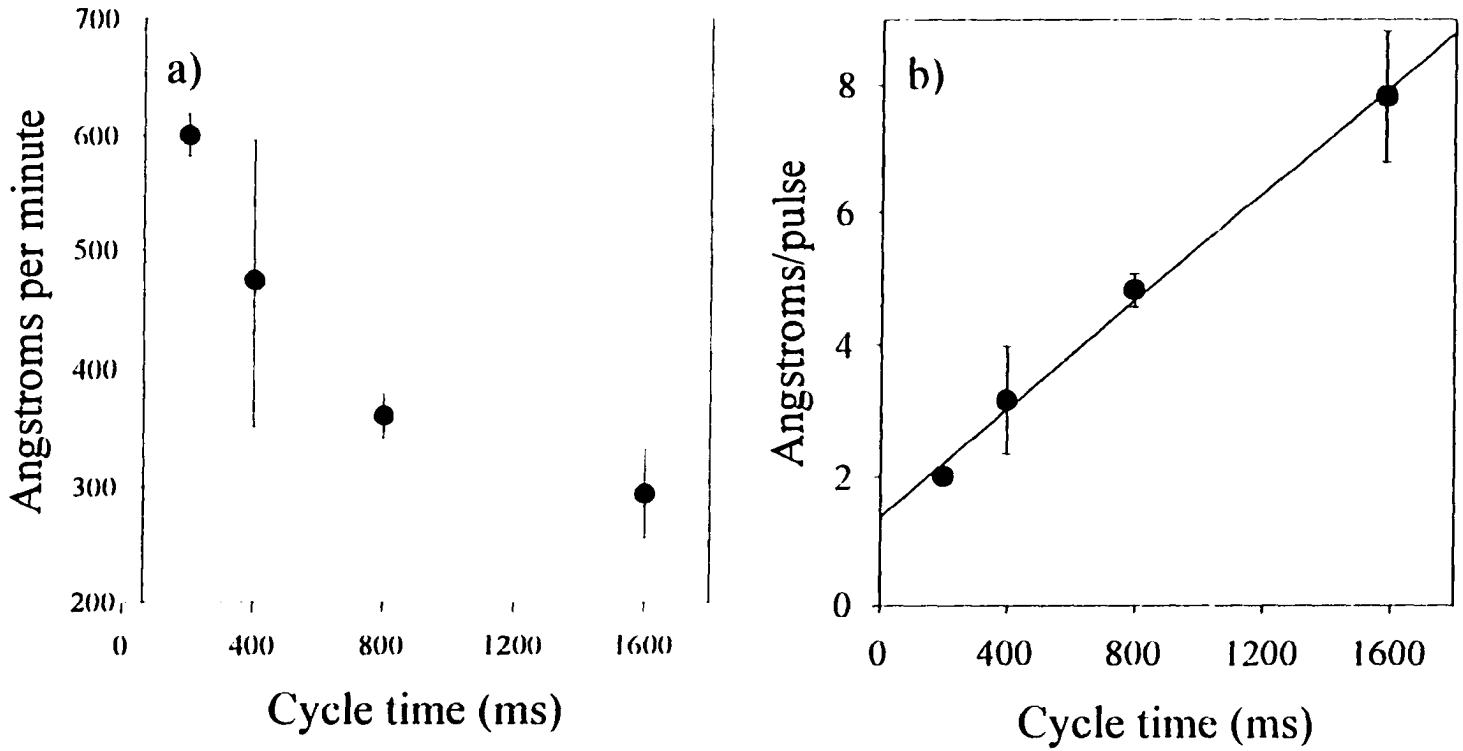

Figure 8.8. a) Deposition rate as a function of cycle time and b) deposition rate per pulse as a function of cycle time for pulsed plasma depositions with P = 500 W and a constant duty cycle of 1%.

Table 8.2. Atomic Stoichiometries for Aged a-$Si_{1-x}C_x$:H Films[a]

	atomic %		
Plasma Conditions[b]	**Si**	**C**	**O**
CW, Ungrounded	37.7	29.2	33.1
CW, Grounded	36.9±0.3	33.4±0.7	29.8±0.5
CW, (-) Bias	35.4±1.2	31.6±1.5	32.1±0.3
CW, (+) Bias	35.6±0.7	35.3±0.1	29.2±0.8
CW, Ungrounded, with H_2	45.1±0.1	24.6±0.4	30.3±0.4
CW, Grounded, with H_2	45.6±0.1	33.5±0.1	20.8
Pulsed, Ungrounded	36.5	48.2	15.4
Pulsed, Grounded	32.0±0.1	52.1±1.2	15.9±1.3
Pulsed, (-) Bias	30.2±1.9	55.2±0.3	13.6±2.1
Pulsed, (+) Bias	30.7±1.5	56.4±2.1	13.1±0.6
Pulsed, Ungrounded, with H_2	32.4	51.5	16.2
Pulsed, Grounded, with H_2	44.5±0.4	36.0±0.9	19.6±1.3

[a]XPS analysis was performed ~4 days after deposition. Error limits given on selected samples are one standard deviation of the mean for the samples, and indicate the reproducibility of the analysis. [b]CW = continuous wave plasma; pulsed = pulsed plasma with P = 500 W, 1% duty cycle; grounded/ungrounded refers to the Si substrate; (- or +) Bias refers to the substrate bias of either +1000 V or -1000 V; with H_2 indicates the deposition was performed with H_2 added to the SiH_4/CH_4 feed.

any of the film compositions with the exception of films deposited with H_2 dilution, where the Si/C ratio increased from 0.63 to 1.24. All films deposited in pulsed plasmas show significantly higher C/Si ratios than their CW counterparts with the exception of depositions on grounded substrates with H_2 dilution.

H_2 dilution significantly changed not only the film composition for both the pulsed and CW plasma films deposited on grounded substrates, it also dramatically changed the bonding environment in the film as shown by high resolution XPS data, Fig. 8.9. In films deposited with H_2 dilution from both pulsed and CW plasmas, Si was present primarily in its elemental form (55-65% of total Si_{2p} area), Fig. 8.9a.[21] The remaining Si species were carbide (20-30% of total Si_{2p} area) and oxide (10-15% of total Si_{2p} area), Fig. 8.9a. In contrast, CW and pulsed plasma deposited films without H_2 dilution showed Si bonding primarily to carbide (pulsed: 70-80%, CW: 35-45%) and oxide (pulsed: 20-30%; CW: 55-65%).

In the C_{1s} spectra of films deposited in pulsed plasmas with H_2 dilution, Fig. 8.9b, two distinct peaks are resolved. The BEs of these peaks are characteristic of carbide and hydrocarbon with relative areas of 35-45% carbide and 55-65% hydrocarbon. In contrast, the C_{1s} spectra of films deposited from SiH_4/CH_4 mixtures with no hydrogen all had one rather broad peak, due to a combination of silicon carbide, graphite, and hydrocarbon species. It is likely the addition of H_2 to the plasma significantly decreases the amount of graphite-like carbon present in the film. As graphite has a BE that falls between hydrocarbon and carbide, a reduction in the amount of graphite-like material present would make it possible to resolve the carbide and hydrocarbon peaks, Fig. 8.9b.

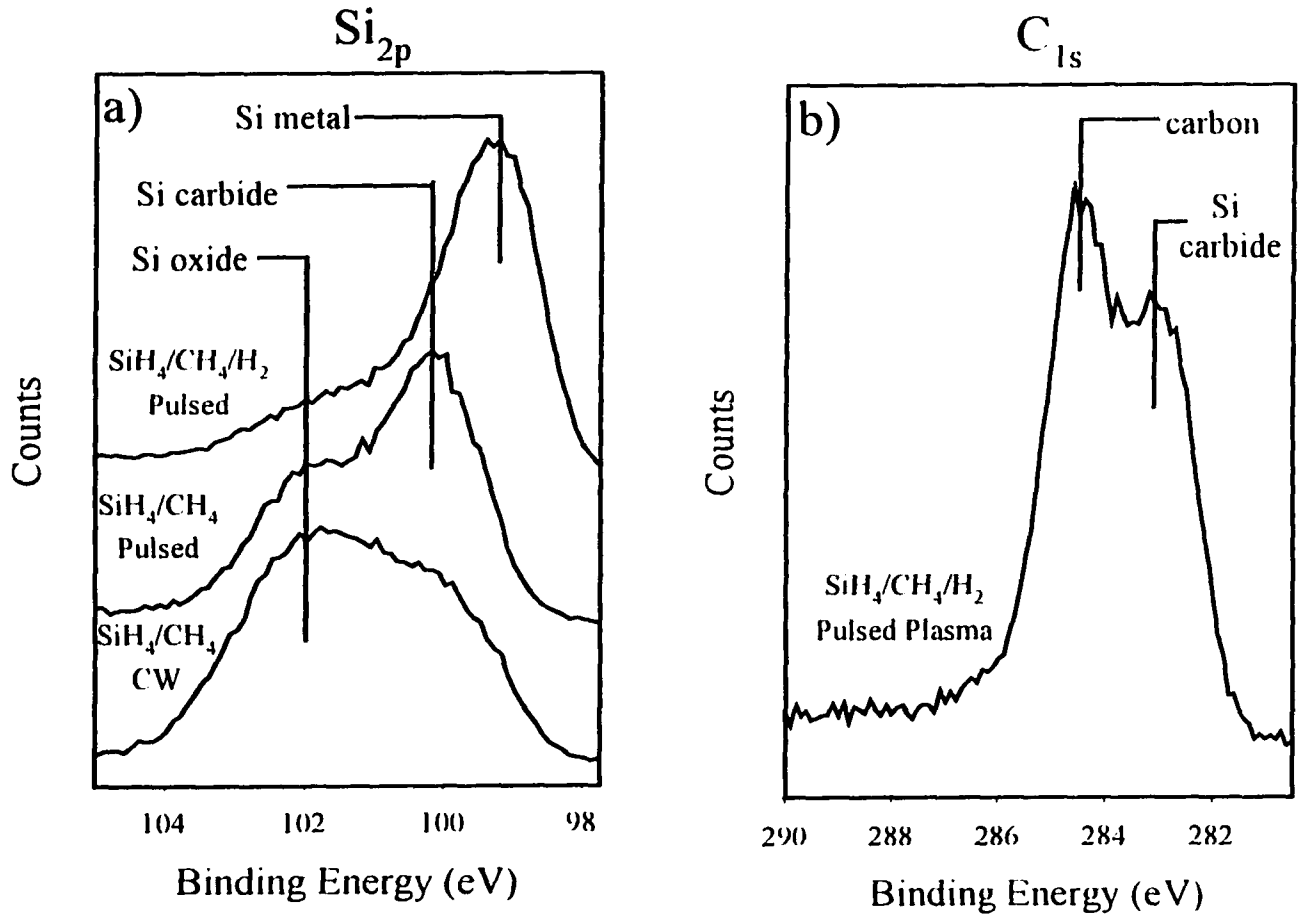

Figure 8.9. a) XPS Si_{2p} spectra for a-$Si_{1-x}C_x$:H films deposited: from a pulsed plasma with H_2 dilution and P = 500 W, 1% duty cycle (top spectrum); from a similar pulsed plasma with no H_2 dilution (middle spectrum); and from a CW plasma (bottom spectrum). b) XPS C_{1s} spectrum for a film deposited from a pulsed plasma with H_2 dilution and P = 500 W, 1% duty cycle.

8.2.4. SCANNING ELECTRON MICROSCOPY

SEM images of a-Si_xC_{1-x}:H films showed similar morphology under all deposition conditions (both pulsed and CW) with the exception of films deposited on ungrounded substrates in pulsed SiH_4/CH_4 plasmas. Figure 8.10a shows a SEM image of a film deposited onto a grounded substrate in a pulsed plasma. The image shows a smooth surface with occasional mounds dispersed over the surface. Figure 8.10b shows a very different morphology for a film deposited onto an ungrounded substrate in a pulsed plasma. Here the surface has a very rough "cauliflower"-like appearance. This rough surface suggests a significant amount of damage is occurring, presumably from ion bombardment[22] or other energetic plasma species. SEM images of films deposited with H_2 added also show smooth surfaces similar to that shown in Fig. 8.10a.

8.2.5. OPTICAL EMISSION SPECTROSCOPY

The gas-phase content of SiH_4/CH_4 CW plasmas were characterized using OES. Figure 8.11 shows a stacked plot of emission spectra from 63 and 72 W SiH_4/CH_4 plasmas over the wavelength range of 400-713 nm. The spectra are characterized by a strong H_α emission at 656.3 nm, an H_2 emission band from 575 to 645 nm, and a low intensity CH emission at 430 nm. Although the applied rf power was changed by only 9 W, the intensity of the H_α line is over an order of magnitude greater for the 72 W plasma. Similar intensity increases were observed for the H_2 band. In addition, no H_β or CH emissions were observed in the 63 W plasma.

Figure 8.12 shows a stacked plot of emission spectra from a high power CW

a)

b)

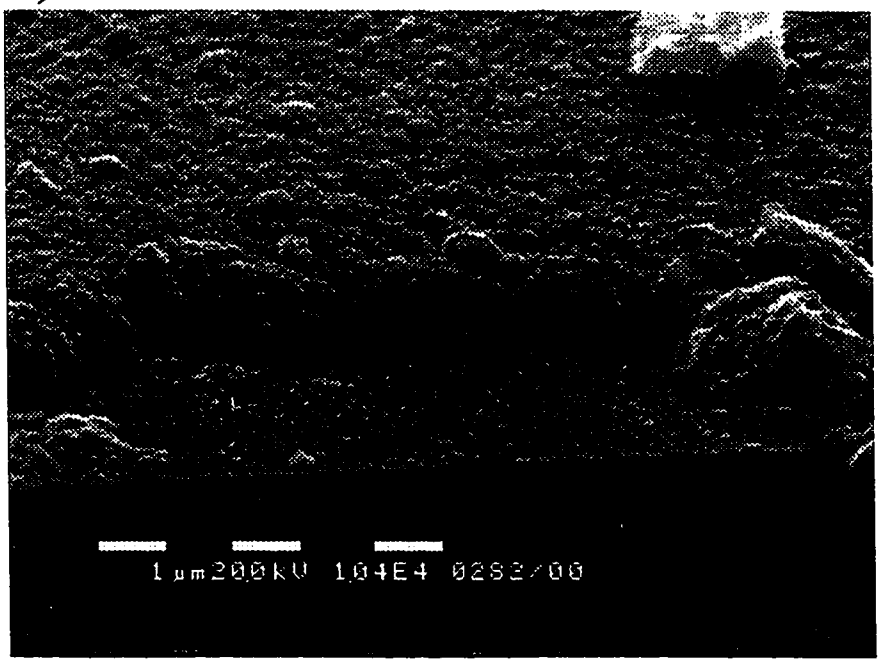

Figure 8.10. Scanning electron micrographs of films deposited for 30 minutes from pulsed plasmas with P = 500 W, 1% duty cycle on: a) grounded and b) ungrounded Si substrates.

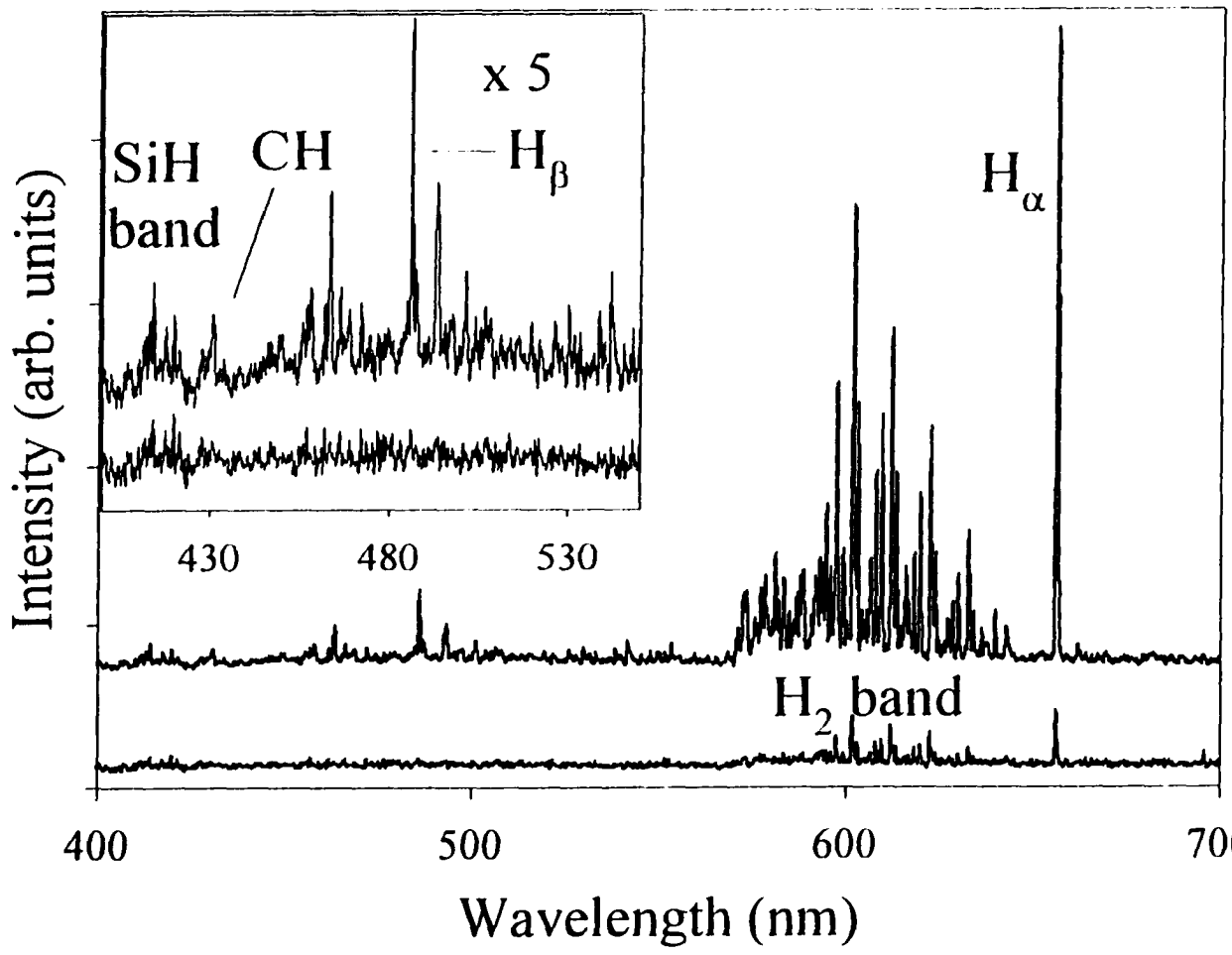

Figure 8.11. Optical emission spectra of SiH_4/CH_4 CW plasmas with P =72 W (upper spectrum) and P = 63 W (lower spectrum). Spectra were collected with a 2 second acquisition time. The inset shows an expanded view of the SiH and CH bands from 400-540 nm.

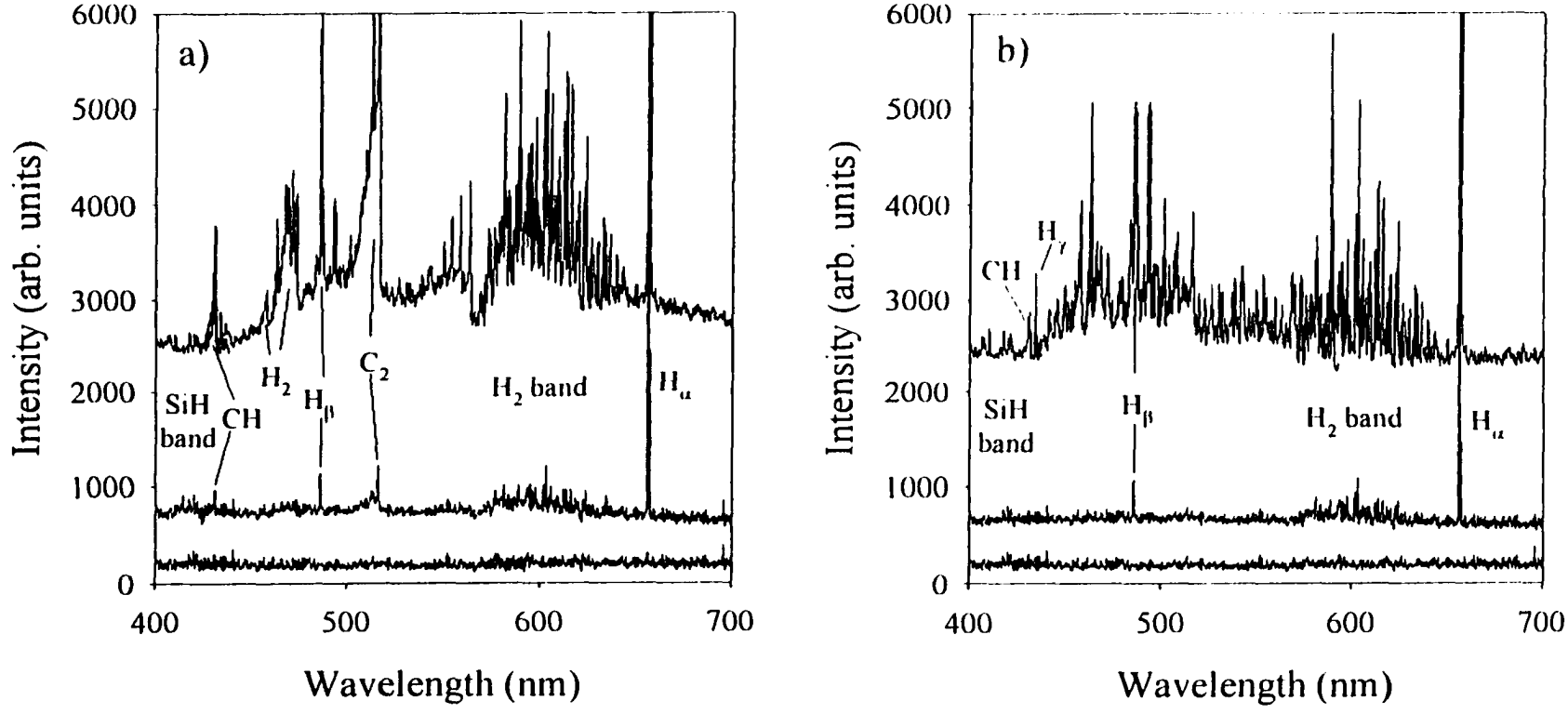

Figure 8.12. Optical emission spectra of SiH_4/CH_4 plasmas: P =500 W CW (upper spectrum), 5 W CW (middle spectrum), and P = 500 W pulsed (lower spectrum), a) without H_2 dilution, b) with H_2 dilution. Spectra were collected with a 2 second acquisition time.

plasma (P = 500 W), a high peak power pulsed plasma (P = 500, 1% duty cycle, 2 ms on time), and a low power CW plasma (P = 5 W) with no H_2 dilution. The low power plasma shows very low intensity emission over the entire range of the spectrum. The pulsed plasma and the high powered CW plasma without H_2 dilution show substantial amounts of C_2, CH, H_α, H_β, and H_2 emissions. In contrast, the pulsed plasma and high power CW plasma in the H_2 dilution system show a marked decrease in CH emission at 430.9 nm and C_2 emission at 516.3 nm. This implies there is less fragmentation of CH_4 in the H_2 dilution system. The large emission from C_2 in the pulsed plasma and the 500 W CW plasma without H_2 dilution and the lack of this emission in plasmas with H_2 dilution helps to explain the change in graphitic carbon content seen in the XPS data.

8.3. DISCUSSION

This work was undertaken to examine the deposition of a-$Si_{1-x}C_x$:H as a function of pulsed plasma parameters and to compare these films with those deposited in equivalently powered CW plasmas. The main experimental results may be summarized as follows: (1) FTIR results demonstrate that the composition of films deposited from pulsed and CW plasmas are significantly different. Moreover, pulse parameters greatly affect the resulting film composition and film deposition rate. (2) Grounding the substrate in both the pulsed and CW systems results in a decrease in oxidation rates and a decrease in the methyl group incorporation in the film. In the pulsed system, FTIR spectra show a significant shift of the Si-C vibration for films deposited on ungrounded substrates. Removal of the ions by use of deflector plates in the pulsed plasmas results in an increased

oxidation rate and more SiH_x incorporation in the film. (3) FTIR and XPS results show hydrogen dilution also significantly affects film composition. In general, H_2 reduces the amount of CH_3 incorporation for all systems and also reduces oxidation rates for all films. These results are discussed further below.

8.3.1. PULSE PARAMETERS.

The results obtained here show that very different film compositions result with CW and equivalently powered pulsed plasmas. First, as reported in Chapter 7, oxidation rates for films deposited in CW plasmas are considerably faster than films deposited from equivalently powered pulsed plasmas. We believe this is because there are fewer trapped radicals and fewer microvoids in the films produced in pulsed systems. Possible oxidation mechanisms for these materials are discussed in Chapter 7.

The second compositional difference observed is that there is greater carbon incorporation in films deposited from SiH_4/CH_4 pulsed plasmas, Table 8.2. This is likely the result of increased fragmentation of CH_4 in the pulsed plasma during the on time. With P = 500 W, we achieve a high density plasma during the on times of the pulse cycle (~1 W/cm^3) relative to the CW system (~0.01 W/cm^3). This can lead to more fragmentation of the relatively inert CH_4 molecule than in the 5W CW plasma, thus introducing a greater carbon incorporation in the resulting film. Although pulsed systems are generally thought to decrease fragmentation of organic monomers,[1,4] we believe the very high peak powers used in the present system do afford greater fragmentation of the CH_4 when compared to the CW system. This is supported by OES measurements of a 5W

CW plasma which show no emission signal due to CH or C_2 radicals in the plasma, Fig. 8.12. In contrast, the emission spectrum for the equivalently-powered pulsed plasma (P = 500 W, 1% duty cycle) shows significant signal from both the CH ($A^2\Delta$ - $X^2\Pi$) band at ~430 nm, and C_2 emission at 516.3 nm, Fig 8.12.[23]

The third compositional difference is the greater hydrogen incorporation in films deposited from the CW SiH_4/CH_4 plasmas relative to the pulsed systems. This is most obvious when considering the SiH_x stretching and bending modes, which are present in the CW films, but are not distinct absorption peaks in the films deposited from the pulsed plasmas. Since most of the gas-phase fragmentation in the CW plasma occurs with SiH_4 rather than with CH_4, we see incorporation of various SiH_x moieties in the resulting film. In the pulsed plasma, surface "annealing" may occur through radical reactions at the film surface during the off time.[24] These types of reactions generally serve to decrease the amount of hydrogen in a film and, in polymerization systems, decrease the crosslinking in the material.[7]

In considering only the pulsed plasmas, the pulse parameter that most influences film composition appears to be the peak applied rf power. FTIR spectra of films deposited from P = 63 W and P = 72 W pulsed plasmas (equivalently powered at 5 W) demonstrate significant changes occur in the deposition process between these two powers, Fig. 8.2. In addition, a large increase in optical emission is observed in the OES spectra of 63 and 72 W CW plasmas, Fig. 8.11. This suggests that the changes in film properties may be related to differences in the gas-phase chemistry during the plasma on time. This change in emission intensity is also accompanied by a decrease in reflected power for the

discharge. At higher CW powers (i.e. ≤500 W), the OES spectra show increased fragmentation as evidenced by higher intensities in the C_2, CH and hydrogen emission bands, Fig. 12.

This type of increase in optical emission with increasing applied rf power is a well-documented phenomenon of electrodeless rf discharges.[25] In a review article, Eckert ascribes this increase in optical emission to a change in coupling modes in the plasma.[26] At low *P*, a capacitive-coupled electrostatic predischarge exists, characterized by low plasma densities, low photoemission densities, and relatively high reflected powers. At higher *P*, an inductively-coupled electromagnetic main discharge results, characterized by high plasma densities, a bright emission and low reflected powers. Two modes have been observed for discharges of Ar, Cl_2, and N_2.[27,28]

For a-$Si_{1-x}C_x$:H deposition systems, Schmidt et al. observed low and high power-density regimes in their SiH_4/CH_4 CW plasmas.[29] Films deposited in the low power-density regime were characterized by a low level of carbon incorporation even at high CH_4/SiH_4 flow ratios. In contrast, films deposited in the high power-density regime had much higher C/Si ratios. The minimal carbon incorporation at low power-density is attributed to preferential electron impact dissociation of SiH_4 over CH_4, suggesting that CH_x radicals in the plasma are the result of reactions between SiH_x radicals and CH_4. This is supported by the results of Catherine et al. who reported that CH_4 is fragmented by electron impact under high power conditions, with a rate constant an order of magnitude lower than that for SiH_4.[30]

In our pulsed plasmas, the change in plasma modes is largely responsible for the

variation in film properties observed with a change in *P*. XPS data show that carbon incorporation is much lower in films deposited from 5 W, CW plasmas than from a 500 W, 1% pulsed plasma, Table 8.2. The FTIR spectra also show lower concentrations of both CH_x and SiH_x groups in films deposited in the pulsed system, Fig. 8.1. This is likely the result of increased gas-phase fragmentation of both CH_x and SiH_x species in the pulsed system due to greater plasma densities during pulse on times. This greater fragmentation leads to fewer SiH_x and CH_x moieties in the deposited film. Pulsed plasmas allow for the deposition of unique materials by accessing higher density plasma regimes without the generation of high substrate temperatures since the overall power input is low.

Another pulse parameter to consider is the pulse cycle time, which affects film deposition rates. Data taken with different plasma off times show an inverse relationship between T_S and the deposition rate per pulse, which has been seen in other systems.[1,31,32] By only changing the cycle time, while leaving *P* and duty cycle constant, equal minimal heating of the substrate is obtained. For these experiments the highest deposition rates were found for the shortest cycle times and there is a linear relationship between the film deposition rate/pulse and the cycle time, Fig 8.8. These results suggest that film deposition occurs during both the plasma on time and the plasma off time. The latter deposition is likely due to active species created during the on time reacting at the surface of the growing film at the beginning of the off time.

8.3.2. SUBSTRATE BIAS

One difference observed in film composition with grounded or biased substrates vs

ungrounded substrates in both the CW and pulsed systems is a significant decrease in CH_3 group incorporation. Methyl groups are thought to result in microvoids and dangling bonds in the growing film,[33,34] a primary cause of electrical and mechanical instability in these films.[35,36] In the pulsed plasmas, one possible mechanism for methyl group incorporation is the formation of active surface sites/dangling bonds created by bombarding ions during the on time, which subsequently react with CH_3 species during the off time. This seems reasonable as methyl radicals are a dominant species in CH_4 plasmas,[37] and they have moderate surface reactivities.[38]

In addition to lower CH_3 levels, there are three other characteristics that distinguish films deposited in pulsed plasmas on ungrounded substrates: 1) the Si-C stretching vibration in the IR shifts to higher frequencies, from ~780 to 837 cm^{-1} and is narrower than that found for films formed on grounded substrates; 2) the films display significantly different morphology, with a "cauliflower"-like structure; and 3) the oxidation rates for these films are significantly faster than their grounded counterparts. One possible explanation for the Si-C frequency shift is a large increase in the C/Si ratio, which would cause the Si-C stretch to shift to higher frequency because C is a harder and lighter atom than Si. The XPS data, however, show similar C/Si ratios in the surface composition for both films. While the bulk composition of these films may differ significantly from that near the surface (XPS sampling depth ~100 Å), we do not believe this is the central reason for the observed shift in frequency.

A more likely possibility is that this shift is the result of a large increase in the number of "dangling bonds" or trapped radicals in the film. This is supported by the other

two distinguishing features of these films, the increased oxidation rates and the different morphology. Moreover, several other studies have shown that when a-SiC, or a-$Si_{1-x}C_x$:H films are annealed at high temperatures, the Si-C stretch in the IR shifts to higher frequency and the peak width decreases.[9,39,40,41,42] It is generally believed that crystallization of the film is occurring at these increased temperatures. Indeed, Yoshii et al. suggest that the peak shift to ~800 cm^{-1} is related to a phase transition from amorphous to polycrystalline β-SiC.[44] In films with low carbon content, the Si-C stretching absorbance shifts to even higher frequencies upon annealing, 818 cm^{-1}. For these materials, the shift to frequencies greater than 800 cm^{-1} was attributed to dangling bonds in the films.[44] This suggestion was supported by electron spin resonance (ESR) data that showed a large spin density even after annealing at 1000 °C.

In our experiments, this shift is only seen in the films deposited on *ungrounded* substrates. This suggests the effect is the result of self-biasing of the substrate which can greatly increase the voltage drop across the sheath compared to that for the grounded substrates. The voltage drop determines the energy of the charged particles hitting the substrate and high energy ions are considered the primary cause of surface damage and dangling bonds in plasma-deposited films.[34] Thus, our results suggest that the three differences we observe for films deposited on grounded substrates are all the result of an increase in high energy ion bombardment of the ungrounded substrates, relative to the grounded substrates.

8.3.3. H_2 DILUTION

Addition of H_2 to the feed results in much higher Si/C ratios than for films deposited without H_2 dilution in both the CW and pulsed systems, Table 8.2. This increase in silicon content is likely the result of gas phase H atoms reacting with SiH_4 to form SiH_3,[43] and reacting with CH_3 radicals to form CH_4. These reactions serve to increase the concentration of active silicon precursors, while decreasing the concentration of carbon precursors in the plasma. OES data show addition of H_2 to a 500 W CW plasma results in a marked decrease in CH emission at ~430 nm, Fig. 8.12. This suggests less fragmentation of CH_4 is occurring in the $SiH_4/CH_4/H_2$ system. Moreover, gas-phase H atoms can abstract surface moieties such as CH_3 and CH_2, again resulting in an increased Si/C ratios in these films.[44] These surface reactions also reduce the oxidation rate of CW films by annealing the surface through reactions with dangling bonds in the film, as discussed in Chapter 7.

In addition to reducing the oxidation rate and increasing the Si/C ratio, H_2 dilution also changes the bonding environment of Si in the films, as revealed by the XPS data of Fig. 8.9. Addition of H_2 to the pulsed plasma results in a decrease in the silicon carbide and silicon oxide peaks in the Si_{2p} spectrum of aged samples and an increase in the Si metal peak. Likewise, the C_{1s} XPS spectrum shows a significant amount of carbon, relative to silicon carbide, with little graphitic carbon incorporation. This implies the carbon is incorporated into the silicon network[33] with both threefold and fourfold coordination, but that hydrogen dilution increases the concentration with fourfold coordination.[45,46] Thus, films deposited from $SiH_4/CH_4/H_2$ pulsed plasmas, while

amorphous in nature, are partially chemically ordered.[47]

OES spectra of pulsed 500 W plasmas with no H_2 dilution show significant emission from C_2 at 516.3 nm. For emission spectra of pulsed plasmas taken with H_2 dilution, no C_2 emission is noted. This implies that H_2 dilution reduces the fragmentation of CH_4 in the plasma. There is a correlation in the 500 W pulsed plasmas between C_2 emission (Fig. 8.12) and graphitic carbon incorporation in the film (Fig 8.9b). It is reasonable that C_2 in the 500 W plasmas leads to higher levels of graphitic carbon in the deposited a-$Si_{1-x}C_x$:H films. It also reasonable that the suppression of C_2 production in the 500 W plasmas with H_2 dilution leads to less graphitic carbon incorporation into the deposited film.

8.4. CONCLUSIONS

Film composition and deposition rates have been obtained for a-$Si_{1-x}C_x$:H films deposited from pulsed SiH_4/CH_4 plasmas and are compared to films deposited in equivalently powered CW plasmas. Grounding the Si substrates in the pulsed plasmas resulted in films with slower oxidation rates. Films deposited on ungrounded substrates in the SiH_4/CH_4 pulsed plasma had a considerably rougher surface morphology and a Si-C stretching frequency shifted to much higher values. Films deposited on grounded substrates had significantly lower methyl group incorporation and lower rates of oxidation than their ungrounded counterparts. Hydrogen dilution in the plasma results in an increase in the Si/C ratio.

REFERENCES

1. N. M. Mackie, N. F. Dalleska, D. G. Castner, and E. R. Fisher, Chem. Mater. **9**, 349 (1997).

2. C. L. Rinsch, X. Chen, V. Panchalingam, R. C. Eberhart, J.-H. Wan, and R. B. Timmons, Langmuir **12** 2995 (1996).

3. C. R. Savage, R. B. Timmons, and J. W. Lin, in *Structures–Property Relations in Polymers*, (American Chemical Society, Washington DC, 1993) p. 745.

4. N. M. Mackie, D. G. Castner, and E. R. Fisher, *Langmuir* **14**, 1227 (1998). N. M. Mackie and E. R. Fisher, Polym. Prepr. **38**, 1059 (1997). M. A. Leich, N. M. Mackie, K. L. Williams, and E. R. Fisher, Macromolecules **31**, 7618 (1998). A. E. Lefohn, N. M. Mackie, E. R. Fisher, Plasma Polym., accepted for publication.

5. H. Yasuda, *Plasma Polymerization* (Academic Press, Orlando, FL, 1985).

6. N. Morosoff, *Plasma Deposition, Treatment and Etching of Polymers*; d'Agostino, R., Ed. (Academic Press, Boston, 1990) p 9.

7. V. Panchalingam, X. Chen, C. R. Savage, R. B. Timmons, and R.C. Eberhart, J. Appl. Polym. Sci. **54**, 123 (1994).

8. K. Hiramatsu, H. Ohnishi, T. Takahama, and K.-I. Yamanishi, J. Vac. Sci. Technol. A **14**, 1037 (1996).

9. H. Wieder, M. Cardona, and C. R. Guarnieri, Phys. Stat. Sol. (b) **92**, 99 (1979).

10. Y. Tawada, K. Ysuge, M. Kondo, H. Okamoto, and Y. Hamakawa, J. Appl. Phys. **53**, 5273 (1982).

11. P. J. R. Honeybone, J. K. Walters, D. W. Huxley, R. J. Newport, W. S. Howells, J. Tomkinson, and C. Hotham, J. Non-Crsyt. Solids **169**, 54 (1994).

12. W.-L. Lin, H.-K. Tsai, S.-C. Lee, W.-J. Sah, and W.-J. Tzeng, Appl. Phys. Lett. **51**, 2112 (1987).

13. W. K. Choi, Y. M. Chan, C. H. Ling, Y. Lee, R. Gopalakrishnan, and K. L. Tan, J. Appl. Phys. **77**, 827 (1995).

14. J. Huran, L. Hrubcin, A. P. Kobzev, and J. Liday, Vacuum **47**, 1223 (1996).

15. F. Fujimoto, A. Ootuka, K.-I. Komaki, Y. Iwata, I. Yamane, H. Yamashita, Y. Hashimoto, Y. Tawada, K. Nishimura, H. Okamoto, and Y. Hamakawa, Jpn. J.

Appl. Phys. **23**, 810 (1984).

16. F. Demichelis, G. Crovini, C. F. Pirri, and E. Tresso, Phil. Mag. B **68**, 329 (1993).

17. J. L. C. Fonseca, D. C. Apperley, and J. P. S. Badyal, Chem. Mater. **5**, 1676 (1993).

18. Above ±1 kV arcing occurred between the substrate and the coil or metal fittings to the glass reactor.

19. The maximum voltage that could be applied to the plates without arcing was ±200V.

20. J. R. Bottin, P. R. McCurdy, and E. R. Fisher, Rev. Sci. Instrum. **68**, 2149 (1997).

21. Data in Figure 8.9 is shown only for the pulsed plasma deposited film, however, similar results were obtained for the CW system.

22. M. J. Armstrong and R. H. Muller, J. Appl. Phys. **65**, 3056 (1989).

23. A. Pastol and Y. Catherine, J. Phys. D: Appl. Phys. **23**, 799 (1990).

24. K. Yasui, M. Muramoto, and T. Akahane, Jpn. J. Appl. Phys. **33**, 4395 (1994).

25. U. Kortshagen, N. D. Gibson, and J. E. Lawler, J. Phys. D: Appl. Phys. **29**, 1224 (1996).

26. H. U. Eckert, *Proc. 2nd Int. Conf. Plasma Chem. Technol.*, edited by H. Boening, (Technomic, Lancaster, PA, 1986), p 171.

27. P. A. Miller, G. A. Hebner, K. E. Greenberg, P. D. Pochan, and B. P. Aragon, J. Res. Natl. Inst. Stand. Technol. **100**, 427 (1995).

28. J. Y. Choe, I. P. Herman, and V. M. Donnelly, J. Vac. Sci. Technol. A **15**, 3024 (1997).

29. M. P. Schmidt, I. Solomon, H. Tran-quoc, and J. Bullot, J. Non-Cryst. Solids **77/78**, 849 (1985).

30. Y. Catherine, G. Turban, and G. Grolleau, Plasma Chem. Plasma Process. **2**, 81 (1982).

31. D. M. Bhusari and S. T. Kshirsagar, J. Appl. Phys. **73**, 1743 (1993).

32. K. Yamamoto, Y. Ichikawa, N. Fukada, T. Nakayama, and Y. Tawada, Thin Solid Films **173**, 253 (1989).

33. H- K. Tsai, W- L. Lin, W. J. Sah, and S- C. Lee, J Appl. Phys. **64**, 1910 (1988).

34. W- J. Sah, H- K. Tsai, and S- C. Lee, Appl. Phys. Lett. **54**, 617 (1989).

35. J. Folsch, H. Rubel, and H. Schade, Appl. Phys. Lett. **61**, 3029 (1992).

36. W. Beyer, R. Hagar, H. Schmidbaur, and G. Winterling, Appl. Phys. Lett. **54**, 1666 (1989).

37. H. Kojima, H. Toyoda, and H. Sugai, Appl. Phys. Lett. **55**, 1292 (1989).

38. H. Toyoda, H. Kojima, and H. Sugai, Appl. Phys. Lett. **54**, 1507 (1989).

39. P. Musumeci, R. Reitano, L. Calcagno, F. Roccaforte, A. Makhtari, and M. G. Grimaldi, Phil. Mag. B **76**, 323 (1997).

40. W K. Choi, T. Y. Ong, L. S. Tan, F. C. Loh, and K. L. Tan, J. Appl. Phys. **83**, 4968 (1998).

41. K. M. Kramer and M. O. Thompson, J. Appl. Phys. **79**, 4118 (1996).

42. K. Yoshii, Y. Suszaki, A. Yakeuchi, K.Yasutake, and H. Kawabe, Thin Solid Films **199**, 85 (1991).

43. M. J. Kushner, J. Appl. Phys. **63**, 2532 (1988).

44. G. Cicala, P. Capezzuto, G. Bruno, L. Schiavulli, and G. Amato, J. Appl. Phys. **79**, 8856 (1996).

45. A. Tabata, S. Fujii, Y. Suzuoki, T. Mizutani, and M. Ieda, J. Phys. D: Appl. Phys. **23**, 316 (1990).

46. Y. Katayama, K. Usami, and T. Shimada, Philos. Mag. B. **2**, 283 (1981).

47. A. Chehaidar, R. Carles, A. Zwick, C. Meunier, B. Cros, and J. Durand, J. Non-Cryst. Solids **169**, 37 (1994).

APPENDIX 1:

SURFACE SCATTER/MOLECULAR BEAM

VELOCITY DISTRIBUTION PROGRAM

The velocity distribution program is designed to provide one dimensional simulations of the velocity distribution of a given species either in a molecular beam or scattering from a surface. The model assumes an initial Gaussian distribution of molecules across the path of the laser beam. It also assumes a Maxwell-Boltzmann distribution function for the velocity of molecules either in the molecular beam or scattering from a surface. For scattered molecules, the distribution function can either be assumed to have no angular dependence or a cosine angular dependence. The program can also give higher levels of angular dependence for the cosine function.

The code is written in C++. In this appendix, text in normal type is the code for modeling the velocity distribution of species in the molecular beam. The additional code in italics modifies the original program to allow for velocity distribution simulations of molecules scattering from a surface.

In general, the program is designed to create functions for a Gaussian distribution, a Maxwell-Boltzmann distribution, and a cosine distribution. These distribution functions are then integrated, and their areas divided into equal probability bins. When a 'molecule' is generated, it is pseudorandomly given an initial position, a velocity, and an 'x' component for its direction of motion, determined by a Gaussian, Maxwell-Boltzmann, and cosine functions respectively. This process is repeated until a statistically significant sample is collected (up to 1,000,000 times).

OPERATING INSTRUCTIONS

I. The Program.

The program is straight-forward and easy to use. For the surface velocity scatter program there are eight input parameters: temperature, time delay, mass, laser cross section, substrate height, laser-surface distance, a cosine distribution function, and the starting position. For the temperature you should input your best approximation of the translational temperature of your molecule. The time delay is the time from when the laser excites your molecule to the center of your camera gate in microseconds. To determine your time delay you must determine the time it takes from triggering the laser to the light entering the interaction region. This can be done by either increasing or decreasing your gate delay incrementally until scattered light is observed using a short gate width (100-200 ns) and a very short acquistion time < 1 second. Mass should be input in AMU. The laser cross section is generally best determined by fitting the experimental data taken at the shortest time delay, since at short time delays the molecules have not moved much and should be representative of the laser's cross section. The substrate height is generally ~25 mm (1 inch). The laser surface distance is the distance from the surface to the laser beam along the surface normal. The cosine function is the angular dependence of the distribution of molecules scattering from the surface. If there is no angular dependence a zero should be entered. If there is a cosine angular dependence a 1 should be entered. Distributions with higher angular dependencies can also be modeled. The starting position is simply where you want your x axis to begin, and is determined from the experimental data. Generally this number is ~ -15 mm.

II. Data Taking.

Normal IRIS data is taken with pixels binned 4 x 4 to increase signal to noise, speed up acquisition time, and save disk space. When taking velocity data spatial resolution is critical especially at the shortest time delays, therefore pixels are unbinned (0.08958 mm by 0.08958 mm). Determining exactly when the laser enters the chamber is critical for accurate modeling. Two factors play against each other when taking this kind of data: signal to noise is best at short time delays, but at short time delays the molecule has had little time to move therefore this data has poorer resolution, while at long time delays the molecule has had more time to move, but there is lower signal-to-noise. You may consider binning your pixels at longer time delays. You will not be able to do least squares fitting as outlined below, however, if you bin your pixels, without going into the program and changing the pixel value. Also, since this is a time resolved experiment, the narrower the gate width the better, generally less than 500 ns. For velocity measurements of molecules in the molecular beam the laser should be brought in perpendicular to the molecular beam to get maximum movement of your molecule with respect to the laser with the surface rotated out of the path of the molecular beam. This will increase the resolution of the experiment by maximizing the pixels traversed by the molecule. The camera must be rotated 45 degrees when in this mode. For scatter velocity measurements it is best to operate the instrument in its normal configuration (laser intersecting the molecular beam at a 45°angle). This will minimize any interference between scattering molecules and the molecular beam. For molecular beam velocity measurements images must be taken on resonance and off resonance, while for scatter measurements, images must be taken on and off resonance with the surface in and out of the path of the molecular beam.

Periodically, the focus of the camera should be checked by placing a card with a checkered grid of known periodicity in the interaction region and imaging the card. A business card works

well with a grid created in Coreldraw with a 2 mm by 2 mm spacing. Once the camera is in focus you will need to determine the area imaged by the camera. By imaging the grid and carefully counting the squares imaged by the camera, you can determine the area imaged by the camera. Your data is only as accurate as this measurement, so this is critical. Incidently, this measurement is also critical for IRIS reactivity measurements as well, as it is used for determining your x-axis spacing.

III. Data Processing

Images should be subtracted from their off-resonance counterparts. For scattered measurements, the background corrected images of surface-out is then subtracted from the surface in-image. For long time delays this may leave a large negative spot on the image where the molecular beam signal has been blocked by the surface. A cross section across the laser's path of averaged pixels–approximately equal to your surface height--is made (~300 pixels). It is imperative to determine exactly where the laser is on the cross section. A good approximation can be made by taking a cross section of the image at the shortest time delay with the surface in before any subtractions are made, the peak intensity of this cross-section should be within one pixel of the laser's path. This file is then exported as a .prn file in WinView. This is done by choosing the *save as* option under the *file* menu. In the *save as* menu option click on *file type* and choose ascii-xy. Then just click *OK* and you're done. This .prn file consist of two columns, the first column represents the pixels across the laser in the image, and the second column gives the amount of LIF signal for the cross-sectional average. The .prn file can then be imported into Sigma Plot. It is a good idea to import these two rows into columns 2 & 3, leaving column 1 open for your x-axis. For scatter velocity data, the data file is generally plotted backwards so you will need to sort the two rows of data and reverse their order. In Sigma Plot this is done simply by using your mouse to highlight the two rows to be sorted and then clicking the *sort* option under the *transform* menu. Once in this menu option just click the '*descending*' option and *OK*. Now your data should be in the right order. After this, go to *transforms* > *user defined*, there type in "col(1) = data(-15, 30, 0.08958)," this will create a data set for the distance from the laser which will be used as the x-axis. You will need the adjust the -15 value in your transform until the pixel which you determine corresponded to the laser's path is zero on the x axis. You can now graph the data by going to *graph* > *create*. Choose *line plot* under the create menu option, then *simple straight line* and *x-y pair*, under x enter column 1 and then column 3 for the y-axis. The simulation also creates a .prn file called fin_dist.prn which can also be imported into Sigma Plot as a comma delimited file. Generally, the simulation will have higher 'intensity' values than the actual data, so it will need to be scaled to the intensity of the data. This can be done simply by creating a 'scaling' column for the simulation. If your simulation is in columns 5 and 6–where 5 is the x axis, or distance from the laser, and column 6 is the number of simulated molecules travelling that distance–column six can be scaled down by adding a line to your transform such as 'col(7)=col(6)*0.01)'. Columns 5 and 7 can then be plotted on the same graph by choosing the *add a plot* option under the *graph* menu option. The steps are identical for creating the initial graph. Once both plots are on the same graph, adjust the transform for creating column 7 to adjust the peak heights until they are about the same height. Least square fitting can be utilized to determine the best fit. The easiest way to do a least squares fit is to make sure the numbers for the x-axis of the data are the same as that for the simulation. At this point this should be the case, if you've done everything correctly. If the x-axes are the same then it is easy to create a transform that takes the difference of the data intensity value and the *corrected* intensity value for the

simulation and then squares this difference. The squared values of these differences can then be summed over the range of interest. The transform should look something like this: 'col(10)=sum((col(7)-col(3))^2),' where column 7 is your scaled simulation intensity, column 3 is your data intensity, and column 10 is the running sum of the square of the differences. The simulation that comes out with the lowest number is the best fit over the range sampled.

VELOCITY SCATTERING MODEL

```
#include <stdlib.h>
#include <iostream.h>
#include <iomanip.h>
#include <math.h>
#include <fstream.h>
struct Distance
{
        long double final_position;
        long double dist;
};
struct Bins
{
        long double vel_component;
        long double probability;
        long double sum_vel_component;
        long double travel_dist;
    long double sum_dis;
    long double sum_probability;
    long double surface;
    long double laser;
    int count;
    long double sum_vel;
    long double velocity;
    int maxwell;
    int life;
    int gauss;
    long double int_dist;
};
struct Molecule_Distributions
{
        long double probability_area_normal;
        long double vel_component;
        long double velocity;
        long double probability_cum_area;
        long double probability;
        long double surface;
        long double travel_dist;
        long double maxwell;
        long double gauss;
        long double gauss_area_norm;
        long double gauss_cum_area;
        long double maxwell_area;
        long double probability_area;
        long double max_area_normal;
        long double gauss_area;
```

```
        long double int_dist;
        long double maxwell_cum_area;
};
const maximum = 400;
const MAX = 2000;
const max = 200;
void main()
{
    Molecule_Distributions molecule[MAX];
    Bins molecules[max];
    Distance distance[maximum];
    int temp = 0;
    int mass = 0;
    long double laser_x_section = 0;
    long double starting_position = 0;
    long double surf_dist = 0;
    long double substrate_height = 0;
    int cos;
    int mass1;
    long double substrate_height1 = 0;
    char ans;
    long double time_delay;
    long double time;
    void data_in(int &temp, int& mass, long double& time_delay,
                 long double& time, long double& laser_x_section, long double&
                 substrate_height, long double& surf_dist, int& cos, long double&
                 starting_position);
    void compute(int temp, int mass, long double time, Molecule_Distributions molecule[], long
                 double laser_x_section, long double, substrate_height, long double surf_dist, int
              cos, long double starting_position);
    void compute2(Molecule_Distributions molecule[], Bins molecules[], int temp, int mass,
                  Distance distance[], long double time, long double laser_x_section, long double
                  substrate_height, long double surf_dist, int cos, long double starting_position);
do
{
    data_in(temp, mass, time_delay, time, laser_x_section, substrate_height, surf_dist, cos,
                 starting_position);
        mass1 = mass;
        substrate_height1 = substrate_height;
    compute(temp, mass, time_delay, molecule.laser_x_section, substrate_height, surf_dist, cos,
                 starting_position);
        mass = mass1;
        substrate_height = substrate_height1;
    compute2(molecule, molecules, temp, mass, distance, time, laser_x_section,
                  substrate_height, surf_dist, cos, starting_position);
        cout <<"Would you like to run another simulation?"<<endl;
        cout <<"(Type y for yes or n for no) ";
```

```
        cin >> ans;
        } while (ans == 'y' || ans == 'Y');
}
   void data_in(int &temp, int& mass, long double& time_delay,
                long double& time, long double& laser_x_section, long double&
                substrate_height, long double& surf_dist, int& cos, long double&
                starting_position)
        {
        int parameter;
        char ans;
        char ans1;
        ifstream in;
        in.open ("data");
        in>>temp>>time_delay>>mass>>laser_x_section>>substrate_height>>surf_dist>>cos>>
             starting_position;
        in.close();
        cout << "1. Temperature                = " <<temp<<" K"<<endl;
        cout << "2. Time delay                 =  " << time_delay<<" microsec"<<endl;
        cout << "3. Mass                       = " <<mass<<" AMU"<<endl;
        cout << "4. Laser x-section            =  " <<laser_x_section<<" mm"<<endl;
        cout << "5. Substrate height           =  " <<substrate_height<<" mm"<<endl;
        cout << "6. Laser-surface Distance     =  " <<surf_dist<<" mm"<<endl;
        cout << "7. Cosine Distribution Function   =  " <<cos<<endl;
        cout << "8. Starting position          = " <<starting_position<<" mm"<<endl;
        cout << "Do you want to change any of these parameters?" << endl;
        cin >> ans;
        if (ans == 'y' || ans == 'Y')
        {
          do
          {
                cout <<"Type the number of the parameter you would like to change."<<endl;
                cin >> parameter;
                switch (parameter)
                {
                        case 1:
                                cout<< "What value do you want to change the temperature
                                to?"<<endl;
                                cin >> temp;
                                break;
                        case 2:
                                cout<< "What value do you want to change the time delay
                                to?"<<endl;
                                cin >> time_delay;
                                break;
                        case 3:
                                cout << "What value do you want to change the atomic mass
                                to?"<<endl;
```

```
                cin >> mass;
                break;
        case 4:
                cout << "What value do you want to change the laser cross
                section to?"<<endl;
                cin >> laser_x_section;
                break;
        case 5:
                cout << "What value do you want to change the substrate height
                to?"<<endl;
                cin >> substrate_height;
                break;
        case 6:
                cout << "What value do you want to change the laser-surface
                distance to?"<<endl;
                cin >> surf_dist;
                break;
        case 7:
                cout << "What value do you want to change the distribution
                function to?"<<endl;
                cin >> cos;
                break;
        case 8:
                cout << "What value do you want to change the starting position
                to?"<<endl;
                cin >> starting_position;
                break;

        }
    cout<< "Would you like to change any more parameters? (y or n)"<<endl;
    cin >> ans1;
    } while (ans1 == 'y' || ans == 'Y');
ofstream out;
out.open("data");
    out <<temp<<" "<<time_delay<<" "<<mass<<" "<<laser_x_section<<"
        "<<substrate_height<<" "<<surf_dist <<" "<<cos<<" "<<starting_position<<endl;
    out.close();
    cout << "These are the parameters with which the program will run."<<endl;
    cout << "1. Temperature              = "<<temp<<" K"<<endl;
    cout << "2. Time delay               =  " << time_delay<<" microsec"<<endl;
    cout << "3. Mass                     =  " <<mass<<" AMU"<<endl;
    cout << "4. Laser x-section          =  " <<laser_x_section<<" mm"<<endl;
    cout << "5. Substrate height         =  " <<substrate_height<<" mm"<<endl;
    cout << "6. Laser-surface distance   =  " << surf_dist<<" mm"<<endl;
    cout << "7. Cosine Distribution Function  =  " <<cos<<endl;
    cout << "8. Starting position        = " <<starting_position<<" mm"<<endl;
```

```
        }
        time = (time_delay*0.000001);
}
void compute(int temp, int mass, long double time,
    Molecule_Distributions molecule[], long double laser_x_section, long double
        substrate_height, long double surf_dist, int cos, long double starting_position)
{
    int i;
    int vel_squared = 0;
    long double initial_position = 0.0;
    long double sum = 0.0;
    long double pixel_dist = 0.0;
    long double tot_pixel_dist = 0.0;
    int pixel_number = 0;
    long double y = 1.5/long double(MAX);
    long double x = 0.0;
    molecule[0].maxwell_cum_area = 0;
    molecule[0].velocity = 0.0;
    cos = cos + 2;
    ofstream out;
    out.open("gauss_dist.prn");
    for (i = 0;i < MAX; i++)
    {
        molecule[i].int_dist = -1.0 + i*y;
    }
    for (i = 0;i < MAX; i++)
    {
       x = molecule[i].int_dist * 6;
       molecule[i].gauss = exp(-(x*x));
    }
    for(i = 0; i < MAX; i++)
    {
      molecule[i].gauss_area=((molecule[i].gauss+molecule[i+1].gauss)*5);
        sum = sum + molecule[i].gauss_area;
    }
    for (i = 0; i <= MAX; i++)
    {
      molecule[i].gauss_area_norm= molecule[i].gauss_area/sum;
    }
    for (i = 1; i < MAX; i++)
    {
        molecule[i].gauss_cum_area = molecule[i-1].gauss_cum_area +
        molecule[i-1].gauss_area_norm;
        out<<setw(12)<<setprecision(5)<<molecule[i].int_dist<<",";
        out<<setprecision(5)<<setw(12)<<molecule[i].gauss<<",";
        out<<setprecision(5)<<setw(12)<<molecule[i].gauss_area;
        out<<setprecision(5)<<setw(12)<<molecule[i].gauss_area_norm;
```

```
        out<<setprecision(5)<<setw(12)<<molecule[i].gauss_cum_area <<endl;
}
out.close();
out.open("maxwell_dist.prn");
for (i = 0;i <= MAX;i++)
{
      molecule[i].velocity = i*2;
   molecule[i].maxwell = molecule[i].velocity*molecule[i].velocity*
      exp(-(.001*mass*molecule[i].velocity*molecule[i].velocity)/
   (2*8.3145*temp));
}
    sum = 0;
for (i = 0; i <= MAX; i++)
{
    molecule[i].maxwell_area=((molecule[i].maxwell+molecule[i+1].maxwell)
        *1);
        sum = sum + molecule[i].maxwell_area;
}
for (i = 0; i <= MAX; i++)
{
    molecule[i].max_area_normal= molecule[i].maxwell_area/sum;
}
for (i = 0; i < MAX; i++)
{
        molecule[i].maxwell_cum_area = molecule[i-1].maxwell_cum_area +
        molecule[i-1].max_area_normal;
        out<<setprecision(5)<<setw(12)<<molecule[i].velocity<<",";
        out<<setprecision(5)<<setw(12)<<molecule[i].maxwell<<",";
        out<<setprecision(5)<<setw(12)<<molecule[i].maxwell_area<<",";
        out<<setprecision(5)<<setw(12)<<molecule[i].max_area_normal;
        out<<setprecision(5)<<setw(12)<<molecule[i].maxwell_cum_area<<endl;
}
out.close();
for (i = 0; i < MAX; i++)
{
        molecule[i].probability = 0;
}
out.open("probability.prn");
for (i = 0; i < MAX; i++)
{
        initial_position = long double(-substrate_height*0.5);
        molecule[i].surface = initial_position +
        long double((i)*substrate_height)/long double(MAX);
        molecule[i].travel_dist = ((molecule[i].surface* molecule[i].surface)+
        (surf_dist*surf_dist));
        molecule[i].travel_dist = sqrt(molecule[i].travel_dist);
        molecule[i].probability = surf_dist/pow(molecule[i].travel_dist, cos);
```

```
        molecule[i].vel_component = surf_dist/molecule[i].travel_dist;
    }
    sum = 0;
    for (i = 0; i < (MAX-1); i++)
    {
      molecule[i].probability_area=((molecule[i].probability+molecule[i+1].probability)
          *1);
          sum = long double(sum) + molecule[i].probability_area;
    }
    for (i = 0; i < (MAX-1); i++)
    {
      molecule[i].probability_area_normal= molecule[i].probability_area/sum;
    }
    for (i = 1; i < MAX; i++)
    {
          molecule[i].probability_cum_area = molecule[i-1].probability_cum_area +
          molecule[i-1].probability_area_normal;
          out<<setprecision(5)<<setw(12)<<molecule[i].probability<<",";
          out<<setprecision(5)<<setw(12)<<molecule[i].probability_area<<",";
          out<<setprecision(5)<<setw(12)<<molecule[i].probability_area_normal<<",";
          out<<setprecision(5)<<setw(12)<<molecule[i].probability_cum_area<<endl;
    }
    out.close();

}
void compute2(Molecule_Distributions molecule[], Bins molecules[], int temp, int mass,
          Distance distance[], long double time, long double laser_x_section, long double
          substrate_height, long double surf_dist, int cos, long double starting_position)
{
    int rand();
    int i;
    int x = 0;
    int w = 0;
    int test = 0;
    int test1 = 0;
    int test2 = 0;
    int test3 = 0;
    int k = 0;
          long double high = 0;
    long double final_dist = 0;
    for(i = 0; i < max; i++)
    {
          molecules[i].count = 0;
          molecules[i].sum_dis = 0;
          molecules[i].int_dist = 0;
    }
    for(i = 0; i < MAX; i++)
```

```
{
      for(k = 0; k < max; k++)
      {
         if(molecule[i].gauss_cum_area <= long double(k+1)/long double(max)&&
         molecule[i].gauss_cum_area > long double(k)/long double(max))
         {
            molecules[k].count = molecules[k].count + 1;
            molecules[k].sum_dis = molecules[k].sum_dis +
            molecule[i].int_dist;
            molecules[k].int_dist = molecules[k].sum_dis/
               molecules[k].count;
      }
   }
}
for(i = 0; i < max; i++)
{
      molecules[i].count = 0;
      molecules[i].sum_dis = 0;
      molecules[i].velocity = 0;
}
for(i = 0; i < MAX; i++)
{
      for(k = 0; k < max; k++)
      {
         if(molecule[i].maxwell_cum_area <= long double(k+1)/long double(max)&&
          molecule[i].maxwell_cum_area > long double(k)/long double(max))
          {
            molecules[k].count = molecules[k].count + 1;
            molecules[k].sum_vel = molecules[k].sum_vel +
            molecule[i].velocity;
            molecules[k].velocity = molecules[k].sum_vel/molecules[k].count;
      }
   }
}
for(i = 0; i < max; i++)
{
      molecules[i].count = 0;
      molecules[i].sum_probability = 0;
      molecules[i].probability = 0;
}
for(i = 0; i < MAX; i++)
{
      for(k = 0; k < max; k++)
      {
         if(molecule[i].probability_cum_area <= long double(k+1)/long double(max)&&
         molecule[i].probability_cum_area > long double(k)/long double(max))
         {
```

```
                molecules[k].count = molecules[k].count + 1;
                molecules[k].sum_probability = molecules[k].sum_probability +
                molecule[i].probability;
                molecules[k].probability = molecules[k].sum_probability/
                                molecules[k].count;
                        molecules[k].sum_vel_component= molecules[k].sum_vel_component +
                                molecule[i].vel_component;
                        molecules[k].vel_component = molecules[k].sum_vel_component/
                                molecules[k].count;
        }
    }
}
ofstream out;
out.open("diag.prn");
for(i = 0; i < max; i++)
{
        if (molecules[i].probability >= high)
        {
        high = molecules[i].probability;
        }
       }
for(i = 0; i < max; i++)
{
        molecules[i].probability = molecules[i].probability / high;
}
for(i = 0; i < max; i++)
{
        out << molecules[i].probability<<"   ";
        out << molecules[i].velocity<<"  ";
        out << molecules[i].int_dist<<endl;
}
out.close();
       for(x = 0; x< maximum; x++)
    distance[x].final_position = 0;
           for(i = 0; i < 1000000; i++)
{
        test = (rand()*max)/32768;
        test1 = (rand()*max)/32768;
        test2 = (rand()*max)/32768;
        test3 = (rand()*max)/32768;
            final_dist = ((laser_x_section * molecules[test].int_dist) +
            (1000 * molecules[test1].velocity*time)
            *(molecules[test2].vel_component)
                  *(molecules[test3].vel_component));
         for(x = 0; x < maximum; x++)
            {
               if ((final_dist < (float(x)+(starting_position/0.08958))*0.08958)
```

```
                &&(final_dist >
                    (float(x)+(starting_position/0.08958)-1)*0.08958))
                distance[x].final_position =
                distance[x].final_position + 1;
        }
}
 out.open("fin_dist.prn");
 out << "T = " <<temp<<" K"<<endl;
 out << "t = " <<time<<" s"<<endl;
 out << "m = " <<mass<<" amu"<<endl;
 out << "l x-sec = " <<laser_x_section<<" mm"<<endl;
 out << "l-s dist = " <<surf_dist<<" mm"<<endl;
 out << "subs. wid. = " <<substrate_height<<" mm"<<endl;
       out << "cos dist = " <<cos<<endl;
       out << "start pos. = " <<starting_position<<" mm"<<endl;
 for(i = 0; i < maximum; i++)
              distance[i].dist = starting_position + i*.08958;
 for(i = 0; i < maximum; i++)
       {
       out << distance[i].dist<<",  "<<distance[i].final_position<<endl;
       }
 out.close();
 for(i = 0; i < maximum; i++)
       {
              distance[i].dist= 0;
              distance[i].final_position=0;
       }
       for(i = 0; i < MAX; i++)
       {
              molecule[i].vel_component= 0;
              molecule[i].velocity=0;
              molecule[i].probability_area_normal= 0;
              molecule[i].probability_cum_area=0;
              molecule[i].probability= 0;
              molecule[i].surface=0;
              molecule[i].travel_dist= 0;
              molecule[i].maxwell=0;
              molecule[i].gauss= 0;
              molecule[i].gauss_area_norm=0;
              molecule[i].gauss_cum_area= 0;
              molecule[i].probability_area=0;
              molecule[i].max_area_normal= 0;
              molecule[i].gauss_area=0;
              molecule[i].int_dist= 0;
              molecule[i].maxwell_cum_area=0;
       }
       for(i = 0; i < max; i++)
```

```
        {
                molecules[i].vel_component= 0;
                molecules[i].sum_vel_component= 0;
                molecules[i].probability= 0;
                molecules[i].surface=0;
                molecules[i].travel_dist= 0;
                molecules[i].sum_dis=0;
                molecules[i].sum_probability= 0;
                molecules[i].surface=0;
                molecules[i].laser= 0;
                molecules[i].count=0;
                molecules[i].sum_vel= 0;
                molecules[i].velocity=0;
                molecules[i].maxwell= 0;
                molecules[i].life=0;
                molecules[i].gauss= 0;
                molecules[i].int_dist=0;
        }
}
```

LIST OF TERMS

vel_component	x component of the velocity vector
probability	probability of molecule having a certain vel_component
sum_vel_component	sums the cosine function for binning
travel_dist	distance molecule must travel from position on surface to laser
sum_dis	sums the initial positions for the Gaussian function for laser
sum_probability	sums the cosine function for binning
surface	initial of molecule on the surface with respect to normal from laser
laser	position of molecule when crossing laser wrt surface normal at intersection point of molecular beam
count	counting function
sum_vel	sums the Maxwell distribution of velocities
velocity	velocity of molecule
maxwell	Maxwell distribution probability function
gauss	Gaussian distribution probability function
int_dist	Initial position of molecule in laser
probability_area_normal	normalizes the area of the cosine function to unity
probability_cum_area	cumulative area under the normalized cosine distribution function
gauss_area_norm	normalizes the area of Gaussian function to unity
gauss_cum_area	cumulative area under the normalized Gaussian distribution function
maxwell_area	area under maxwell function
probability_area	area under cosine function
max_area_normal	normalizes the area of the Maxwell function to unity
gauss_area	area under Gaussian function
maxwell_cum_area	cumulative area under the normalized Maxwell function
maximum	lines of out put
MAX	number of points sampled on a function
max	number of bins
temp	translational temperature of molecule you are modeling
mass	mass of molecule in AMU
laser_x_section	laser cross section at full width half maximum in mm
surf_dist	laser-surface distance
substrate_height	substrate height
cos	angular distribution dependence as a cosine function
mass1	reestablishes mass of molecule
ans	character used in case function
ans1	character used in case function
time_delay	time from when laser excites molecules to center of camera gate in μs
time	time delay in seconds